The Dissertation Committee for Takuji Adachi Certifies that this is the approved version of the following dissertation:

Understanding of Conjugated Polymer Morphology Formation and the Structure-Property Relationships from the Single Chain Level to the Bulk Level

Committee:

David A. Vanden Bout, Supervisor

Peter J. Rossky

Lauren J. Webb

Christopher W. Bielawski

Venkat Ganesan

Understanding of Conjugated Polymer Morphology Formation and the Structure-Property Relationships from the Single Chain Level to the Bulk Level

by

Takuji Adachi, B.E.

Dissertation

Presented to the Faculty of the Graduate School of

The University of Texas at Austin

in Partial Fulfillment

of the Requirements

for the Degree of

Doctor of Philosophy

The University of Texas at Austin

August, 2012

Dedication

To my family.

To Shiori Yamazaki, my first true love, who has supported me through my graduate study while she has been also busy on her own graduate study in Florida.

To Professor Paul F. Barbara, my first supervisor, who passed away on October 31, 2010.

To Sharon and Juliet Barbara, who have been strongly moving forward even after the loss of their important family and saved me from looking down.

To Professor Hiroshi Masuhara who has been a great supporter of my “adventure” in USA.

Acknowledgements

I have so many people that I truly thankful for, but first of all I would like to thank for Professor David A. Vanden Bout. It was very hard to face the reality that Professor Paul Barbara suddenly passed away. I could have simply dropped out from the graduate school if David was not there to take over the role of the supervisor for me. He was always willing to discuss new ideas or next directions with me no matter how stupid ideas I brought to him. After people in the original Barbara group left, he was the one I could discuss science at a bar after work. In fact, I went to drink with David much more than with Paul, and I was so happy to discuss many ideas then. The ACS conference in Denver was particularly memorable. Without his generosity, curiosity and positive attitude, I could have never integrated my graduate research into this dissertation.

I like to thank for my committee members, Professors Peter Rossky, Lauren Webb, Christopher Bielawski, and Venkat Ganesan. They gave me helpful comments and suggestions not just as committee members, but also helped me a lot to go through the time period of Paul's death. They kindly gave me lots of advices regarding both my research and future plans after the graduation.

I like to thank for Professor Paul F. Barbara. His enthusiasm and personality brought me to Texas all the way from Japan. It is very rare for Japanese students to go abroad to get a Ph.D. degree, and I had no idea how and what I could do. I visited Austin in May 2005 to get the feeling of how the life in USA and in Paul's research group would be. To be honest, I could barely communicate in English that time, but Paul told me all kind of stories while he was showing me around the campus. For some reason, I could understand what he was trying to tell me despite my poor English. I cannot forget his

smile and lots of sweat on his face when he was showing me the construction site of nano- science and technology (NST) building (construction completed in 2006 and now called FNT) His face was filled with the joy of talking about his plans and dreams. After I joined his group, he always called me in my office and taught me many important things such as his philosophy and knowledge about science. Even the derivation of equations was sometimes discussed on a phone. Weekend was my favorite time to talk to him because he was less busy and so a bit more patient with me. Besides science, he often told me the story of his dogs, Marley and Punky. No matter how mad he was at my stupid replies to his questions, he could switch his mood completely when he started talking about Marley and Punky. I really have to thank Marley and Punky for saving me from many scary moments. "I have to go, bye", this is how he often suddenly hang up the phone even in the middle of conversation. One day, he was so worried about the future of science. He was telling me how great the Bell Lab and other research labs of industries were when Paul was young and that we lost them. After a while of discussion, he reached a conclusion, "Oh, but this is not my problem but you guys' problem. I won't be alive, hahaha. I have to go, bye." He was joking at the end, but he left me some feelings that he might have known some magic to solve the problem. Now it is really our problem to figure out. I just try hard to find the magic thought Paul might have had or find my own magic.

I like to thank Sharon and Juliet Barbara for sharing so many fun times with me. I cannot express how grateful I am for their kindness and honesty. We always joked about how crazy Paul was when he was alive. Now we always talk about the memories with Paul and what we can do without him. We miss him a lot no matter how crazy he was…I am learning lots of things from both Sharon and Juliet even after Paul died. I am really grateful for them.

I like to thank all the Barbara group members (called Barbarians). There were so many people who came and left during three and half years of my life in the Barbara group. Hsiao-Wei Liu, Wei-Shun Chang, Ya-lan Chang, Kwan-jik Lee, Jenny Ma, Yu-Shan Yeh, Donna Suk, John Grey, Rodrigo Palacios, Leonid Fradkin, Johanna Schmidtke, Ioannis Bounos, Yonjing Zhu, Hui Wang and Joshua Bolinger were in the group when I started and they helped me a lot to get started. Among the people in the Barbara group, I have special feelings for people who faced Paul's death with me in Austin. Joshua Bolinger, Matthew Traub, Rui Zhang, Song Guo, Johanna Brazard, Jan Vogelsang, Girish Lakhwani, Suhbadip Ghosh, Omar Fabian and Albert Lee. I also thank the secretary Ms. Sharon Bugnand and all the Barbara group alumni who supported us to go through tough time.

I like to thank for the students in the Vanden Bout group, Craig Cone, Dave Ostrowski, Katie Clark, Micah Glaz, Katie Walker, Leigh Krueger, Matt Wallack and Shauna Ingle, who kindly welcomed me and helped me for my transition. I also like to thank very kind and modest postdoc Dr. Zhongjian Hu who joined the group recently and worked with me closely to continue single molecule spectroscopy researches.

I had so many collaborators on various projects that I had opportunities to work with and like to thank for them. Professor Brian Korgel, Dr. Matthew G. Panthani, Dr. Vahid Akhavan, Dr. Brian Goodfellow, Professor Ananth Dodabalapur, Dr. Lawrence Dunn, Dr. Chris Lombaldo, Professor Allen Bard, Dr. Heechang Ye, Professor Venkat Ganesan, Dr. Paresh Chokshi, Dr. Benjamin Hanson, Professor Christopher Bielawski, Dr. Zicheng Li, Robert Ono, Professor Peter Rossky, Dr. Adam Willard, Professor Xiaoyang Zhu, Dr. Lei Shen, Professor Arumugam Manthiram, and Dr. B. Reeja Jayan.

I like to thank for all my friends in Austin. I cannot list all my friends' name here, but I had so much fun in Austin thanks for everyone. I want to show special thanks for

Omar Fabian, Jan Vogelsang, Johanna Brazard, Girish Lakhwani, Dave Ostrowski, Robert Ono, Eric Silver, Lauren Kang, Micah Glaz, Julian Villarreal and Selene Arrazolo for daily fun interactions.

I like to thank my first roommate Chris Griffith, his girlfriend Teresa Stewart and his mom Katrina Griffith (whom I call “mom” as well) for their kindness. I could not speak English well in the beginning of this graduate school and there were so many cultural differences I had to adjust to. My transition from Japan to Austin was so enjoyable and unforgettable thanks for their kindness and love. My first culture shock was when Chris grilled a pound of steak and gave it to me. It is like four times the size of typical steak you see in Japan.

I like to thank for Professor Hiroshi Masuhara, who suggested me to come to Austin and supported me since then. The first time I got the idea to come to USA, he was the only professor who gave me a big positive response and introduced me to Paul. Even after I left his group in Japan, he has always been a great supporter through my graduate school and his activities around the world always stimulated me to work harder.

Finally, I like to thank for Shiori Yamazaki. A book she gave me changed my life and made me challenge in USA. The long distance between Texas and Florida always made our relationship up and down, but still we have grown up together and shared many precious memories. I can never express enough how grateful I am for her and how important she is to me. She is a special person for my entire life.

Understanding of Conjugated Polymer Morphology Formation and the Structure-Property Relationships from the Single Chain Level to the Bulk Level

Takuji Adachi, Ph.D.

The University of Texas at Austin, 2012

Supervisor: David A. Vanden Bout

Morphology is the origin of life and function. Defining and designing morphology, understanding the relationship between morphology and function, is an essential theme in a number of research areas. In conjugated polymer research, the major obstacles to achieving these goals are the heterogeneity and complexity of conjugated polymer films. In the study presented in this dissertation, various single molecule spectroscopy techniques were used as an approach to minimize the complexity of these problems. By using excitation polarization spectroscopy, it was discovered that single chains of poly[2-methoxy-5-(2'-ethylhexyloxy)-1,4-phenylenevinylene] (MEH-PPV) assume a highly ordered rod conformation despite the fact that the morphology of bulk films is known to be amorphous. The comparison of results from experiments and a coarse grained bead-on-a-chain simulation suggested that single chains have the ability to use a thermally induced defect to maximize π-π stacking and adopt a rod conformation as a stable conformation. Bias-induced centroid spectroscopy (BIC) on highly ordered single chains demonstrated that the energy transfer scale could be an order of magnitude larger than the value typically measured for bulk films. It was further demonstrated that such an extraordinary long energy transfer was not a unique property of single chains but

was also observed in aggregates as long as the morphology was ordered. These studies were extended to another model compound poly(3-hexylthiophene) (P3HT) to generalize the mechanism of morphology formation and the structure-property relationship. For P3HT, it was shown that side-chains were a very important factor in determining single chain conformation, while the conformation of MEH-PPV was not affected by side-chains. By controlling the side-chains, both ordered and disordered P3HT chains were obtained. The comparison of results from experiments and an energy transfer model simulation quantified that energy transfer was at least twice as efficient in ordered chains as in disordered chains. In aggregates, the difference between the energy transfer efficiency of ordered and disordered morphology was even larger than that in the case of single chains. These results could suggest that there is a very fast energy transfer mechanism that occurs through interchain interactions when chains are packed in ordered fashion.

Table of Contents

List of Tables

List of Figures

Chapter 1: Introduction

Life is not eternal, which makes our time in this world so precious and beautiful. Although it also pushes us to keep moving forward, it does not mean one has to rush. "Don't rush! Stop! Think!" This is what Prof. Paul F. Barbara, one of the busiest people I know, always said to everyone.[1,2,3] It is indeed necessary to stop doing anything and carefully look around where you are and what you are doing. The modern life style in the 21st century can be described by two words, globalization and mass consumption. Too much information and too many substances surround us. Everyone easily ends up rushing and dismisses many important things. Stop and look around from many different points of view. There are a number of things which we take for granted every day. When I thought deeply and carefully looked around, I noticed one important fact: everything in this world has its own unique form or "morphology", and it is because morphology governs all functions. This philosophy is critical in science, and the structure-property relationship is a very important theme in any field of study. I aimed to gain deeper insight into this philosophy and devoted my whole dissertation to studying the morphology and function of conjugated polymers.

1.1 MORPHOLOGY

Morphology is an essential idea in this world. This term can be found in a wide variety of studies such as materials science, geoscience, biology and even linguistics. This is because morphology is the origin of function. By building a small unit of substances into larger structures, it often manifests new functions. Although it is not easy to clearly define when the "birth of morphology" occurs, the resulting function can be completely different depending on the way components are assembled, even if they are the same.

In linguistics, morphology is the study of the structure and form of words. Here, words are the building blocks; each sentence is assembled from many words. The meaning of sentences is dependent on how words are assembled into certain "morphologies". It is easy to realize that it is possible to deliver many different ideas by using the same set of words.

In natural science, molecules (or atoms) are the building blocks which are assembled into each substance. The function of a substance depends on how molecules are assembled into "morphology". Even if the same molecules are used to assemble into a structure, the structure's function can be completely different if the way it is assembled is varied. There are a number of astonishing examples in nature. For example, our body is made up of proteins which are assembled from amino acids, but there are only 22 kinds of amino acids. That is, the unique function of each of our body parts is achieved by assembling a small set of molecules in different manners.

It is amazing how nature has created such complex systems just by assembling a limited selection of parts and has found the structures that manifest the desired functions. Darwin's theory states that "natural selection" is the key to evolution. There are always random genetic errors which modify the morphology and function of creatures. If the modified morphology and function of a certain species is specially adapted to an environment, the species becomes superior to others and dominates the environment. If evolution really relies on random trials and errors, it takes an unimaginably long time until a desired function is obtained. In fact, it has been a controversial topic whether evolution by random trials and errors is fast enough to create advanced forms of life.[4-8] However, with or without the answer to this question, it is obvious that evolution can be accelerated if one could avoid randomness and direct the trajectories of evolution.

After wandering into the mysteries of nature, it is clear to me that there is much materials scientists can learn. Morphological control is critical because morphology governs life and there is a structure that manifests a desired function. The ultimate goal of materials science should be determining how to control morphology not by random trials and errors but by understanding the structure-property relationship so as to accelerate the speed of progress. When we find out the key to controlling morphology and function, a rational materials "evolution" should begin.

1.2 MORPHOLOGY AND FUNCTION IN CONJUGATED POLYMERS

A research field that requires the immediate achievement of this goal is that of conjugated polymers. Conjugated polymers are organic semiconductors that are soluble in organic solvents. Films of conjugated polymers can be used for "plastic electronics"[9] such as solar cells,[10-12] light-emitting diodes[13-15] and field effect transistors[16,17]. Energy shortage is a critical problem in modern society. Because this material is suited for fabricating cheap and large scale devices, the commercially profitability of these devices is expected to be extremely high. This will happen as soon as we find the "key" to control morphology and function.

The functions of conjugated polymers are strongly dependent on polymer morphology. This is because π-electrons are delocalized along the backbone of polymer chains and chain-chain interactions (i.e. intra- and interchain interactions) critically modulate the electronic states of these materials.[18] There have been a number of studies to control the morphology and function of conjugated polymers and thereby improve the performance of devices.[19-21] Figure 1.1 illustrates a schematic overview of conjugated polymer research, which emphasizes the importance of the supramolecular assembly of polymer chains.[19]

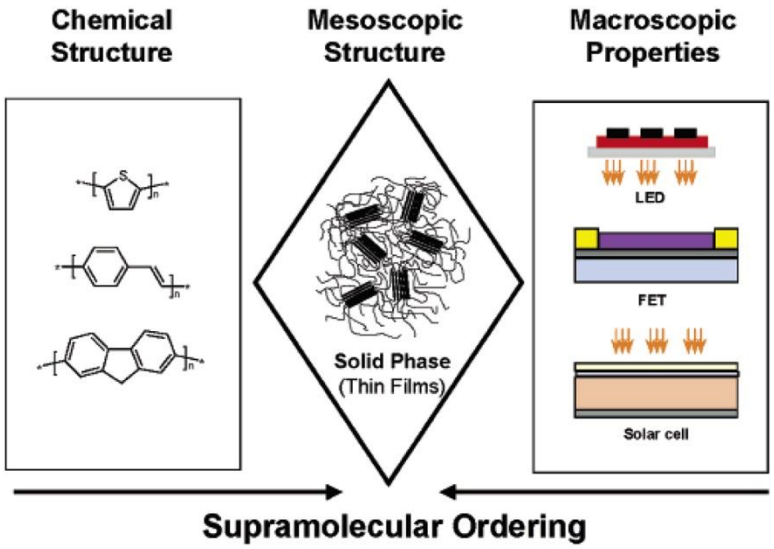

Figure 1.1: A schematic overview of conjugated polymer researches. The control of solid phase morphology is the key parameter to optimize the function of films and devices. (Copied from Ref 19)

Figure 1.2 and 1.3 show examples of how morphology affects function. Conjugated polymer films are prepared through solution processing methods such as spin-casting and printing. During the evaporation of organic solvents, chains are packed into a neat solid film. The morphology of the resulting films can be varied by adjusting many factors such as the type of solvent used for processing[22], the coating conditions (temperature and rate)[21,23,24], the molecular weight of the polymers[20,25-27], the distribution of molecular weight[28,29], and the chemical structure of the polymers[30,31]. Figure 1.2A and B shows atomic force microscopy (AFM) images of polymer films demonstrating how the molecular weight of polymers affects the film morphology.[20] Figure 1.2C shows the change in charge mobility as a function of molecular weight and processing conditions.[20] Figure 1.3 demonstrates that the small modification of the chemical structure of the polymers changes the film morphology, which results in a large shift of the peak of the photoluminescence spectrum.[30] These results strongly indicate that the optimization of any function cannot be achieved without understanding how to control morphology.

The major obstacle to establishing a quantitative understanding of how to control morphology and how morphology affects function is the heterogeneity and complexity of polymer morphology.[32,33] The morphology of conjugated polymer films is formed by three dimensional polymer networks consisting of a number of individual chains. It is almost impossible to form a homogeneous supramolecular structure during film processing because of the flexible nature of chains and the relatively less selective and directional molecular interactions (π-π interactions) of conjugated polymers. As a result, a bulk polymer film tends to consist of a distribution of nano-scale polymer domains. Polymer domains with a wide distribution of size and shape can be observed from the AFM images shown in Figure 1.2 and 1.3. Not only are the shape and size altered but the crystallinity of each domain is also varied[32,34]. When an ensemble characterization

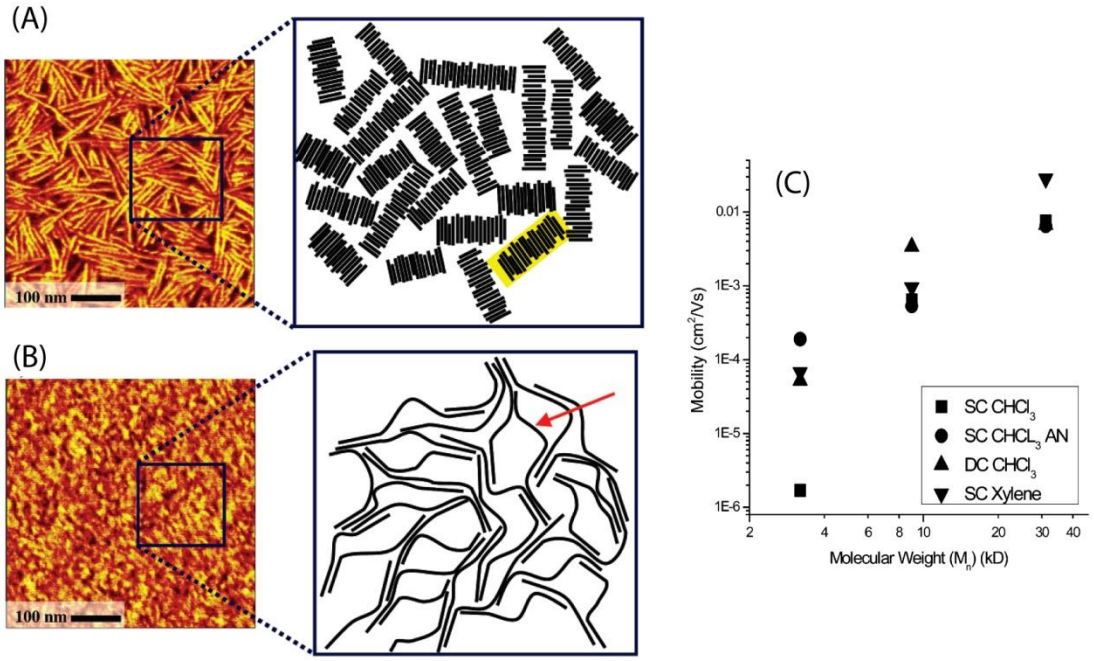

Figure 1.2: Atomic force microscopy phase images of polymer films made from (A) low molecular weight (<4kDa) and (B) high molecular weight (>30kDa) poly(3-hexylthiophene). (C) Comparison of the change in charge carrier mobility for three different MWs as the processing conditions are changed. Samples are spin-cast (SC) from chloroform, annealed (AN), drop-cast (DC), or spin-cast from xylene. (Reproduced from Ref 20)

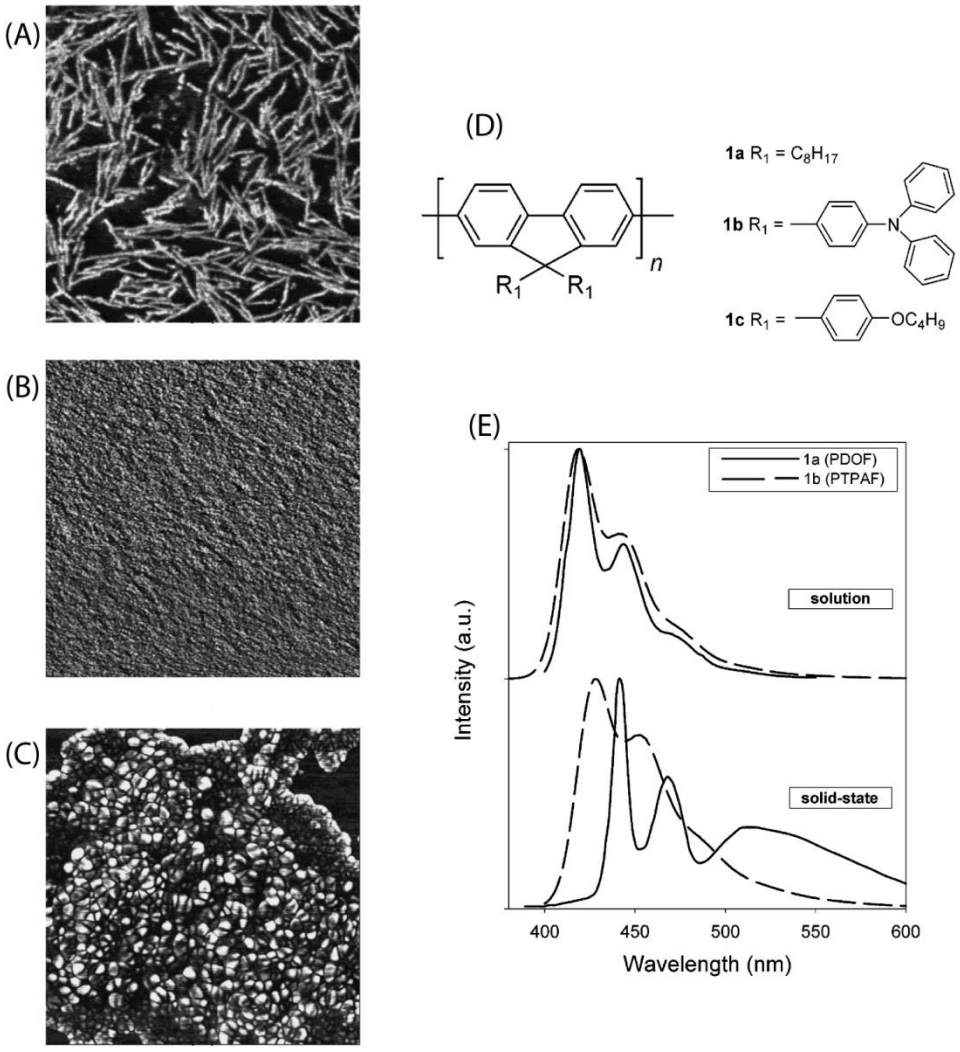

Figure 1.3: Atomic force microscopy phase images of thin films of (A) poly(9,9-dioctylfluorene) (PDOF, 1a), (B) poly(9,9-ditriphenylaminefluorene) (PTPAF, 1b), and (C) 1c. Chemical structures are shown in (D). (E) Photoluminescence spectra of PDOF (1a, full line) and PTPAF (1b, dashed line): (top) solution spectra (in chloroform); (bottom) solid-state spectra. (Reproduced from Ref 30)

method is used to define the morphology or function of films, it only measures an average property of this heterogeneous morphology of nano-domains.

The heterogeneity and complexity of film morphology and function further increases when films are made from a blend of more than two polymers[35-37] or a polymer and another molecule (e.g. fullerene)[10,31,38,39]. Typically, such blend films are important for light-emitting diode or solar cell applications. Figure 1.4 shows topography images and the solar cell efficiency of local nano-domains probed by photoconductive AFM.[39] The results clearly show the heterogeneity of film morphology and the necessity for optimizing the film morphology.

1.3 SINGLE MOLECULE SPECTROSCOPY FOR CONJUGATED POLYMER RESEARCHES

As previously mentioned, the heterogeneous and complex nature of conjugated polymer films has been major obstacles to quantitatively defining the morphology and function. For both experimental and theoretical approaches, it is difficult to establish a reasonable model for bulk films due to these obstacles. A successful approach to simplify these problems is the study of single chains (or aggregates). Single molecule spectroscopy has been proven to be a powerful technique to revealing various fundamental properties of conjugated polymers that could not be achieved by ensemble characterization methods.[40-44] Also, the comparison between the results of experiments and a theoretical simulation is relatively easy because the size of objects for the simulation can be much smaller than that of bulk films.[45-47] In this dissertation, the first goal is to defining the morphology and function of single conjugated polymer chains, in which intrachain interactions are important parameter. Then, the second goal is to increasing the size of object from single chains to single aggregates so that the effect of interchain interactions can be quantified. It is a great advantage to be able to distinguish

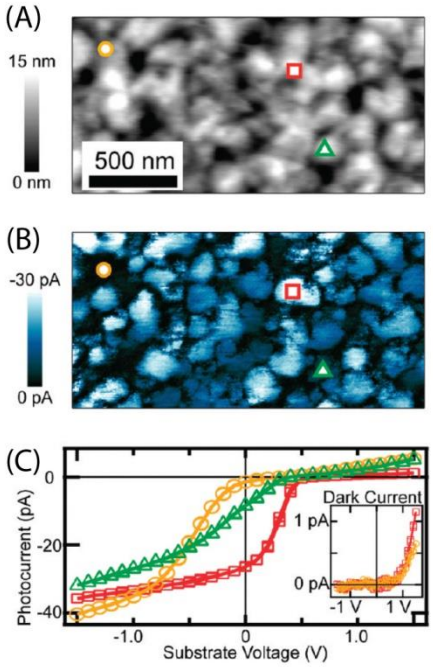

Figure 1.4: (A) AFM height image of a blend film of poly(2-methoxy-5-(3',7'-dimethyloctyl-oxy)-1,4-phenylenevinylene) (MDMO-PPV) and [6,6]-phenyl-C61-butyric acid methyl ester (PCBM), (B) photocurrent map measured with zero external bias and (c) local current-voltage data acquired at the three locations indicated by the symbols in panels A and B. Inset shows local current-voltage data without illumination showing smaller dark currents. (Reproduced from Ref 39)

the property of intra- and interchain interactions in quantifying the structure-property relationship. This strategy enables us to control the level of complexity, which is necessary to establish the complete picture of conjugated polymers.

1.4 BASIC PHYSICS OF CONJUGATED POLYMERS

The certain basic understandings of conjugated polymers have been established by the study of the polymers in solutions, which is less complicated compared to that in bulk films. A conjugated polymer is a long chain of molecules which can be divided into two parts, "backbone" and "side-chain". The backbone of conjugated polymers is made of π-conjugated systems. π-electrons are delocalized over the backbone of polymers and the length scale of the delocalization is called "conjugation length". Conjugation length determines the electronic structure of the materials such as the highest and lowest occupied molecular orbital (HOMO and LUMO) and the gap between the HOMO and LUMO level (Figure 1.5). The side-chain of conjugated polymers is attached to make conjugated polymers soluble in various organic solvents. This is a great advantage for the commercialization of organic electronic devices because films can be fabricated by cheap solution processes.

Model compounds studied in this dissertation is poly[2-methoxy-5-(2'-ethylhexyloxy)1,4-phenylenevinylene)] (MEH-PPV) and poly(3-hexylthiophene) (P3HT). The chemical structure of these compounds is shown in Figure 1.6. In MEH-PPV, π-electrons are delocalized over the alternating single and double bonds of phenylenevinylene backbones. In P3HT, π-electrons are delocalized over the alternating single and double bonds and sulfur atoms of thiophene rings. For the samples used in this dissertation, the number of repeat unit per chain is from hundreds to thousands depending on the molecular weight of the polymers used in each chapter.

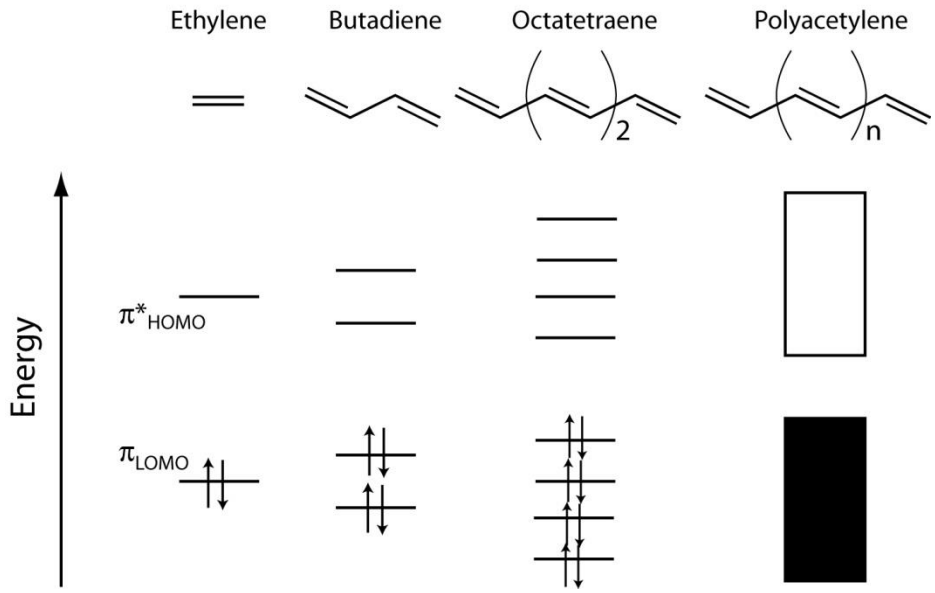

Figure 1.5: Molecular orbital of polyene series. HOMO-LUMO energy changes as the function of conjugation length of the polymer.

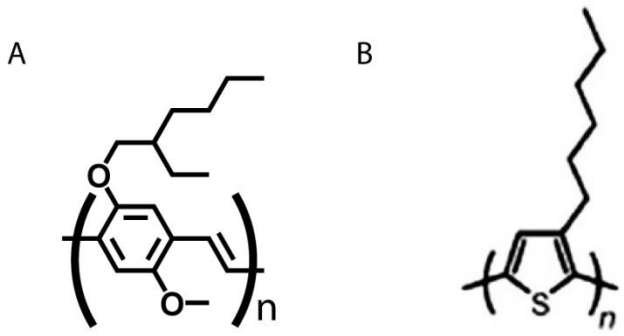

Figure 1.6: Chemical structure of (A) MEH-PPV and (B) P3HT

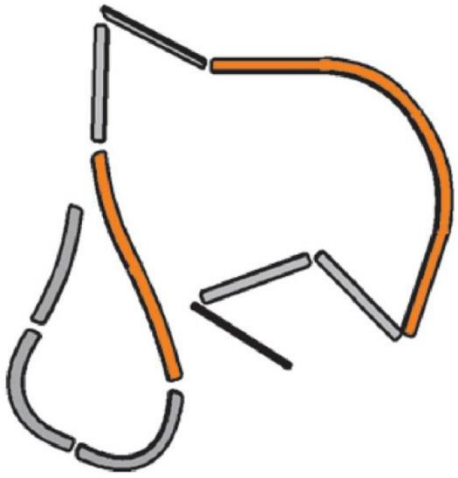

Figure 1.7: A cartoon of conjugated polymer chain which represents the distribution of conjugation length of chromophores. Longer conjugation is represented by the orange color. (Copied from Ref 48)

The question that is often asked about these materials is regarding the definition of conjugation length.[49,50] For an MEH-PPV chain with molecular weight of 1,000 kDa, the physical length of the chain can be as long as two micrometers if the chain is completely stretched. Do π-electrons delocalize over the entire chain? The answer for this question is "no", and this is because there are conformational defects such as torsion and bend of a chain or chemical defects that disrupt the delocalization of π-electrons.[51] As results, a chain is divided into many individual conjugated segments that are called "chromophores". It has been shown that the conjugation length of each chromophore and the distribution of the chromophore length depend on a chain conformation.[51-53] Figure 1.7 shows a typical cartoon of a conjugated polymer chain, representing the distribution of chromophores length.[48]

The particular function discussed throughout this dissertation is how conjugated polymers interact with light and how morphology affects the interaction. Key fundamental ideas are the absorption and emission of light and the energy transfer between chromophores. In physical chemistry, these ideas are treated quantum mechanically and the detailed descriptions can be found in a number of books.[54,55] Here, I limit the introduction of the ideas in qualitative manners. When energy of light is sufficient to rearrange the distribution of electrons of molecules from the lowest energy state "ground state (S_0)" to a higher energy state "excited state (S_n)", the energy is transferred to molecules from light. This is called absorption. The absorbed energy can be released by several paths such as the internal conversion (heat), spontaneous emission (fluorescence) and intersystem crossing. A simple diagram of these processes is shown in Figure 1.8. The absorption and fluorescence can be probed by spectroscopy and these spectra are often mirror image of each other (Figure 1.9).

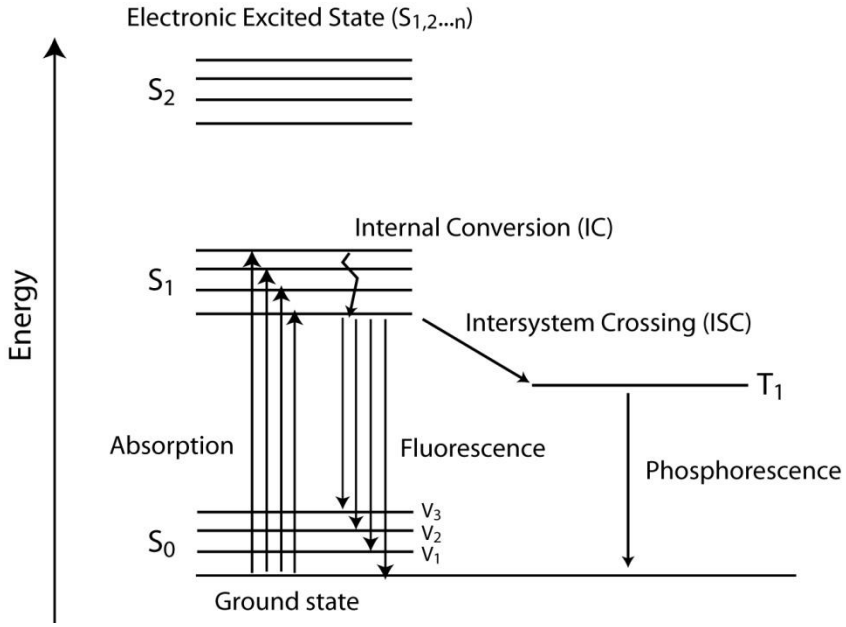

Figure 1.8: A simple Jablonski diagram representing a electronic states and various transitions between states.

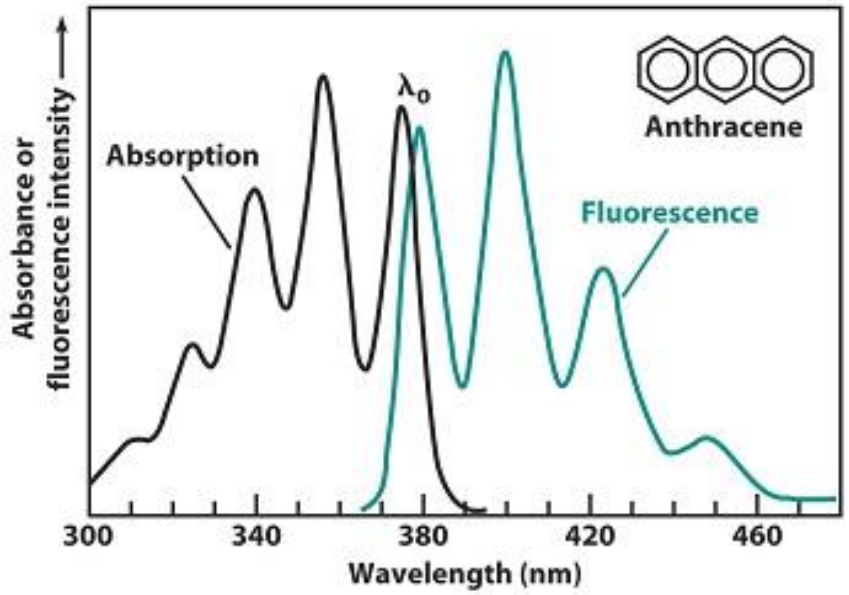

Figure 1.9: Absorption and emission spectrum of anthracene. This is a good example showing a mirror image relation of absorption and emission. (Copied from Ref 56)

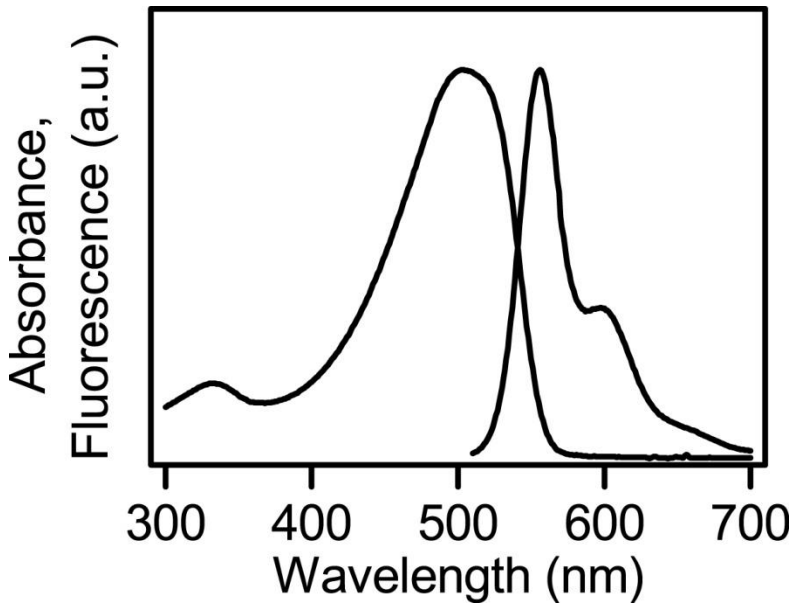

Figure 1.10: Absorption and emission spectrum of MEH-PPV (Molecular weight of 900kDa from Polymer source Inc.)

In conjugated polymers, chromophores along a chain interact with lights individually. Chromophores absorb light and the absorbed energy is released by any process listed in Figure 1.8. Figure 1.10 is the absorption and fluorescence spectra of MEH-PPV. A broad distribution of chromophore length along a chain is reflected in a broad and featureless absorption spectrum. Compared to the absorption spectrum, the fluorescence spectrum is relatively narrower and possesses a clear vibronic feature. This is often explained by energy transfers occurring between chromophores, which funnel energy down toward fewer numbers of sites and emit from there.[51]

During the lifetime of an excited state, the energy due to light absorption can be transferred between chromophores (Figure 1.11). The energy transfer process occurs through resonant dipole-dipole interactions between chromophores and is often described by a model based on the Förster resonant energy transfer (FRET). FRET model is mostly used to describe the energy transfer between two dye molecules and the rate can be calculated as follows:

$$t = \frac{9(\ln 10)\kappa^2 J}{128\pi^5 n^4 N_A} \frac{Q_0}{\tau} \frac{1}{r^6} \tag{1.1}$$

where Q_0 is fluorescence quantum yield of donor in the absence of acceptor, τ is the fluorescence lifetime of κ is the dipole orientation factor, J is the spectral overlap calculated as

$$J = \int f_D(\lambda)\varepsilon_A(\lambda)\lambda^4 d\lambda \tag{1.2}$$

where f_D is the normalized donor emission spectrum and ε_A is the molar extinction coefficient. In these expressions, λ is the wavelength, N_A is the Avogadro's number, n is the refractive index. Because the conjugation length of chromophores is longer than that of dye molecules, one needs to be careful for how to treat dipoles in a simulation. Further discussions on whether the simple FRET model is appropriate for conjugated polymers can be found in Chapter 7. In any case, energy transfers between chromophores

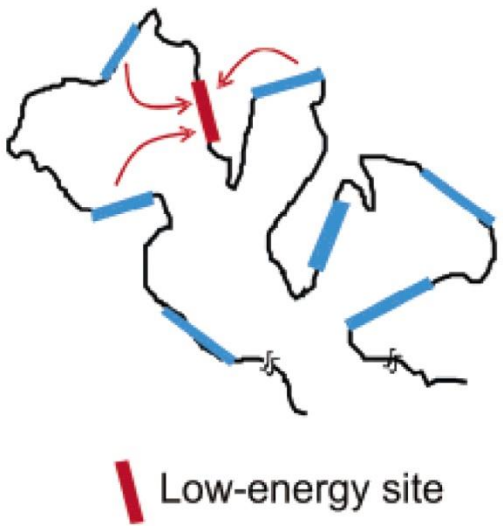

Figure 1.11: A cartoon representing energy transfers in a conjugated polymer chain. Energy flows from higher energy chromophores (blue) to lower energy chromophores (red). (Copied from Ref 40)

are an important function of conjugated polymers, and understanding how morphology affects energy transfer processes is one of the main themes in this dissertation.

1.5 PROPERTY TRANSITION OF CONJUGATED POLYMERS FROM SOLUTION TO SOLID PHASE

Conjugated polymers in sold phase can be thought as a completely different theme of study from that in solution phase. There are a number of things which need to be redefined such as the electronic structures of the polymers, the conjugation length of chromophores, energy transfers between chromophores and so on. The major cause of these property changes from solution to solid phase is the effect of interchain interactions.[18,57] As the density of chains increases from solution to solid phase, the main parameter that determines the polymer properties shifts from intrachain to interchain interactions. The interactions of chains in films are strongly affected by the morphology of conjugated polymers. However, as previously mentioned, the complexity and heterogeneity of morphology make it difficult to quantify the structure-property relationship in films. Despite these obstacles, there have been many experimental and theoretical studies that tried to understand the physics of conjugated polymer films because of the application for organic electronics. Herein, I introduce a few examples of property differences between solution and solid phase, and point out major questions that are still remained unanswered.

The absorption and fluorescence spectra of conjugated polymer films are one of good examples.[58-60] Figure 1.12 shows the absorption and fluorescence spectra of P3HT in solution (in chlorobenzene) and as a film.[59] A significant red-shift from the solution to film is observed in both the absorbance and fluorescence spectra. In addition to the red-shift, the vibronic feature of absorption spectrum becomes clearer in the film, and the

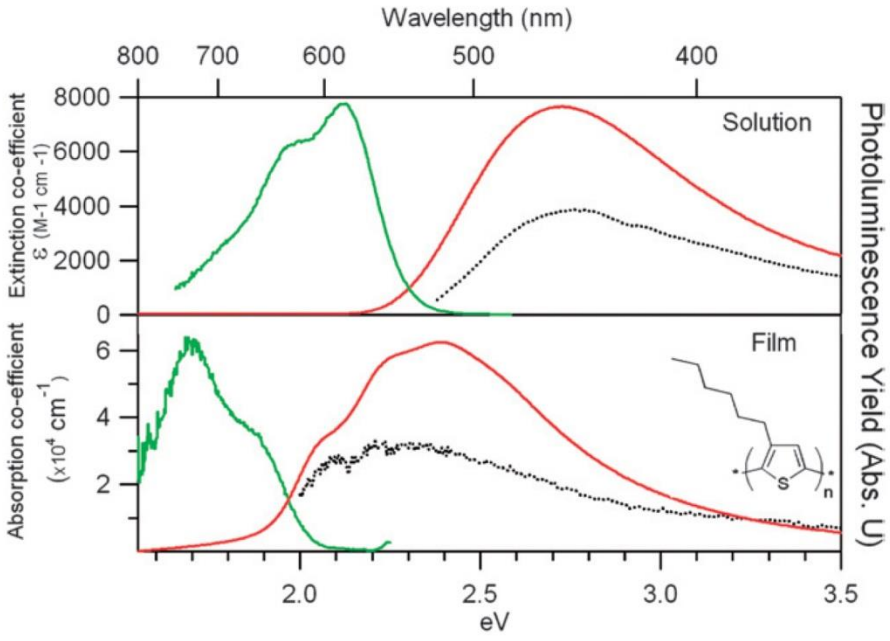

Figure 1.12: (top) Absorption extinction co-efficient (red line), excitation spectrum (dotted black line) and emission spectrum (green line) for 93% regioregular P3HT in solution at $4x10^{-5}$ mol l^{-1} concentration. Note extinction co-efficient refers to moles of the P3HT monomer unit (Mw 169) (bottom) Absorption co-efficient (red line), excitation spectrum (dotted black line) and emission spectrum (green line) for the 93% RR P3HT film. Film thickness is ~80 nm. Excitation wavelength for emission spectra was the absorption peak maximum while excitation spectra were taken at the emission maximum. Chemical structure of the P3HT monomer is given as an inset. (Reproduced from Ref 59)

ratio of the 0-0 and 0-1 transition peaks of the fluorescence spectrum changes. The magnitude of the red-shift and the change in spectral shape from solution to solid phase can be varied between different polymers, but these trends are general in many conjugated polymers. However, the mechanism of these changes has not been fully explained yet.[58,61]

The important question is regarding how the delocalization of electronic states changes from solution to solid phase. Earlier, I introduced the idea of chromophores (section 1.4) and that the conjugation length of chromophores depends on a chain conformation. The observed red-shift of these spectra may be due to the extension of chromophore length, because chains can be more planarized by dense packing of chains in films. However, another explanation for the red-shift may be that emission occurs from new species that arises from strong interechain interactions, the character of which might be similar to "excimer" or "exciplex" observed in dye aggregates. Whether electronic states delocalize over only one chain or multiple chains is critical in understanding the electronic structures and property of these materials.

In addition to these spectral changes, the quantum yield of fluorescence decreases wildly from solution to solid phase.[59,62-64] For the case of P3HT, it is reported that the quantum yield decreases from 0.33 to 0.02.[59] Everyone agrees on that the rate of non-radiative decay is much faster in film than in solution. However, the detail of this non-radiative decay is unknown and there have been multiple hypotheses. One hypothesis is that there is an intrinsic quencher along a chain and the quenching of the fluorescence increases as the density of chains near the quencher increases.[65,66] Another hypothesis is that strong interchain interactions modify the electronic state of the polymers and some type of non-emissive state (such as charge transfer state) becomes a competitive pathway for energy to decay through.[59,67,68] A suggested energy diagram is shown in Figure 1.13.

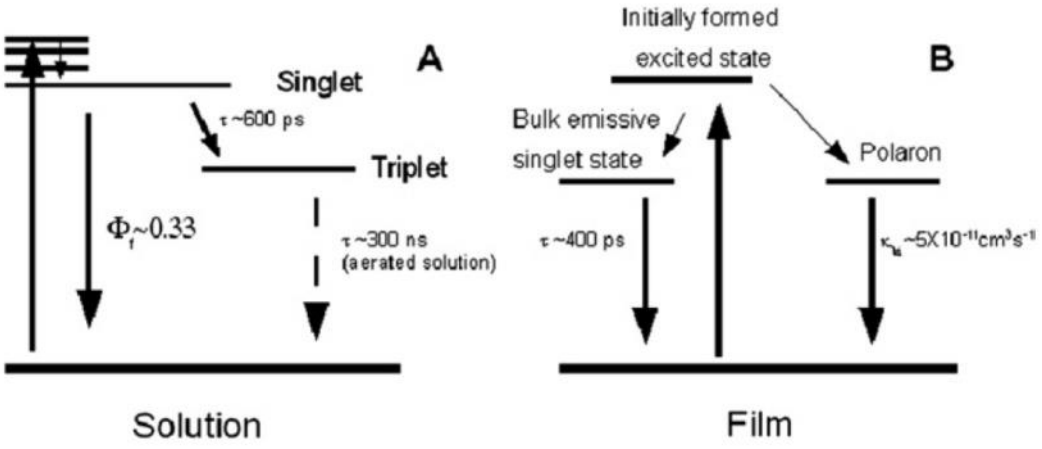

Figure 1.13: Energy diagrams for P3HT in solution (A) and in film (B). For the film sample the polaron state (charge transfer state) provides a competitive pathway to emissive state formation thereby reducing the fluorescence efficiency of P3HT in films. (reproduced from the Ref 59)

In addition to the answers for these questions, energy transfer models can be treated differently depending on how to treat the electronic states of conjugated polymer films. In general, energy transfer models for conjugated polymers have been developed based on the study of the polymers in solution.[69-71] In these models, chromophores are defined along a chain, and no effect of interchain interactions on delocalization of electronic states has been considered. If electronic states are delocalized over multiple chains, these models need to be modified. Furthermore, dense packing of chains in solid films increases the number of available acceptor sites for energy to migrate to compared to the case of solution. Overall, the energy transfer models in 3-D dense polymer networks of solid films most likely require some modification from the models developed for chains in solution.

To summarize this section, major questions that need to be answered are following: 1) How does the definition of chromophores change from solution to solid phase? When chains are closely packed, do electronic states simply delocalize over a longer segment on one chain or delocalize over multiple chains? 2) What is the mechanism for the decrease of fluorescence quantum yield from solution to solid phase? Do interchain interactions change the energy landscape of electronic states and the decay path of absorbed energy? 3) What is a good model for energy transfer occurring through multiple chains in solid films? By using single molecule spectroscopy approach, I aimed to find the answers for these questions as much as possible.

1.6 EXPERIMENTAL SETUP

Throughout this dissertation, various experimental methods were invented to reveal yet unknown fundamental property of conjugated polymers. The details of each method will be described in following chapters, and only the basic of the setup is introduced here.

Samples for single molecule spectroscopy were prepared as follows. Isolated chains of conjugated polymers embedded in poly(methyl methacrylate) (PMMA) matrix were obtained by dynamically spin-coating very low concentration (10^{-13} $molL^{-1}$) of conjugated polymers in PMMA/Toluene solution. The final thickness of these films was measured as 200 nm with a final spot density of 0.1 spots/μm^2. In order to avoid any photooxidation of samples, they were prepared and sealed using epoxy resin (GC electronics, 2 Part Epoxy Glue) and a glass coverslip in a glove box (MBraun, with O_2 and H_2O less than 5 ppm) and investigated in the microscope apparatus within a few days after the sample preparation in order to avoid penetration of oxygen or moisture into the sample through leaks in the seal.

Confocal and wide-field microscopy setups were built based on an inverted microscope (Zeiss, Axiovert 200) with a 1.25 NA objective lens (Zeiss, Achrostigmat, 100X). Ar-Kr ion laser (Melles Griot, model 35 LAL-030-208) was used as an excitation source. A prism was used to separate individual laser lines and 488-nm line was used for most experiments. The excitation beam was further cleaned by a laser line filter (Chroma) and sent to a sample by using a dichroic mirror (Semrock). The excitation scattering light from the sample was blocked from the detector path using a dichroic mirror and a 488-nm notch filter (Chroma). The scheme of confocal and wide-field microscopy is shown in Figure 1.12 and 1.13 respectively. The first difference between two microscopy techniques is the excitation beam path. For confocal microscopy, the excitation beam is collimated to the back aperture of an objective lens and a diffraction limited focused spot on a sample is achieved. While a focused beam spot was scanned through a sample by using a piezo electric stage, fluorescence signals were detected by an avalanche photo diode (APD, Perkin-Elmer Optoelectronics SPCM-AQR-15) and its output was read by a multichannel scalar board (MCS, Becker Hickl PMS-400). By synchronizing a piezo

stage and a fluorescence signal of APD, a fluorescence image was constructed. After constructing an image, a beam spot can be sit on a molecule and either fluorescence transient was recorded or fluorescence spectrum of individual molecule was obtained by using a spectrograph (Acton SP-150) combined with a liquid N_2 cooled charge coupled device (Princeton Instruments, Spec-10 CCD). On the other hand, for wide-field microscopy, the excitation beam is focused on a back aperture of an objective lens and a collimated beam is sent to a sample. The illumination area of ~40 μm was obtained, and a whole image was sent to an electron multiplying CCD (EMCCD, Andor, model iXon$^+$ DU-897E). A series of images at a same area can be acquired and image analysis was performed by using a home-written MATLAB program to extract information such as fluorescence transient of individual molecules. A flipping mirror was used to switch between confocal and wide-field microscopy setup.

1.7 DISSERTATION OVERVIEW

Chapter 2 describes the morphology of single MEH-PPV chains. Single molecule fluorescence excitation polarization spectroscopy was used to probe the excitation anisotropy of individual molecules in the x-y plane of a lab frame. Detailed analysis of the experimental results shows that the polymer chain conformation of nearly defect-free MEH-PPV is surprisingly ordered and elongated in a rod structure. In bulk films, MEH-PPV has been known to assume amorphous morphology. To further gain the insight of morphology formation, the comparison of the experimental results to coarse grain bead-on-a-chain simulation was performed with the aid of Professor Venkat Ganesan and Dr. Paresh Chokshi. The results suggested that single MEH-PPV chains possibly possess the ability to thermally induce bending defects at optimal locations to achieve highly anisotropic rod conformation.

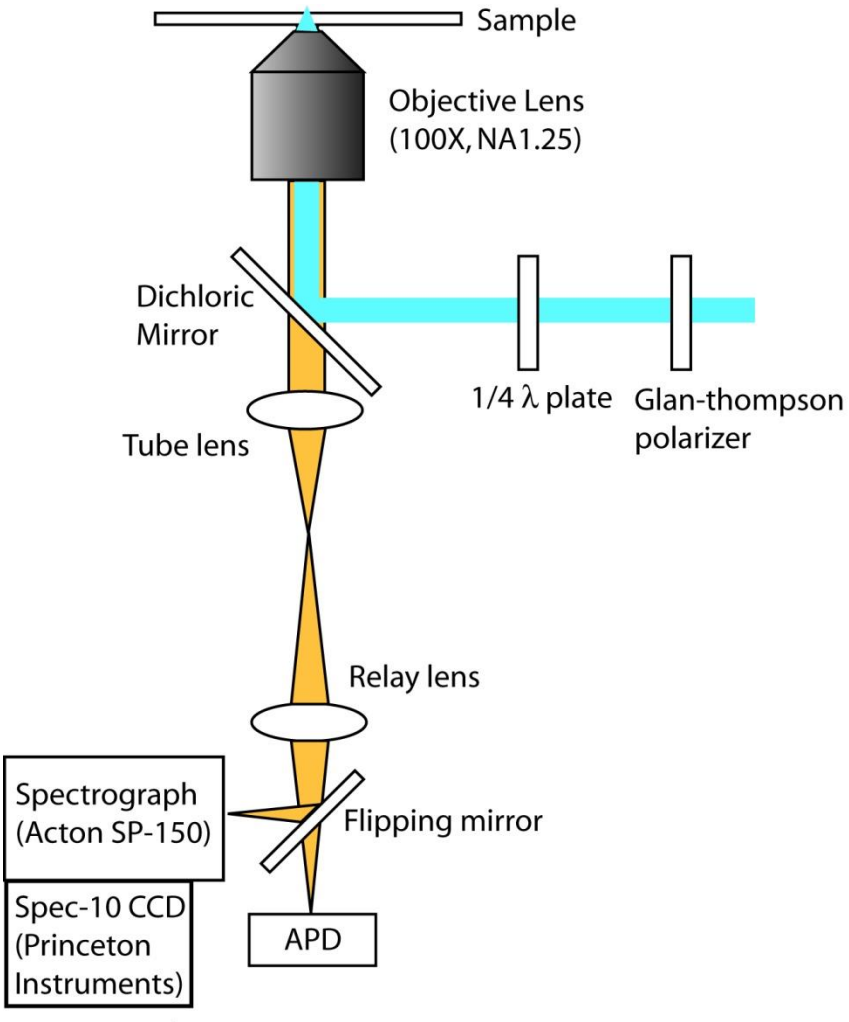

Figure 1.14: A basic confocal microscopy setup used in this dissertation

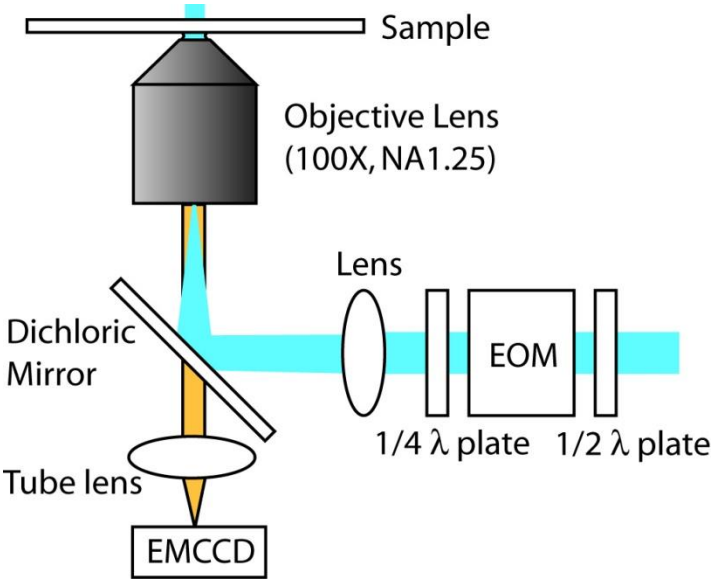

Figure 1.15: A basic wide-field microscopy setup used in this dissertation

Chapter 3 describes the solvent vapor annealing (SVA) of single MEH-PPV chains. As described in chapter 2, single chains of MEH-PPV fold into highly ordered rod conformations. A question raised from this result was whether these conformations are in an equilibrium state (the lowest energy conformation) or not. SVA is known to assist polymer films to reach lower energy state if an appropriate solvent were used. A unique point of the study in this chapter is that the microscopy imaging of single chains is done during the annealing. It was observed that the conformation of MEH-PPV chains was the same before and after annealing, and therefore it was concluded that the self-folding of single MEH-PPV chains into equilibrium conformation during a spin coating process is very efficient. Furthermore, the real-time observation of SVA process at the single molecule level made it possible to follow the morphological dynamics such as the folding/unfolding and translations of chains.

Chapter 4 describes the distance scale of energy transfer in highly ordered single MEH-PPV chains. The quenching of excitons by hole polarons was used as a mean to characterizing energy transfer distance. Real-space measurements of the distance scale for exciton/polaron quenching in a bulk film has been limited due to the insufficient resolution of conventional far-field fluorescence microscopy. The visualization of exciton quenching induced by hole polarons in single-polymer chains in a device geometry was achieved. The distance-scale for quenching was measured by means of a new subdiffraction, single-molecule technique—bias-modulated intensity centroid spectroscopy—which allowed the extraction of a mean centroid shift of 14 nanometers for highly ordered, single-polymer chains. This shift requires energy transfer over distances an order of magnitude greater than previously reported for bulk conjugated polymers and far greater than predicted by the standard mechanism for exciton quenching, the unbiased diffusion of free excitons to quenching sites. Instead, it was

suggested that multistep "energy funneling" to trapped, localized polarons is the probable mechanism for polaron-induced exciton quenching.

Chapter 5 describes the distance scale of energy transfer in highly ordered MEH-PPV aggregates. When the extraordinarily long-range energy transport was observed (Chapter 4), an important question was raised as to whether these characteristics are sustained when conjugated polymer chains agglomerate into a neat solid. A solvent vapor annealing with carefully chosen solvents made it possible to control polymer aggregation process. As a result, aggregates with volumes of at least 45,000 nm^3 (molecular weight ~ 21MDa) maintain a highly ordered morphology and show pronounced fluorescence blinking behavior, indicative of substantially long-range energy transport. Based on a simple energy transfer model simulation, it was shown that an average energy transfer scale of 25-30 nm up to 60 nm was necessary to reproduce such observations. Along with Chapter 4, it was concluded that the extraordinarily energy transfer was only present in highly ordered morphologies; this finding emphasizes the importance of the control of morphology.

Chapter 6 describes the effect of side-chains on morphology control. The same technique as Chapter 2 was used to characterize the conformation of single P3HT chains with different degree of regioregularity (*i.e.*, the percentage of head-to-tail linkages between monomer units in the polymer backbone) that were given from Professor Christopher W. Bielawski and Mr. Robert Ono. It was known that side-chains affect the morphology of bulk films through the control of interchain interactions. However, the role of side-chains in the absence of interchain interactions was not well defined. Especially, it was shown that MEH-PPV folds into highly ordered conformation even for regiorandom samples (Chapter 2), which indicates that side-chains might not affect single chain conformations. The results showed that the regioregularity controls the morphology

of P3HT even at the single chain level. While every regioregular (*rr*-) P3HT chain within an ensemble was found to fold into a highly ordered conformation, single regiorandom (*rra*-) P3HT chains adopted a wide variety of conformations, ranging from highly ordered to isotropic. Molecular dynamics simulation on atomistic models of *rr*- and *rra*-P3HT chains (with the aid of Professor Venkat Ganesan and Dr. Benjamin Harrison) supports the effect of regioregularity on the collapsed conformations. The difference between MEH-PPV and P3HT suggests that the role of side-chains in morphology control might be dependent on the density of side-chains along a backbone.

Chapter 7 describes the morphological effect on the efficiency of energy transfer in single conjugated polymer chains. As shown in Chapter 4 and 5, energy transfer scale in highly ordered morphology is extraordinary long. The goal of this chapter was to quantify the difference of energy transfer efficiency between ordered and disordered conformations. P3HT with different degree of regioregularity was used as model compounds for the ordered and disordered conformations (Chapter 6). Single molecule fluorescence spectra and excitation/emission polarization anisotropy of individual molecules were compared with a Förster Resonance Energy Transfer (FRET) model simulation. These studies showed that ordered conformations facilitate efficient energy transfer to a smaller number of low energy sites compared to disordered conformations. As a result, the histograms of spectral peak wavelengths for ordered conformations were centered at much lower energies than those obtained for disordered conformations. Collectively, these experimental and simulated results provide the basis for quantitatively describing energy transfer in conjugated polymers.

Chapter 8 describes the morphological effect on energy transfer in conjugated polymer aggregates. The major difference between single chains and aggregates is the contribution of interchain interactions. When single chains of *rr*- and *rra*-P3HT were

assembled into aggregates by using SVA method described in Chapter 5, highly ordered and disordered aggregates were successfully prepared, respectively. This result demonstrated that the SVA induced aggregation can be used not only for MEH-PPV and for other materials. The morphological difference between *rr*- and *rra*-P3HT was even more significant for aggregates than for single chains (Chapter 6 and 7). The fluorescence transients of ordered and disordered aggregates showed drastic difference. While *rr*-P3HT aggregates showed pronounced blinking, *rra*-P3HT aggregates never showed a blinking. Instead, the fluorescence transients of *rra*-P3HT aggregates showed continuous decay in the presence of quenchers such as oxygen. These results support the conclusion from Chapter 7 that states that energy transfer is more efficient in ordered conformations than in disordered conformations. Additionally, it was quantified that the morphological effect on energy transfer was larger for the case of aggregates compared to that for single chains. These results may imply the existence of fast energy transfer mechanism through interchain interactions. That is, when chains are packed in ordered fashion, absorbed energies may travel much faster between chains than along a chain.

Chapter 9 describes the outlook of the morphology study in conjugated polymers.

Chapter 2: Highly Ordered Single Conjugated Polymer Chain Rod Morphologies

This chapter was reproduced in part from: Adachi, T.; Brazard, J.; Chokshi, P.; Bolinger, J. C.; Ganesan, V.; Barbara, P. F. *J. Phys. Chem. C* **2010,** *114, 20896*

2.1 INTRODUCTION

Many of the most important questions in conjugated polymer research are concerned with polymer morphology.[72] How to measure and to define polymer morphology, how to synthetically control polymer morphology, and how polymer morphology affects function, remain mostly unanswered. A major obstacle toward answering these questions is the complex and highly heterogeneous molecular level structure of conjugated polymer materials.[73] In order to simplify morphological research on conjugated polymers and thereby to make it tractable, our group has developed the investigation of single conjugated polymer chain morphology as a simple model system in this area of research.[40-42,47] For single chains, morphology and conformation essentially have the same meaning. For example Hu *et al.* showed that single molecule fluorescence excitation polarization spectroscopy on isolated conjugated polymer chains can be used to characterize the morphological order of a single polymer chain through the polarization excitation anisotropy, A.[47] This quantity can be simply related to the order parameters, S_c, of the polymer chain conformation as follows.

$$S_C = \frac{1}{2}\left\langle 3\cos^2\beta - 1 \right\rangle \tag{2-1}$$

$$A = \frac{3S_C}{2 + S_C} \tag{2-2}$$

where β is the angle between each segment and the polymer principal internal axis.[74,75] For the prototypical conjugated polymer MEH-PPV, a broad histogram of anisotropy values was observed ranging from nearly zero anisotropy values to a value approaching

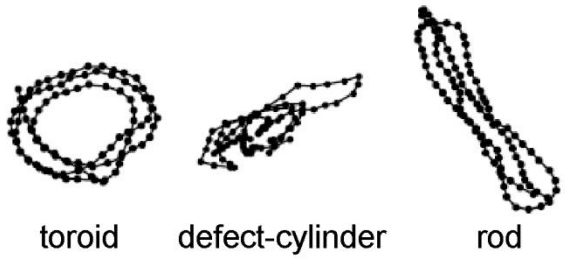

Figure 2.1: Three conformations of a 100-segment homopolymer generated by Monte Carlo simulations. This figure was adapted from Hu et al..[47]

0.8.[47] These data proved that the flexible chain model is incorrect for conjugated polymers and instead a certain degree of parallel chain nematic-like order was required by the experimental data. However, the observed broad distribution of anisotropy values in our earlier papers indicated that a broad distribution of single polymer chain morphologies was present in the ensemble of polymer chains.[47]

We have previously developed a molecular level understanding of single polymer chain morphology by comparing the histogram of the observed experimental anisotropy for the different chains in the ensemble to the predictions of the anisotropy from Monte Carlo simulations for stiff conjugated polymer chain employing a coarse grain beads on a chain model.[47] Within this model each bead represents one or at most a small number of repeat units and the stiffness and self-attraction of the chain are reflected respectively by the parameters b and U as described later in more details (eq. 2.28-30). For physically realistic stiffness and self-attraction parameters (b = 10 kT rad^{-2} and U = 0.6), this type of simulation predicts, for polymer chain with no structural defects, two types of condensed morphologies, the toroid and the rod. Figure 2.1 shows examples of the toroid and the rod forms. These simulations also show that a tetrahedral chemical defect due to non-ideality in the synthetic procedure and post synthetic chemical oxidation allows the chains to adopt complex disordered conformations (*e.g.* the defect-cylinder in Figure 2.1) with individual chain anisotropies ranging from zero to unity depending upon the location and the number of defects.[47,76,77]

In this chapter we reexamine the polarization anisotropy of MEH-PPV using significantly improved materials that contain relatively few tetrahedral defects per chain. We also employ an improved experimental apparatus that has less polarization distortion than the instrument that was employed by Hu *et al.*.[47] Detailed analysis of the new experimental results shows that the polymer chain conformation of nearly defect-free

MEH-PPV is surprisingly ordered and elongated in a rod structure. This has a number of implications for understanding the nanoscale morphology of conjugated polymer chains. Furthermore, the comparison of the experimental results to coarse grain beads on a chain simulations reported herein demonstrates that the intramolecular potentials for beads on a chain simulations typically used in polymer simulations may lack certain features that are necessary to realistically model the morphology of conjugated polymers.

2.2 MATERIALS AND METHODS

2.2.1 Materials

Poly[2-methoxy-5-(2'-ethylhexyloxy)1,4-phenylenevinylene)] (MEH-PPV) was purchased from Polymer Source Inc. (M_n = 150 kDa, PDI = 3.0 and M_n = 2,600 kDa, PDI = 1.5)[78] and American Dye Source Inc. (M_n = 1,000 kDa, PDI = 7.2)[79]. Poly[methylmethacrylate] (PMMA, M_n = 45 kDa) was purchased from Sigma Aldrich Co. Glass coverslips were cleaned in an acid piranha solution (hydrogen peroxide/sulfuric acid 1:3 in volume). [***Caution***: Piranha solution is aggressive and explosive. Never mix piranha waste with solvents. Check the safety precautions before using it.] Isolated chains of MEH-PPV embedded in PMMA matrix were obtained by dynamically spin-coating from toluene. The final thickness of these films was measured as 200 nm. In order to avoid any photooxidation of samples, they were prepared and sealed using epoxy resin (GC electronics, 2 Part Epoxy Glue) and a glass coverslip in a glove box (MBraun, with O_2 and H_2O less than 5 ppm) and investigated in the microscope apparatus within a few days after the sample preparation in order to avoid penetration of oxygen or moisture into the sample through leaks in the seal.

2.2.2 Wide-Field Fluorescence Polarization Spectroscopy Apparatus

A newly constructed wide-field fluorescence polarization spectroscopy apparatus with a 488-nm excitation wavelength was used to study MEH-PPV at its peak absorption in solution. In comparison to the previously described confocal type apparatus,[47] the new set-up has less distortion of excitation polarization. As derived by Axelrod[80] and Forkey *et al.*,[81] when the excitation beam is focused with high NA objective lens the polarization of the beam becomes distorted. Using wide-field excitation minimizes this problem because the excitation beam is close to collimated.

The apparatus is based on an inverted microscope (Zeiss, Axiovert 200) with a 1.25 NA objective lens (Zeiss, Achrostigmat, 100X) and a wide-field detection scheme using a EMCCD detector (Andor, model iXon$^+$ DU-897E). The excitation source is the 488-nm line of an Ar-Kr ion laser (Melles Griot, model 35 LAL-030-208). The polarization of the excitation beam was rotated in the x,y frame around the axis of propagation using an electro-optical modulator (EOM, Fastpulse technology, model 3079-4), a voltage amplifier (Trek, model 601-1) and a programmable function generator (Wavetek, model 29A) using a method previously described.[82] The polarization ratio was greater than 20:1 for any angle of rotation. The illumination area was ~40 μm at FWHM. The excitation power was estimated to be 1 W cm^{-2}. The excitation scattering light from the sample was blocked from the detector path using a dichroic mirror and a 488-nm notch filter (Chroma).

Fluorescence intensities of spots due to individual molecules were measured as a function of polarization angle, θ, and were synchronously time averaged over multiple cycles of polarization modulation to increase the signal-to-noise ratio. The intensities of individual spots were calculated by a simple integration procedure over 5×5 pixels and background subtraction using the background intensity obtained locally in the rectangular

region surrounding each spot. Approximately 20 individual molecules per image were monitored in the 50×50 μm of the field of view of the EMCCD.

2.2.3 Fitting Procedure to Extract Single Molecule Anisotropy (*A*) histogram from Polarization Modulation (*M*) Histogram

The modulation depth, *M*, was measured for an ensemble of single polymer chains using the method described above and by fitting the intensity *vs* polarization angle, θ, data to the following equation (2-3).

$$I(\theta) \propto 1 + M\cos 2(\theta - \phi) \tag{2-3}$$

where ϕ is the orientation when the emission intensity is maximized.

We have previously shown that *M* is due to a projection of the excitation (absorption) tensor onto the x-y plane of the sample. The absorption tensor is due to the incoherent addition of the absorption of individual chromophores located along the polymer chain. The total reduced and simplified tensor has three orthogonal components $I_{x'}$, $I_{y'}$, and $I_{z'}$. The polarization anisotropy in this case reflects the differences among these components. In the cylindrical tensor approximation[74] the polarization anisotropy is quantified by single parameter, *A*, where *A* is given by equation (2-4).

$$A = \frac{I_{z'} - \left(\frac{I_{x'} + I_{y'}}{2}\right)}{I_{z'} + \left(\frac{I_{x'} + I_{y'}}{2}\right)} \tag{2-4}$$

where z' is the direction of maximum bond orientation in the molecular frame.

The results of this chapter demonstrate as described in details below that nearly all of the observed MEH-PPV polymer chains possess an extended rod-shaped conformation resulting in high *A* value ($I_{z'} >> I_{x'}, I_{y'}$). Because *M* is a projection of the absorption tensor, the value of *M* depends explicitly on the tilt angle, ζ, of z' relative to the x-y plane of the microscope. Qualitatively, the major impact of a distribution of tilt

angles is to create a distribution of *M* values for any given *A* value. Even a conjugated polymer chain with a very high *A* value will yield a low *M* value if the chain is oriented perpendicular to the x-y plane of the sample. The precise description of the impact of the distribution of polymer chain orientations (ζ values) on the observed *M* values is presented in the following.

The single molecule polarization anisotropy, *A*, histograms were calculated by a best-fit procedure of the observed modulation depth values, *M*, using a program which convolutes the molecular orientation with anisotropy distribution. As *M* is a projection of molecular anisotropy onto the x, y plane, *M* values can be lower than *A* depending on the tilt angle of each molecule (Figure 2.2). Polarization distortion due to the high NA objective lens was also included in the program. The program generates an arbitrary *A* distribution and converts it to an *M* histogram. Then a fitting routine finds the best *A* distribution to reproduce the experimental result. The calculation employed Forkey's *et al.* equations for the fluorescence intensity of a single dipole as a function of orientation angle in a laboratory frame.[81] In order to calculate the modulation depth, *M*, of a multi-chromophoric system, the expressions were modified as described in the following text. MEH-PPV was assumed to be well-modeled by multiple local chromophores along the polymer chain. An absorption spheroid, representing a continuous distribution of chromophores, was used to describe the absorption rate of a single MEH-PPV chain as a function of chain orientation in the laboratory frame. A dipole moment absorption vector at the angle (θ', ϕ') in a molecular frame was described as follows.

$$\mu_x(\theta', \phi') = a\cos\phi'\cos\theta' \tag{2-5}$$

$$\mu_y(\theta', \phi') = a\cos\phi'\sin\theta' \tag{2-6}$$

$$\mu_z(\theta', \phi') = c\sin\phi' \tag{2-7}$$

where *a* is the minor axis, *c* is the major axis, θ' is the azimuthal angle and ϕ' is the

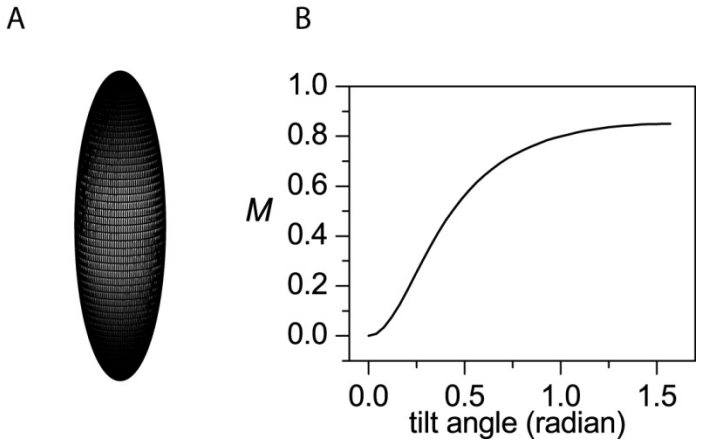

Figure 2.2: (A) A spheroid with anisotropy of 0.85. (B) Calculated modulation depth in the x, y plane of the lab frame as a function of the tilt angle. A long axis of the spheroid is in the z-axis when the tilt angle is 0.

elevation angle. When the spheroid is tilted at angle ξ from the z-axis around the x-axis of a laboratory frame, the following vector is derived.

$$\mu_x(\theta',\phi') = a\cos\phi'\cos\theta' \tag{2-8}$$

$$\mu_y(\theta',\phi') = a\cos\phi'\sin\theta'\cos\zeta - c\sin\phi'\sin\zeta \tag{2-9}$$

$$\mu_z(\theta',\phi') = a\cos\phi'\sin\theta'\sin\zeta + c\sin\phi'\cos\zeta \tag{2-10}$$

The observed fluorescence intensity at a detector can be described as follows. Here, a spheroid is tilted at angle ζ only around the x-axis, so I_x and I_y are the minimum and maximum values, respectively.

$$I_x = C_{ex1}(C_{em1}+C_{em2})\mu_{ex}^2 + C_{ex2}(C_{em1}+C_{em2})\mu_{ey}^2 + C_{ex3}C_{em3}\mu_{ez}^2 \tag{2-11}$$

$$I_y = C_{ex2}(C_{em1}+C_{em2})\mu_{ex}^2 + C_{ex1}(C_{em1}+C_{em2})\mu_{ey}^2 + C_{ex3}C_{em3}\mu_{ez}^2 \tag{2-12}$$

μ_{ex}^2, μ_{ey}^2, μ_{ez}^2 are the x, y, z component of the absorption dipole integrated over the surface of the spheroid, and C_{ex1}, C_{ex2} and C_{ex3} are the coefficients which take the numerical aperture of the objective lens into account for the excitation and C_{em1}, C_{em2} and C_{em3} for the emission.

$$\mu_{ex}^2 = \int_{-\pi}^{\pi}\int_{-\pi/2}^{\pi/2} d\phi'\,d\theta'\cos\phi'\{a\cos\phi'\cos\theta'\}^2 \tag{2-13}$$

$$\mu_{ey}^2 = \int_{-\pi}^{\pi}\int_{-\pi/2}^{\pi/2} d\phi'\,d\theta'\cos\phi'\{a\cos\phi'\sin\theta'\cos t - c\sin\phi'\sin t\}^2 \tag{2-14}$$

$$\mu_{ez}^2 = \int_{-\pi}^{\pi}\int_{-\pi/2}^{\pi/2} d\phi'\,d\theta'\cos\phi'\{a\cos\phi'\sin\theta'\sin t + c\sin\phi'\cos t\}^2 \tag{2-15}$$

$$C_1 = \frac{1}{8}\left(5-3\cos\delta-\cos^2\delta-\cos^3\delta\right)\left(1-\cos\delta\right)^{-1} \tag{2-16}$$

$$C_2 = \frac{1}{24}\left(1-3\cos\delta+3\cos^2\delta-\cos^3\delta\right)\left(1-\cos\delta\right)^{-1} \tag{2-17}$$

$$C_3 = \frac{1}{6}\left(2-3\cos\delta+\cos^3\delta\right)\left(1-\cos\delta\right)^{-1} \tag{2-18}$$

$$\delta = \sin^{-1}\frac{NA}{n} \tag{2-19}$$

where *NA* is the numerical aperture of the objective lens and *n* is the refractive index of the media. From I_x and I_y, the modulation depth *M* for a single molecule with an angle ζ was calculated as follows.

$$M = \frac{I_y - I_x}{I_y + I_x} \tag{2-20}$$

A log-normal distribution was used for the *A* histogram[83] and a least square procedure was used to fit the calculated histogram to the experimental data.

2.3 RESULTS AND DISCUSSION

2.3.1 Polarization Modulation Depth (*M*) Histograms

The experimentally observed *M* values (Figure 2.3A) for an ensemble of MEH-PPV isolated molecules of a molecular weight of 150 kDa are distributed from unity all the way down to zero. An analysis of these results employing a distribution of tilt values and a model presented above reveal that the experimentally observed results are well fitted (Figure 2.3B) by an empirical log-normal distribution[83] of *A* values (Figure 2.3C) as follows.

$$P(A) = \frac{a_2}{A - a_1} \exp(-a_3{}^2) \exp\left\{ -\frac{1}{2a_3{}^2} \left[\ln\left(\frac{A - a_1}{a_2} \right) \right]^2 \right\} \tag{2-21}$$

$$P(A) = 0; \quad \frac{A - a_1}{a_2} \le 0 \tag{2-22}$$

where *A* is the anisotropy, the parameters a_1, a_2, and a_3 are related to the peak (A_0), the FWHM (*H*) and the asymmetry (ρ) of the distribution of the *A* values by the expressions:

$$a_1 = A_0 - H\left(\frac{\rho}{\rho^2 - 1} \right) \tag{2-23}$$

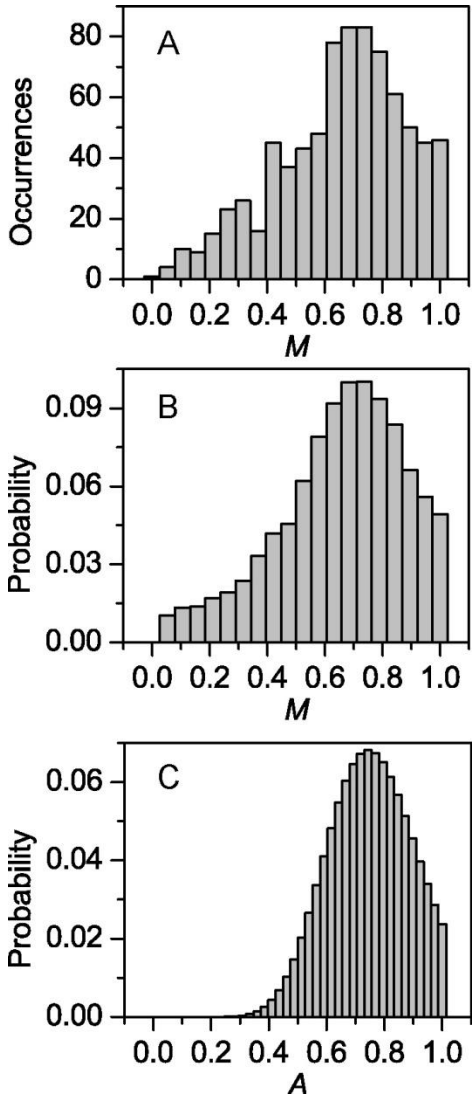

Figure 2.3: (A) The experimental histogram of modulation depth, *M*, from 798 single MEH-PPV molecules (number average molecular weight 150 kDa). (B) The best fit histogram for the data shown in (A), calculated by a least-square fitting procedure. (C) Anisotropy, *A*, distribution resolved by the best fit which generated the data shown in (B).

$$a_2 = H\left(\frac{\rho}{\rho^2 - 1}\right)\exp(a_3{}^2) \tag{2-24}$$

$$a_3 = \frac{\ln(\rho)}{\sqrt{(2\ln 2)}} \tag{2-25}$$

Interestingly, the best fit log-normal distribution does not contain a significant number of low A values in the distribution. In fact we have been unable to fit the results with any distribution which has a few percent of molecules of A value less than 0.3. Thus we can conclude that exclusively high anisotropy molecules are present in the experimental results.

There are two other features of the A fitting process that should be emphasized. First, in addition to the tilt angle effect that was described above, polarization distortion due to the non-collimation of the excitation and the collection optics must be also included in the simulation process. A detailed description of how we include polarization distortion in the computer program used to calculate Figure 2.3B is presented in the section 2.2. Second, an important component of the data acquisition and the analysis process that must be carefully considered in order to obtain unbiased A results is the θ average intensity threshold, $I_{\bar{\theta}}$, for selecting fluorescence spots that is required to select the ensemble of molecules used in the analysis. In particular, it is important to choose a threshold that is large enough to reject spurious spots that are due to impurities; however, if the threshold is set too high, model calculations show that the best-fit A distribution becomes artificially biased toward higher A values. We have carefully verified that the best fit A distribution presented herein is not in error due to the threshold distortion effect by studying the best-fit A results as a function of chosen threshold over a large range.

Figure 2.4 shows analogues M and A distributions for ensemble conjugated polymer chains with a larger molecular weight of 2,600 kDa. As in the case of the lower

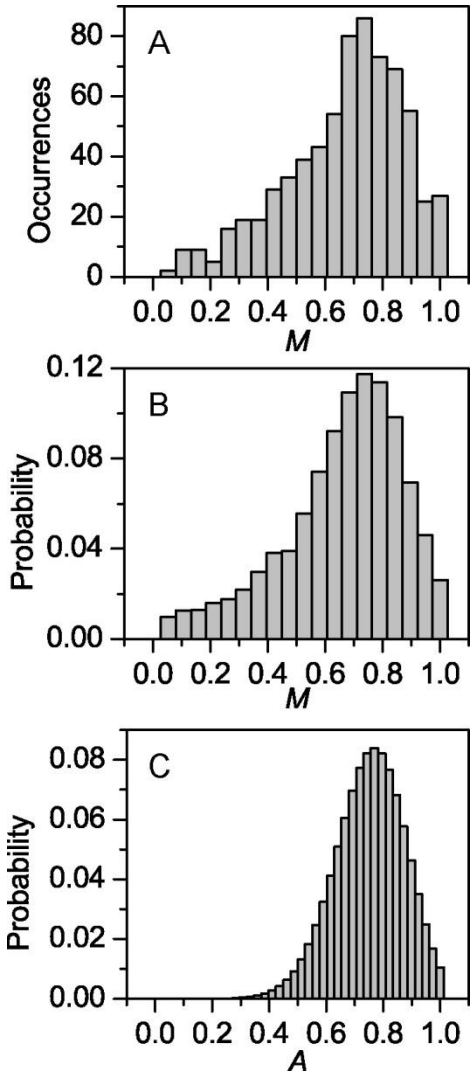

Figure 2.4: (A) The experimental histogram of modulation depth, *M*, from 692 single MEH-PPV molecules (number average molecular weight 2,600 kDa). (B) The best fit histogram for the data shown in (A), calculated by a least-square fitting procedure. (C) Anisotropy, *A*, distribution resolved by the best fit which generated the data shown in (B).

molecular weight sample that was described above, the majority of molecules in this ensemble has an extremely high anisotropy indicative of an ordered rod-shaped conformation. Further polarization *M* measurements associated with the best fit parameters of the *A* distribution are summarized in the Table 2.1. The final entry in the Table 2.1 corresponds to a greater than three years old sample of MEH-PPV obtained from American Dye Source Inc. This sample reveals a considerably broader *M* histogram and a corresponding lower mean *M*, and broader distribution of *A* values. It is highly likely that the broad distribution of molecular conformational order implied by this result is a consequence of unintentional tetrahedral defects (in place of double bonds) which has previously been demonstrated to disturb the order.[47,76] A further indication that this MEH-PPV sample has multiple chemical defects in the polymer chain is the large shift in the absorption maximum from the expected value for the pure polymer of 500 nm to a value of 487 nm, demonstrating a "broken conjugation" effect.[76] Other than the shift in the absorption maxima, the absorption and emission spectra for the more or less defective polymers are indistinguishable. Coarse grain beads on a chain simulations described below, related with previously published data,[47,76] demonstrate that the tetrahedral defects induce conformational disorder and heterogeneity leading to a large range of anisotropy values.

It is interesting to compare the *M* histograms here to those reported in our previous publications.[47,76] The present results are characterized by a significantly high mean *M* values, a much narrower *M* distribution, and especially significant reduction of the fraction of lower *M* values in the polymer chains. We ascribe the contrasting behavior of the new and previously reported histograms to two sources. First, the newer polymer samples from Polymer Source Inc. have substantially small number of tetrahedral defects along the polymer chain as reflected in the absorption spectra. Second, the present

Materials	M_n (kDa)	PDI	λ_{abs} (nm)[1]	Modulation depth		The best fit parameters		
				Mean	Std	A_0	H	ρ
MEH-PPV	150	3.0	500	0.66	0.22	0.75	0.40	1.2
MEH-PPV	2,600	1.5	500	0.67	0.21	0.77	0.30	0.89
MEH-PPV defected	1,000	7.2	487	0.61	0.26	0.71	0.98	2.0

Table 2.1: Modulation Depth and the Best Fit Parameters by Log-normal Function for Various Molecular Weight and/or Suppliers of MEH-PPV.

[1] Absorption measured in Toluene.

measurements were made with our new wide-field polarization modulation apparatus, while the earlier measurements were made with a confocal based single molecule polarization apparatus, as described above. Due to the better collimation of the excitation beam in the wide-field apparatus, the measured *M* values are significantly less distorted by optical effects in the excitation optics.

A small fraction of the molecules exhibited a photobleaching within the 200 s period for a complete modulation experiment. These molecules were removed from the analysis process. After removal of molecules exhibiting photobleaching the resulting histograms were highly reproducible from sample to sample and were also reproduced with a second version of apparatus similarly designed but with new optical components. It was verified that only a smaller number (less than 5 % and in some case lower) of spots were observed due to impurities from samples prepared by an identical procedure in which MEH-PPV was not included in the spin coated solution. Similar *M* histograms to those in Figures 2.3 and 2.4 were observed with thinner PMMA films, although significantly thinner samples revealed a greater fraction of molecules that exhibited a blinking due presumably to interactions of MEH-PPV chains with the surface of the glass substrate underlying the PMMA film. The *M* histograms are not significantly dependant on the concentration of MEH-PPV/PMMA by two orders of magnitude, however at significantly higher MEH-PPV concentration it becomes difficult to measure fluorescence intensities due to overlapping of fluorescence spots, which tends to lead to errors in the *M* measurements. Finally, while in our previous measurements a metal layer was directly deposited on top of the MEH-PPV/PMMA film in order to seal the sample, in the present study we employ a several millimeter gap filled with N_2 as means of avoiding O_2 contamination. This latter approach has the advantage that it does not lead to

metal induced fluorescence quenching of MEH-PPV molecules located at the top interface of the PMMA thin film.

2.3.2 Comparison of Experimental *A* Histograms to Predictions from Beads on a Chain Simulations

Building on our previous modeling studies of the conformation of conjugated polymer chains,[47] we have used a coarse grain beads on a chain model to describe MEH-PPV isolated molecules. To simulate the folding of a semiflexible chain from an elongated, disordered coil state at high temperature to the collapsed, low temperature state, we used a Langevin dynamics simulation for a coarse-grained chain. The motion of an individual bead in the beads on a chain model is governed by the Langevin equation[84]

$$\ddot{\boldsymbol{r}}_i = \Gamma \dot{\boldsymbol{r}}_i - \nabla U - \boldsymbol{W}_i(t) \tag{2-26}$$

where subscript i=1,..,N represents the bead index, N being the total number of beads. The left-hand side is the inertial term and the right-hand side consists of the dissipative frictional force $(\Gamma \dot{\boldsymbol{r}}_i)$, the conservative interaction force (∇U) and the random noise force $(\boldsymbol{W}_i(t))$ which captures the dynamical effects of the implicit solvent molecules. The equation above is written in reduced units where the distance is scaled with r_0, the equilibrium segment length, the time is scaled with $\sqrt{mr_0^2 / k_B T}$ and the energy is described in the units of $k_B T$. In these units, the dimensionless friction coefficient Γ is chosen to be unity[84]. The random noise has following properties:

$$\begin{aligned} \langle \boldsymbol{W}_i(t) \rangle &= 0 \\ \langle \boldsymbol{W}_i(t) \cdot \boldsymbol{W}_j(t') \rangle &= 6\Gamma \delta_{ij} \delta(t - t') \end{aligned} \tag{2-27}$$

Starting with random initial chain conformations, Eq. (2-27) is integrated in time using the velocity Verlet finite difference scheme.[85] The time step in our simulations was kept as 0.01. Even though the simulated chains are allowed to evolve over a very long time, it might be possible that the chains at equilibrium may be trapped in a non-

stationary state separated from the global minimum by an energy barrier. However, the histograms, generated for an ensemble of around 400 chains, are believed to capture the representative probability distribution of multiple crystalline states.

The potential energy of the chain U consists of the energy associated with the stretching of the segment length, U_r, the energy cost for bending of the chain, U_b, and the bead-bead interaction energy, U_{LJ}, given by:

$$U_r = k(r-1)^2 \tag{2-28}$$

$$U_b = b\Theta^2 \tag{2-29}$$

$$U_{LJ}(r_{ij}) = \begin{cases} 4\varepsilon\left[\left(\frac{\sigma}{r_{ij}}\right)^{12} - \left(\frac{\sigma}{r_{ij}}\right)^{6}\right] & r_{ij} \le 2\sigma \\ 0 & r_{ij} > 2\sigma \end{cases} \tag{2-30}$$

where Θ is the bending angle between two neighboring segments. The value for the coefficient of stretching energy k is kept at 100 (in the reduced units), for which case the segment length in our simulations is found to remain at its equilibrium value of unity. In the present study, the stiffness parameter b is kept in the range 10-100 kT rad^{-2}. The Lennard-Jones interaction parameters are taken from a previous study on conjugated polymers[47] which uses ε = 0.6 and $\sigma = 2.1$ (in reduced units). Typically one coarse-grained bead represents 2.5 repeat units of MEH–PPV chain.[47] In order to calculate an ensemble of polymer chain conformations, we have carried out the Langevin dynamics simulations described above. The simulations were carried out for $3\times10^5 - 5\times10^5$ time steps to equilibrate the system. Equilibration was monitored through the temporal evolution of chain properties such as the internal energy and the orientation order parameter. The anisotropy, A, defined in the previous section, is calculated from the eigenvalues of the orientation tensor $\langle \boldsymbol{uu} \rangle$, where $\boldsymbol{u}$ is the bond vector and $\langle\ \rangle$ indicates averaging over the chain length. A value is defined as

$$A = \frac{\lambda_1 - \frac{1}{2}(\lambda_2 + \lambda_3)}{\lambda_1 + \frac{1}{2}(\lambda_2 + \lambda_3)} \tag{2-31}$$

where λ_1 is the maximum eigenvalue, and λ_2 and λ_3 are the remaining two eigenvalues of matrix $\langle \boldsymbol{uu} \rangle$. A value calculated at a given time is then averaged over 10^5 time steps after equilibration to give A_{avg}. The average anisotropy A_{avg} is obtained for an ensemble of around 400 chains and the probability distribution of A_{avg} is presented in terms of a histogram.

For a chain with N = 101 (representing approximately 250 repeat units, *i.e.* ~ 75 kDa, of a MEH-PPV molecule) and no tetrahedral defects, Figure 2.5A shows the distribution of predicted A values and associated beads on a chain representation of two highly ordered conformations from the simulations. Compared to the experimental results, the simulated histograms failed to show a large number of conformations with anisotropies above a value of 0.75. Note that the conformations that are predicted in these simulations are cylindrical in shape with multiple folds of the chain. In order to explore the sensitivity of the simulations of chain to the chosen values for the parameters employed in the model, we have investigated the dependence on both the stiffness and the number of beads employed in the simulations.

Increasing the assumed stiffness of the chain produces a sub-ensemble of chains with a highly anisotropic rod-shaped conformation containing a small number (*i.e* two or even one) fold of the chain. However, these simulations also show the previously identified toroid conformation which has significantly lower anisotropy (A ~ 0.4). In detail, the stiffness parameter b = 10 kT rad^{-2} (Figure 2.5A) is the value previously estimated as the most appropriate value for MEH-PPV based on the analysis of the vibrational spectroscopy.[86] The value b = 10 kT rad^{-2} represents a chain whose

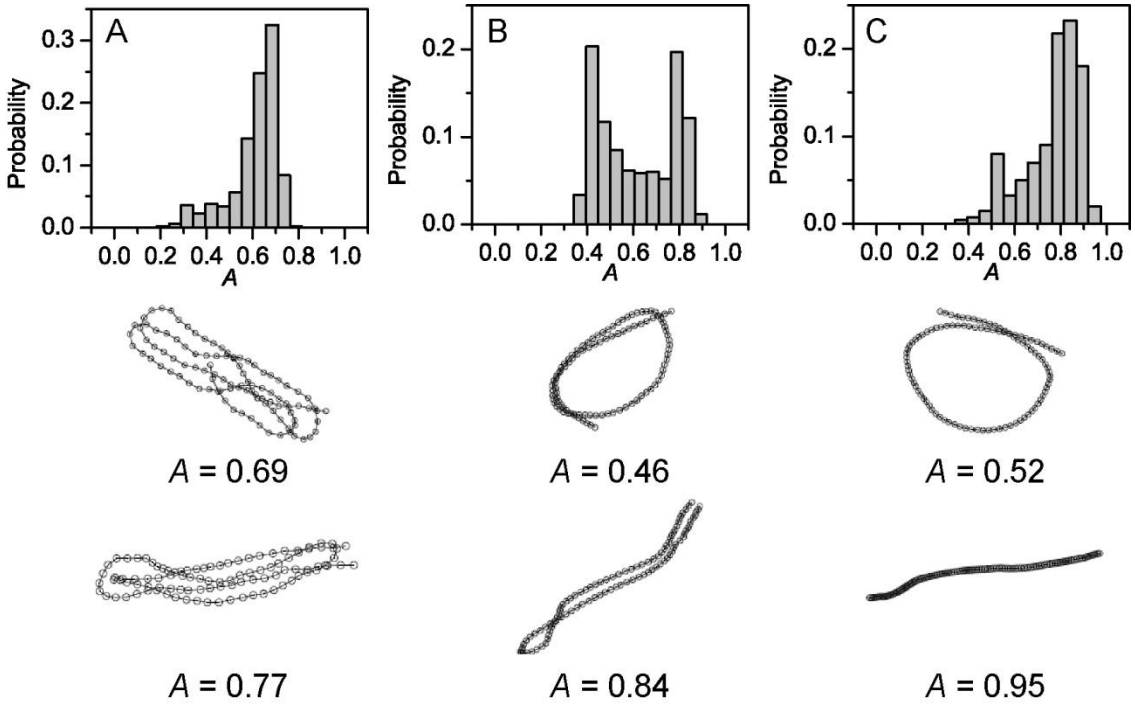

Figure 2.5: The simulated anisotropy, A, distributions for 400 chains with 100 beads and no defect,for three different stiffness parameters of the polymer chain: (A) b = 20 kT rad-2, (B) b = 50 kT rad-2, (C) b = 100 kT rad-2. The most probable chain conformations are also shown.

persistence length is 20 segments.[87] For b = 10 kT rad^{-2}, the distribution peaks at around 0.7 for which the corresponding collapsed state is a folded conformation resembling an ordered cylinder. For b = 50 kT rad^{-2}, as shown in the Figure 2.5B, single-folded hairpin structures with $A > 0.8$ are observed as stable structures. However for this case, toroids with $A \sim 0.4$ are found to coexist with highly ordered hairpins at equal probabilities. Further increase in the chain stiffness renders the toroids less probable and for b = 100 kT rad^{-2}, for which case the persistence length is half the chain contour length, rods with $A >$ 0.75 are realized with very high probability (see Figure 2.5C). However, this stiffness parameter is much higher than that predicted by considering the vibrational force field of MEH-PPV[86] and as such is probably unrealistic.

We have also undertaken more time consuming simulations on longer chains, 200 beads (*i.e.* ~ 150 kDa MEH-PPV), in order to predict the anisotropy of chains closer in size to those investigated experimentally (Figure 2.6). The results are analogous to those described above for the 100 beads. However, the histograms of longer chains exhibit a slightly lower mean A value and a slightly broader A distribution.

Generally speaking, the predicted A histograms reveal both lower and broader distribution than it is observed experimentally. In particular a key discrepancy between experimental and theoretical results is the presence of toroids. While we previously emphasized the potential importance of toroidal conformation for collapsed, isolated conjugated polymer chains,[47] the present experimental results seem to rule this out. A key question then arises why toroidal conformations are missing for real conjugated polymer chain? One possible answer to this question may be that there is or are key missing features in the model potential we and others have used to model conjugated polymer chains. For example it is conceivable that there are additional non-identified modes of polymer chains that favor sharp-bending rod conformations over toroidal

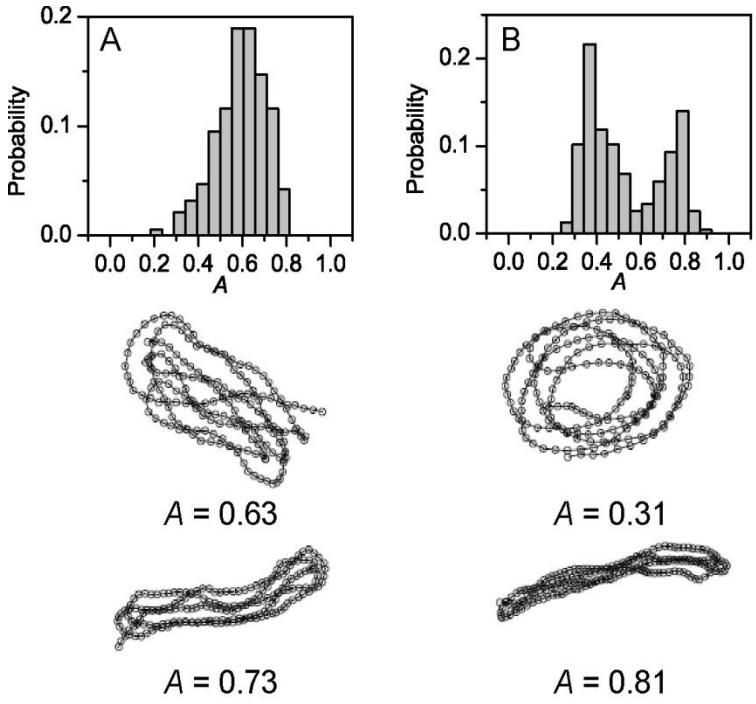

Figure 2.6: The simulated anisotropy, A, distributions for 400 chains with 200 beads and no defect, for two different stiffness parameters of the polymer chain: (A) b = 10 kT rad^{-2}, (B) b = 20 kT rad^{-2}. The most probable chain conformations are also shown.

conformations.[77] To explore that further, we consider the effect of bending defects at various points along the polymer chain. The defect was introduced by setting the angle between two neighboring segments at 109^{o} (*i.e.* tetrahedral defect) at the location of the defect instead of usual 180^{o} at other locations. Figure 2.7A shows the resulting anisotropy histograms for the case when one defect is introduced in the middle of the chain (representing a thermally excited defect which can choose the preferred location). In this case, highly ordered folded structures with $A \sim 0.8$ are found to be favored at equilibrium. If the defect is located in the center of the chain, the toroidal conformations with $A \sim 0.4$ are greatly eliminated and the hairpin-like morphology with central folding becomes a highly probable state. Thus the notion of some presently unknown thermal induced sharp-bending defects[45,77] may be responsible for the experimentally observed high A values, which is promising and should be studied further. Another potential reason for the absence of toroidal conformations is the influence of the PMMA host, which is not taken into account in the simulations.

It should be emphasized that thermally induced sharp-bending defects have a completely different effect on the predicted A histograms from the one due to chemically randomly introduced tetrahedral defects, which are present in real materials as a result of chemical oxidation. Simulated results with randomly situated tetrahedral chemical defects produce ensemble of chains that exhibit a much broader A distribution than it is observed in experiments (see Figure 2.7B). While some of the defected chains accidentally have defects located at the regions which increase the A values, the ensemble also included chains which have defects located in places that significantly reduces A values. In fact, as mentioned above, when the number of chemical defects are increased to be a significant fraction of all segments, the chains are predicted to have a low mean A value and a very broad A histogram.

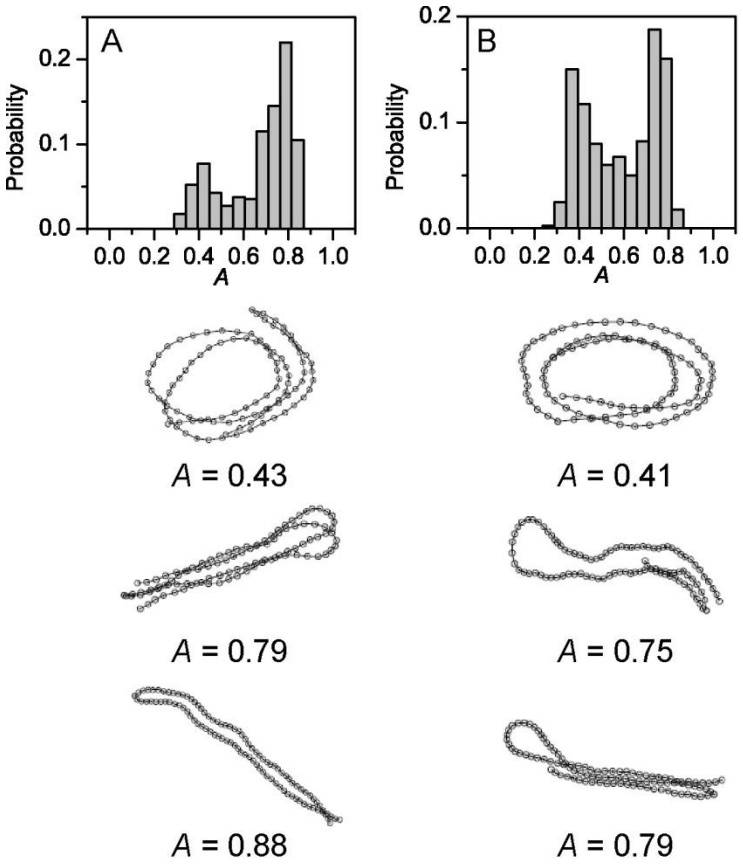

Figure 2.7: The simulated anisotropy, A, distributions for 400 chains with 100 beads and the stiffness parameter $b = 20\ \mathrm{kT\ rad^{-2}}$ with one defect. (A) One defect placed in the middle of the chain and (B) one defect randomly placed in the chains (B). The most probable chain conformations are also shown.

2.4 CONCLUSION

We have reexamined the fluorescence polarization anisotropy of single conjugated polymer MEH-PPV chains. These experiments employed a more precise single molecule fluorescence excitation polarization spectroscopy apparatus and improved MEH-PPV materials that contain significantly less chemical defects. Two different molecular weight samples were measured: 150 kDa and 2,600 kDa. The new polarization anisotropy data after the analysis for the optical polarization effects in the microscope revealed an extraordinary narrow distribution of the anisotropy values centered ~ 0.75 for the different polymer chains in the ensemble. This indicates that the single polymer chain morphology of MEH-PPV has a large degree of parallel chain (nematic-like) order that is considerably more than previously believed based on the earlier measurements. When analyzed by comparing the observed anisotropy data to simulation results from a coarse grain beads on a chain model and molecular dynamics simulations, the predominant morphology of the polymer chain is found to be in a highly anisotropic, rod morphology comprised of only a few turns of the polymer chain. Interestingly, the previously reported toroidal conformation is not observed in these experiments due apparently to the ability of single polymer chain to thermally induce bending defects at the optimal location to achieve more highly anisotropic rod conformation.

Acknowledgement for co-author contributions:
I would like to thank Dr. Johanna Brazard and Dr. Joshua Bolinger for helping me performing the experiments, Dr. Paresh Chokshi and Prof. Venkat Ganesan for performing the molecular dynamics simulations, and Prof. Paul F. Barbara for designing the experiments and helping me writing the analysis programs.

Chapter 3: Watching the Annealing Process One Polymer Chain at a Time

This chapter was reproduced in part from: Vogelsang, J.; Brazard, J.; Adachi, T.; Bolinger, J. C.; Barbara, P. F. *Angew. Chem. Int. Ed.* **2011**, *50*, 1 – 6.

3.1 INTRODUCTION

Annealing (i.e. equilibrating) of conjugated polymer and polymer blend films is a widely used process that achieves optimal film morphology and therefore improves material properties such as electrical mobility for photovoltaic devices and other applications.[88-94] Especially, solvent vapor annealing (SVA) is an industrially important technique since it causes a rapid morphological equilibration of films at room temperature without thermal damage of the material or other complications which are disadvantages of high-temperature annealing.[95-97] However, due to the complexity of polymer films, the understanding of SVA at the molecular level remains largely unclear. In particular, the polymer chain conformation (i.e. morphology) of the intermediates along the annealing pathway, the dynamics of chain reassembly during annealing, and spatial and temporal inhomogeneities of the annealing process have not yet been determined. A better understanding of SVA at the molecular level could lead to improved processing methods of conjugated polymer films, and even to the first rational design approaches for this material class. Single molecule fluorescence spectroscopy/ microscopy (SMS) techniques are a promising approach to obtain a molecular picture of SVA and have already proven to be a valuable experimental tool to study conjugated polymer chain conformations.[40-42,47,98-100]

In this chapter, we report the real-time observation of morphological dynamics induced by SVA in a model system comprised of single chains of a prototypical conjugated polymer poly[2-methoxy-5-(2'-ethylhexyloxy)-1,4-phenylenevinylene]

(MEH-PPV; denoted here as single CP chains) embedded in a poly(methyl methacrylate) (PMMA) host matrix. SMS techniques using a home-built gas/solvent vapor flow chamber (see Experimental Section for details) enabled us to monitor the SVA-induced translocations of single chains (Figure 3.2), to observe the dynamics of chains folding and unfolding (Figure 3.3), and to compare morphological order in single chains immediately after spin-coating of a film to ones after SVA (Figure 3.6).

3.2 EXPERIMENTAL SECTION

Poly[2-methoxy-5-(2'-ethylhexyloxy)1,4-phenylenevinylene] (MEH-PPV) was purchased from Polymer Source Inc. and further purified by GPC with a polystyrene standard to obtain Mn=830 kDa with a PDI of 3.5. Poly(methyl methacrylate) (PMMA, Mn=45 kDa, PDI= 2.2) was purchased from Sigma Aldrich Co. Glass coverslips were cleaned in an acid piranha solution (hydrogen peroxide/sulfuric acid 1:3 in volume). Isolated chains of MEH-PPV embedded in a PMMA matrix were obtained by dynamically spin-coating from toluene or chloroform. The PMMA film thickness was 200 nm, and the concentration of MEH-PPV in solution before spin-coating was approximately 10^{-13} $molL^{-1}$, leading to a final spot density of about 0.1 spots/μm^2. To avoid any photo-oxidation of samples, they were prepared in a glove box (MBraun, with O_2 and H_2O less than 5 ppm) and investigated in the microscope apparatus (see chapter 2 for more details) equipped with a home-built gas flow cell to purge the sample with nitrogen gas, preventing exposure of the sample to oxygen or moisture. The removal of oxygen was examined by applying high-intensity pulses on single conjugated polymer chains, which leads to a significant triplet build-up if no oxygen is present[101] (see Figure 3.9 and Ref. [101] for details). For SVA the nitrogen gas was saturated with the respective solvent (toluene, chloroform, or hexane) by slowly purging the gas through a reservoir of the solvent. No change in the MEH-PPV/PMMA film thickness was observed before and

after the annealing (Figure 3.10). For the preparation of the bulk MEH-PPV film a concentrated MEH-PPV/THF solution (10^{-7}–10^{-8} molL^{-1}) was spin-cast at 2000 rpm onto a glass substrate. For fluorescence correlation spectroscopy (FCS) measurements, the same microscope was used, but in the confocal mode, where the collimated beam of the 488 nm line of an Ar^{+}-gas laser was extended to a diameter of about 1 cm and coupled into the objective. The fluorescence signal was collected by the same objective, focused on an avalanche photo diode (SPCM-AQR-16, Perkin-Elmer) for detection and the signal was correlated by an ALV-5000 fast hardware correlation card.

3.3 Results and Discussion

The main results are summarized in Figure 3.1. Ensemble spectroscopic measurements have shown that CP chains in the solvents used here are isolated, well solvated, and contain few, if any, intra-chain contacts.[52,102,103] In a spin-coated MEHPPV/PMMA film, SMS data show a heterogeneous distribution of collapsed CP chain conformations, including subpopulations of relatively disordered conformations that are kinetically trapped in a high energy state and ordered conformations with a low energy state. During SVA, the film resides in a heterogeneous mixture of solid and liquid-like phase in which the CP chains undergo folding/unfolding events between a collapsed and an extended conformation. The CP chains also undergo large translational jumps during SVA. When SVA is terminated, a solid MEH-PPV/PMMA film is produced in which the CP chains are exclusively in equilibrated highly ordered conformations.

Figure 3.2 shows typical fluorescence images before (Figure 3.2a), during (Figure 3.2b), and after (Figure 3.2c) SVA of a MEH-PPV/PMMA film. Stationary single CP chains can be observed in the long exposure images (ca. 180 s) in Figure 3.2a and c as

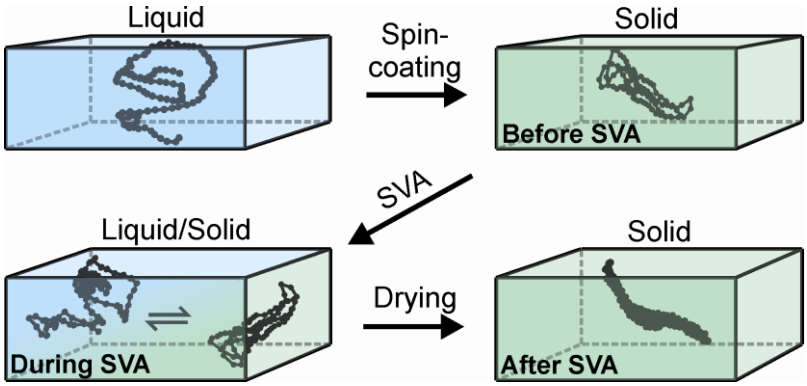

Figure 3.1: Schematic representation of the connection between the conjugated polymer chain conformation and the phase of the sample (SVA, solvent vapor annealing).

diffraction-limited fluorescence spots. In contrast, during SVA, the translational diffusion of CP chains is observed in Figure 3.2b as elongated and blurred fluorescence spots and an increase of fluorescence in the background. Swelling of PMMA by toluene vapor has been studied previously and it was reported that absorption of saturated toluene vapor effectively lowers the glass transition temperature, T_G, of high molecular weight PMMA from about from about 390 K to near or below ambient temperature.[104,105] The observed translational diffusion of single CP chains is clearly due to PMMA swelling. During SVA, the observed single CP chain position trajectories, such as the inset in Figure 3.2b, reveal large fluctuations in the apparent diffusion coefficient, which can, at our level, be sorted into three time regimes. These fluctuations range from: 1) stationary positions on the seconds time scale, 2) time resolvable translocations between 100 ms and 1 s, and 3) rapid "liquid"-like diffusion on the 1–100 ms timescale. The CP chains in the "liquid"-like domains move too fast to be observed directly in the wide-field microscope images but are clearly detectable by fluorescence correlation spectroscopy (FCS). The FCS curves in Figure 3.2 show that a large amplitude of intensity fluctuations is observed on the 10–100 ms timescale during SVA due to translation through the diffraction-limited FCS excitation/observation volume (Figure 3.2b), while no significant motion is observed before and after exposing the film to solvent vapor (Figure 3.2a,c). A high heterogeneity of diffusion times was also observed during the polymerization process of a polymer network and it was concluded that the different diffusion times are related to different degrees of network formation in space.[106] Since the formation and disintegration of a polymer network is related to swelling, a spatial heterogeneous swelling process can be assumed here during SVA.

Conformational changes that occur to the CP chains involving the unfolding and folding correlated with SVA were observed as fluorescence intensity fluctuations (Figure

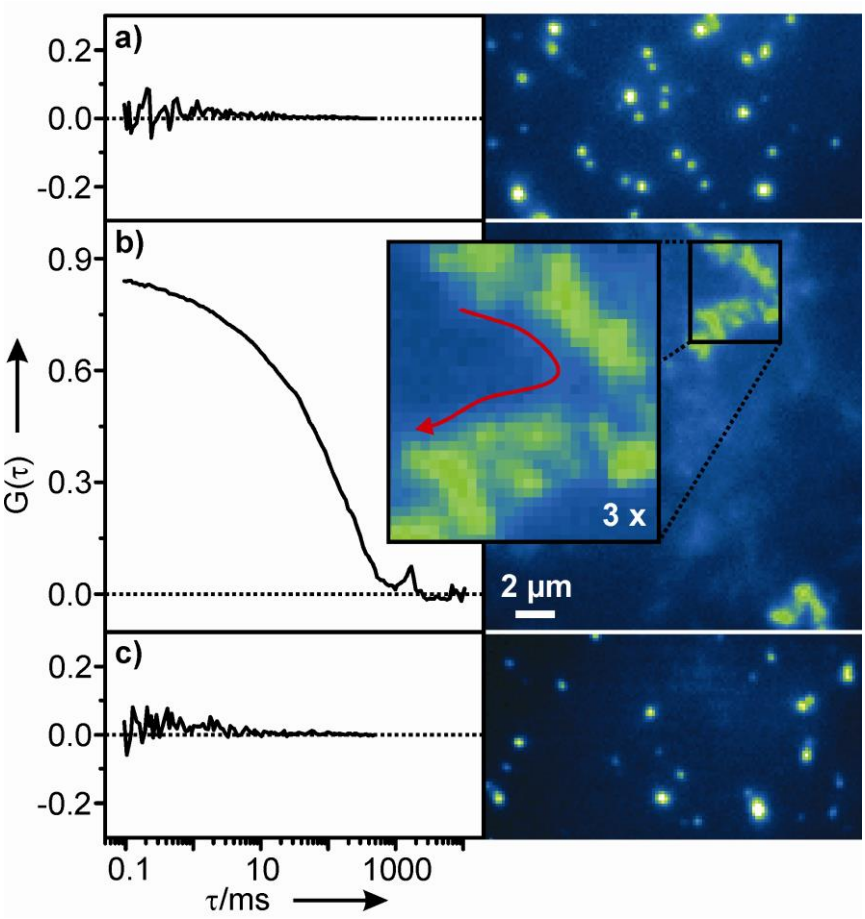

Figure 3.2: Fluorescence correlation spectroscopy (FCS) and wide-field fluorescence images of MEH-PPV/PMMA thin films under different processing conditions are presented. The FCS curves on the left are acquired from a PMMA film with an average concentration of MEH-PPV of ~ 1 molecule/µm² before (a), during (b) and after (c) SVA. The wide field fluorescence images on the right are shown of a PMMA film containing isolated MEH-PPV molecules before (a), during (b) and after SVA (c). The red arrow corresponds to the translation pathway of the molecule. The images are averaged over 180 images with an integration time of one second each. The excitation intensity was ~1 Wcm^{-2}.

3.3). The fluorescence transients of single CP chains were measured by wide-field fluorescence microscopy over a long time period (200–300 s) while the environment was switched between SVA and pure N_2 (no SVA) as indicated in Figure 3.3a. Due to the translation of single CP chains during SVA the fluorescence intensity transients were acquired by tracking the diffraction-limited fluorescence spots under both static and annealing conditions. Additionally, wide-field fluorescence images of a CP chain corresponding to the fluorescence transient at various times and different conditions are presented (Figure 3.3b). The fluorescence transients show that the intensity of single CP chains under SVA is two to three times higher compared to conditions with no solvent vapor present (no SVA). Since over the complete acquisition time the same single CP chain is observed and therefore no change in the absorption cross section can be assumed, this intensity increase is clearly due to an increase in the quantum yield of fluorescence, ϕ_{Fl}.

It has been known from ensemble spectroscopy measurements that the ϕ_{Fl} of MEH-PPV decreases by a factor of 2–3 from solutions compared to films.[63,107] The ϕ_{Fl} decrease is due to the conformational transition of CP chains from an extended conformation to a collapsed conformation.[102] Nguyen et al. reported the correlation between the hydrodynamic radius of MEH-PPV chains and their ϕ_{Fl} value by comparing the results of dynamic light scattering experiments and ϕ_{Fl} measurements in different solvents. The hydrodynamic radius decreases in the poor solvent tetrahydrofuran (THF) compared to the good solvent chlorobenzene. The ϕ_{Fl} of MEH-PPV is lower in the poor solvent compared to the good solvent, suggesting that ϕ_{Fl} is lower in a more collapsed conformation.[102] Therefore we conclude that the observation of the intensity change is due to the transition between a collapsed and an extended conformation, although the mechanism of self-quenching is still unclear. Additionally, the switching between these

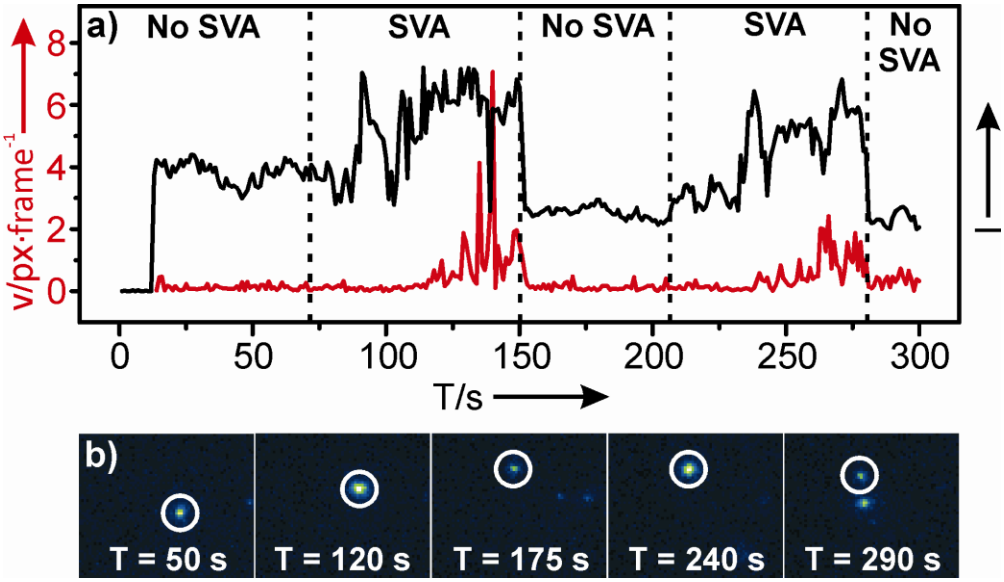

Figure 3.3: Fluorescence intensity transient of a single MEH-PPV molecule within a PMMA host matrix during nitrogen purging (No SVA) and solvent vapor annealing (SVA). (a) The complete fluorescence transient (black curve) and the velocity (red curve) can be recorded by tracking the position of the spot. (b) Wide field fluorescence images corresponding to the fluorescence transient in (a) at the times indicated.

two conformations is reversible as shown in Figure 3.3 with two switching cycles shown here for a single CP chain.

The red curve in Figure 3.3a plots the velocity of the translational diffusion, which was measured as the shift of the centroid position of the fluorescence spot between two consecutive images. The correlation between the intensity increase, translational motion and SVA further indicates that the intensity increase occurs in the solid/liquid-like phase of PMMA. A low excitation intensity was employed ($1 Wcm^{-2}$) to avoid photophysical artifacts such as blinking and photobleaching, and therefore limited the temporal resolution in the measurements (1 s integration time). For these reasons, we were only able to observe intensity changes for slowly moving CP chains. A majority of CP chains diffuses out of the excitation area before an intensity increase can be recorded, and approximately 10% of the CP chains remain in the excitation area and they demonstrate an intensity increase before any translational movement occurs like the data shown in Figure 3.3. This indicates that unfolding can occur even before the network of the surrounding host matrix is substantially swollen, and the heterogeneity of the swelling process of the PMMA matrix leads to different diffusion coefficients as observed in Figure 3.2. Further examples of an intensity increase during SVA due to unfolding are shown in Figure 3.4 and it is also observed in a MEH-PPV bulk film (Figure 3.5).

Finally, by using fluorescence excitation polarization spectroscopy, it is revealed that in fact SVA equilibrates the conformation of single CP chains towards a lower-energy, highly ordered conformation (Figure 3.6). Hu et al. showed that this spectroscopic technique can be used on single CP chains to characterize the conformational order through the polarization excitation anisotropy, A.[47] The fluorescence intensity of single CP chains was measured while rotating the angle of the

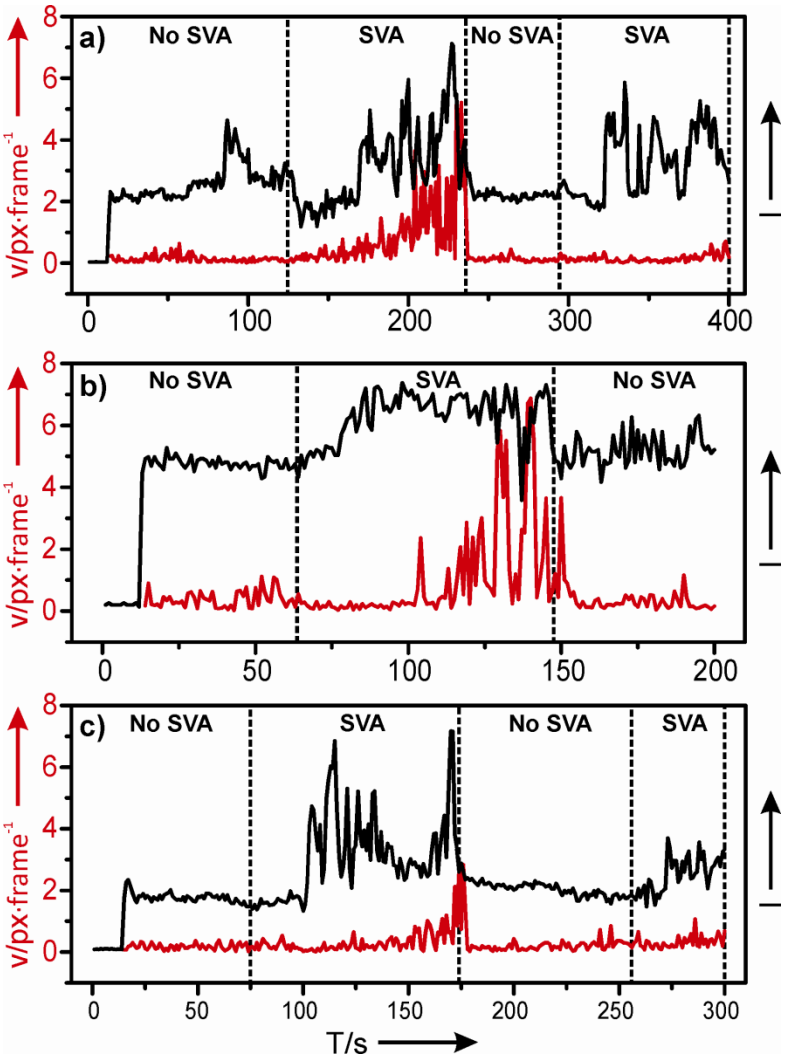

Figure 3.4: (a-c) Fluorescence intensity transients are presented of three single MEH-PPV molecules during nitrogen purging (No SVA) and solvent vapor annealing (SVA). The complete fluorescence transient (black curve) and the velocity can be recorded (grey curve) by tracking the position of the spot.

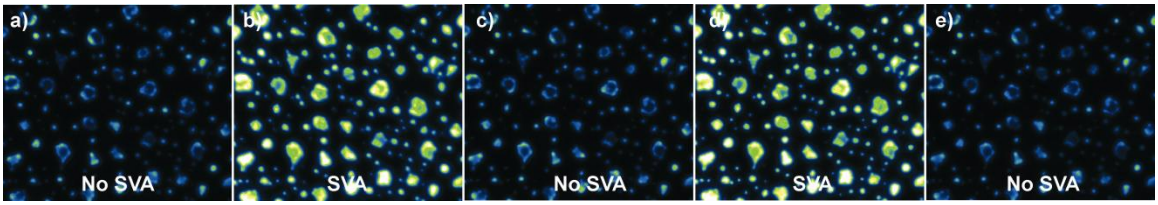

Figure 3.5: Highly aggregated MEH-PPV films prepared by spin-coating high concentration of MEH-PPV solution of THF. Wide-field fluorescence images are acquired at an excitation intensity < 50 mW cm^{-2} from the same area during No SVA (a) and during SVA with toluene (b). (c) Switching back to nitrogen purging results again in lower fluorescence intensity comparable to before SVA. This fluorescence intensity changes by switching between SVA and nitrogen purging can be reproduced for several times in the same film. Two cycles are shown (a-e).

linearly polarized excitation light in the *x*–*y* plane of the laboratory frame. The modulation depth, *M*, was obtained by fitting Equation (3.1) to the intensity vs. polarization angle, θ, where ϕ is the orientation of the net dipole moment of the polymer chain, when the emission is maximized.

$$I(\theta) \propto M \cos 2(\theta - \phi) \tag{3.1}$$

For each single CP chain, *M* was acquired and a histogram over a large number of CP chains (see caption of Figure 3.6 for details) was obtained (Figure 3.6a–d). Since *M* is only a projection of *A* onto the *x*–*y* plane, we used a model which takes the 3-dimensional and randomly distributed orientations of the CP chains as well as optical effects of the microscope into account to extract an excitation anisotropy histogram. Here an empirical Gaussian or bi-Gaussian distribution was employed. Details on the experimental setup, data acquisition, and analysis are described in chapter 2.

It has been shown that the majority of single MEH-PPV chains fold into highly ordered conformations in PMMA when a film is spin-coated from toluene.[100] Nearly identical results are demonstrated here using a sample purified by gel permeation chromatography (GPC) (Figure 3.6a). The modulation depth histogram for the sample spin-coated from toluene shows few low values, but primarily values above 0.5 with a mean modulation depth of 0.7. This modulation depth histogram including the lower values can be well described by a Gaussian distribution of *A* values (Figure 3.7a) with a mean of 0.81 and a standard deviation of 0.12 (Figure 3.6e, dotted curve). In contrast, a sample deposited from chloroform shows a broader modulation depth histogram (Figure 3.6b) that can only be sufficiently described by at least a bi-Gaussian distribution (Figure 3.7b), with mean values of 0.52 and 0.84 and standard deviations of 0.11 and 0.09, respectively (Figure 3.6f, dotted curve).

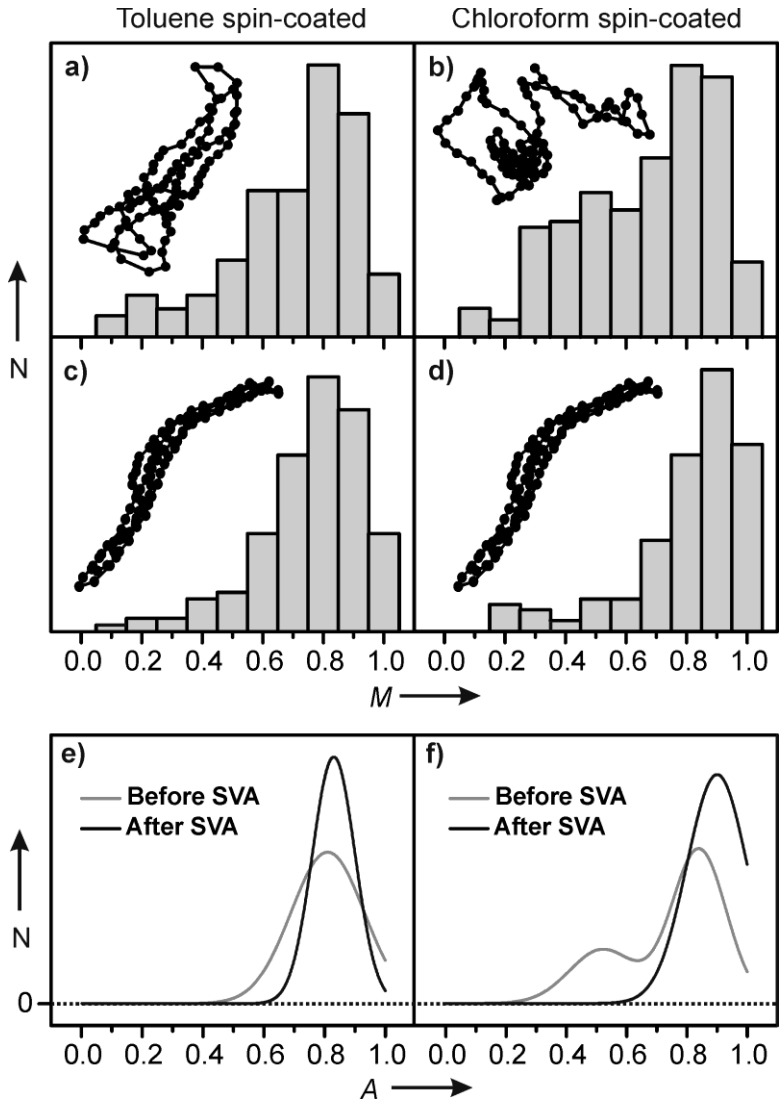

Figure 3.6: The experimental histograms of modulation depth, *M*, from single MEH-PPV molecules (number average molecular weight 830 kDa) embedded in a PMMA host matrix with different preparation methods: (a) Spin-coated from a toluene solution, (b) spin-coated from a chloroform solution. The samples from (a) and (b) were additionally solvent vapor annealed for 60 minutes with toluene-saturated nitrogen gas (c, d). The histograms consist of 152, 230, 160 and 146 MEH-PPV molecules for a, b, c and d, respectively. The insets illustrate a conformation of the molecule consistent with the mean value of histograms. (e, f) Anisotropy, *A*, distributions resolved by the best fit which generated the data shown in Figure 3.7 (striped graphs) and each corresponds to the measured modulation depth histograms shown in (a-d), respectively.

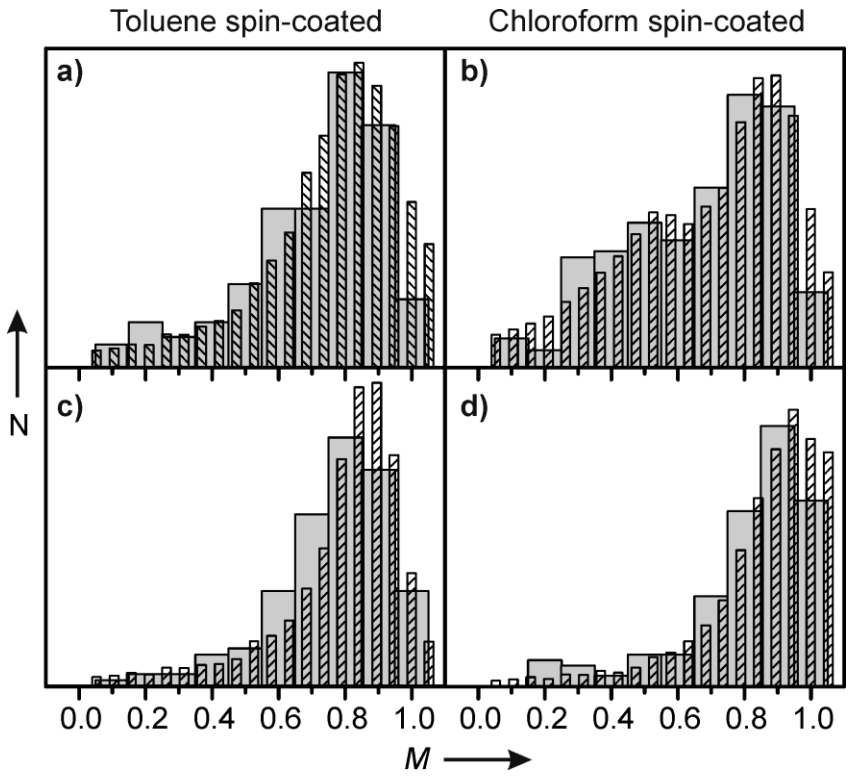

Figure 3.7: The experimental histogram of modulation depth, *M*, from single MEH-PPV molecules embedded in a PMMA host matrix (number average molecular weight 830 kDa) at different preparation methods. (a) Spin-coated from a toluene solution, (b) spin-coated from a chloroform solution and same samples additionally solvent vapor annealed for 60 minutes with toluene saturated nitrogen gas (c, d). The striped bars represent the best fit modulation depth generated from the anisotropy distributions shown in Figure 3.6.

These samples were additionally solvent vapor annealed for 60 min with nitrogen gas saturated with toluene. After SVA, a striking change in the modulation depth histograms was probed by excitation polarization fluorescence spectroscopy. Both samples spun from toluene and chloroform following SVA demonstrate a sharper distribution compared to the samples before SVA (Figure 3.6c,d). Very similar single Gaussian anisotropy distributions are extracted for both samples with a mean of 0.83 and a standard deviation of 0.07 for the sample spin-coated from toluene and a mean of 0.90 and a standard deviation of 0.1 for the sample spin-coated from chloroform, respectively (Figure 3.6e,f black curves). Possible conformations, which would lead to the measured mean values, are presented as insets in Figure 3.6a–d to illustrate the conformational change. The number of detected spots, the intensity of the spots, and the film thickness (as measured by atomic force microscopy, see Figure 3.9) remain the same before and after SVA. These similar pre- and post-SVA results demonstrate that within the time scale of the experiment, aggregation, dissociation, photo degeneration, and de-wetting can be neglected during the SVA process.

Additional studies of SVA with chloroform- instead of toluene-saturated gas reveal similar trends in the anisotropy distribution for a sample spin-coated from chloroform (Figure 3.8). The obtained values for the Gaussian anisotropy distributions after SVA with toluene and chloroform (mean of 0.9 and standard deviation of 0.1 for toluene SVA, mean of 0.87 and standard deviation of 0.16 for chloroform SVA) indicate little dependency on the solvent used for SVA as long as the solubility of MEH-PPV/PMMA and the solvent vapor is sufficient. In contrast, the solubility of PMMA in hexane is limited, and control experiments with hexane-saturated gas reveal no changes during and after SVA. These data reveal that the influence of solvents used for the spin-coating process on the conformation of single CP chains is minimized or eliminated after

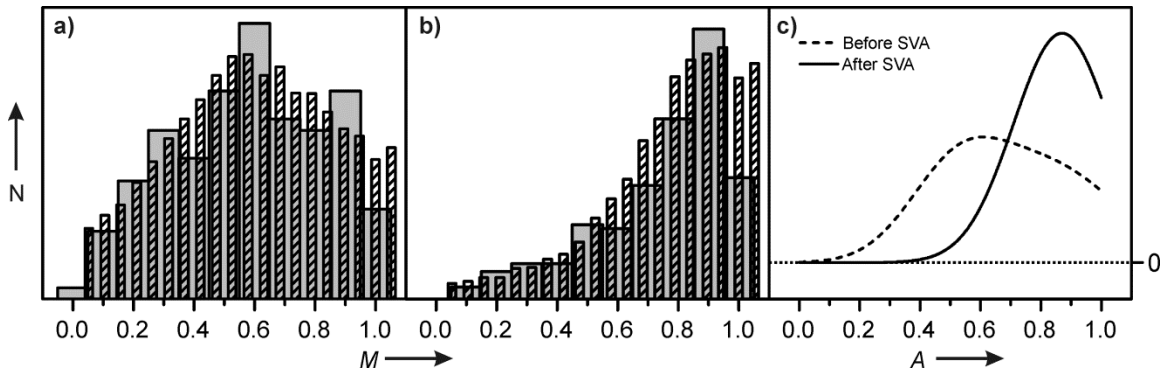

Figure 3.8: The experimental histogram of modulation depths, *M*, from single MEH-PPV molecules (number average molecular weight 830 kDa) embedded in a PMMA host matrix spin-coated from a chloroform solution (a). Same sample additionally solvent annealed for 60 minutes with chloroform saturated nitrogen gas (b). The striped bars represent the best fit modulation depth generated from the anisotropy distributions shown in (c).

SVA with good solvents, allowing the chains to fold into low-energy, highly ordered conformations upon SVA. It has been reported that single CP chains in a PMMA matrix spin-coated from chloroform produces disordered conformations while toluene produces more ordered conformations, for which the reason is still under discussions.[108] Since both toluene and chloroform SVA produces low-energy, highly ordered conformations but different conformations upon spin-coating, we suggest that the increased disorder in samples spin-coated from chloroform can be attributed to the lower boiling point of chloroform (334 K) compared to toluene (383 K). The evaporation rate during the spin-coating process is higher for the lower boiling point solvent, which leads to a higher probability of trapping the CP chains in a high-energy, disordered conformation. For example it was shown that a high rotation speed (8000 rpm) during the spincoating process of bulk MEH-PPV films leads to a high evaporation rate of the solvent, and it was observed that the CP chains become kinetically trapped in their solvent configuration.[109]

3.4 CONCLUSION

Solvent vapor annealing is one of the most important industrial techniques used to improve device properties such as the efficiency of organic solar cells, but little is known about the molecular details of SVA. Herein, we prove that single molecule fluorescence spectroscopy is capable of giving us a fundamental understanding of SVA on the molecular level. It was shown that SVA in fact equilibrates the conformation of CP chains even though the CP chains are trapped in a high energy, disordered conformation prior to SVA due to the use of spin-coating with different solvents. SMS also enabled us to study the details of the SVA process. During SVA, the film absorbs solvent lowering the glass transition temperature below the ambient temperature, and translational motion of the CP chains can be observed within this solid/liquid-like film. Further, it was shown

that the CP chains undergo folding and unfolding events between a collapsed and extended conformation during SVA, which finally leads to a lower energy, highly ordered conformation after the solvent vapor is removed.

Acknowledgement for co-author contributions:
I would like to thank Dr. Jan Vogelsang, Dr. Johanna Brazard and Dr. Joshua Bolinger for helping me performing the experiments, and Prof Paul F. Barbara for designing the experiments.

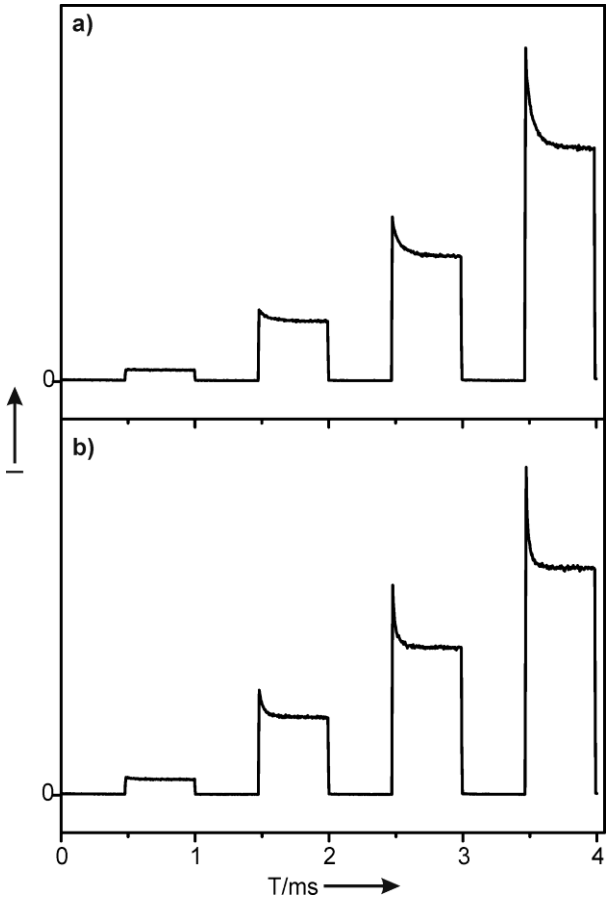

Figure 3.9: Results of the intensity pulse modulation experiment. Ensemble average from ten MEH-PPV molecules in the flow chamber during nitrogen purging (a) and in epoxy-resin sealed samples used in ref [100]. (b). Both samples show high initial intensity, fast decay, and large contrast ratio, consistent with triplet population build up proving the absence of oxygen in a film examined.

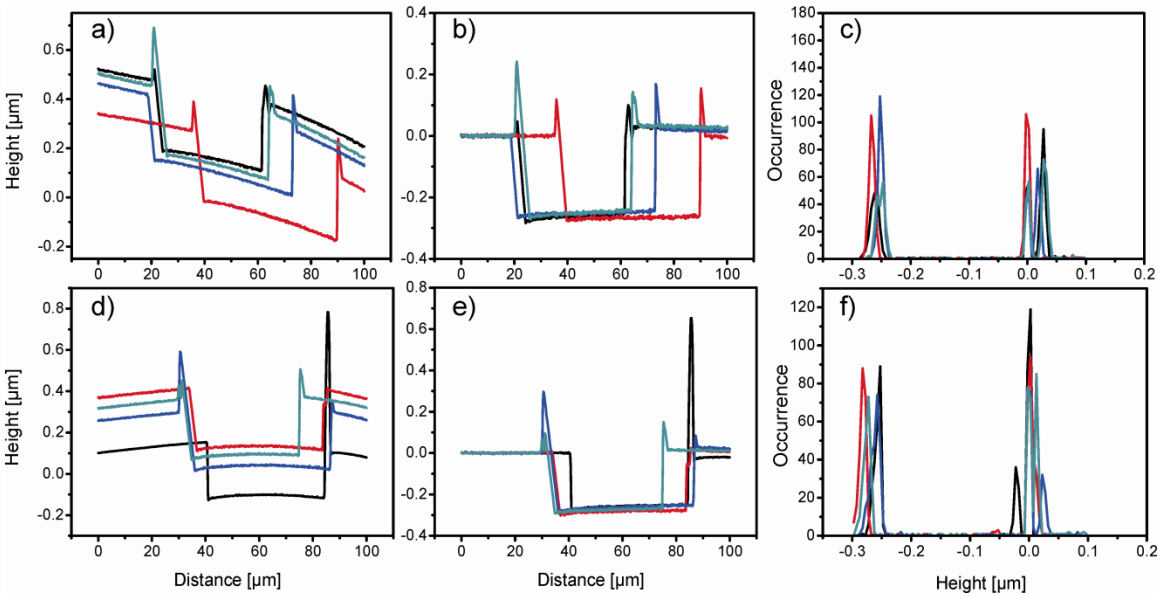

Figure 3.10: Cross-sections of a scratch upon a PMMA film acquired by atomic force microscopy. (a, d) shows the raw data of 4 cross-sections at different positions, (b, e) the corrected data and (c, f) the histograms of the height values from the corrected data. (a-c) is from a PMMA film without solvent vapor annealing whereas (d-f) is from a PMMA film after solvent vapor annealing with toluene.

Chapter 4: Ultralong-Range Polaron-Induced Quenching of Excitons in Isolated Conjugated Polymers

This chapter was reproduced in part from: Bolinger, J. C.; Traub, M. C.; Adachi, T.; Barbara, P. F. *Science* **2011**, *331*, 565.

4.1 INTRODUCTION

The performance of conjugated polymer (CP) based electro-optic devices, such as light emitting diodes and organic photovoltaic solar cells, can be degraded via quenching of the excitons (electron-hole pairs) through their interaction with hole polarons (p^+)**.** Previous electrical and single molecule spectroscopic experiments have demonstrated the existence of p^+ traps in CPs[110,111]. As in the more extensively studied quenching of electrically excited molecules by electron acceptors in dilute solution, exciton quenching in the solid-state is expected to occur by electron transfer from the exciton to p^+. In conjugated polymers, the exciton-to-polaron electron transfer process results in spatial displacement and detrapping of the hole[112,113]. The limited spatial resolution of conventional far-field fluorescence microscopy has constrained the ability to make real space measurements of the distance scale for exciton/polaron quenching[114]. Instead, it has been investigated primarily by ensemble measurements of fluorescence quenching induced by charge injection from electrodes on bulk samples[115]. Such measurements, which are not spatially resolved and indirect in nature, can be misleading because they spatially average over a highly disordered morphology. As a result, very little is known at the molecular level about the mechanism of polaron-induced exciton quenching.

We introduce an electro-optical, subdiffraction single molecule spectroscopy imaging technique, bias-modulated intensity-centroid spectroscopy (BIC). We used this method to spatially resolve the distance scale for fluorescence quenching caused by singlet exciton deactivation by p^+ in isolated single polymer chains of poly[2-methoxy-5-

(2'-ethylhexyloxy)-1,4-phenylenevinylene] (MEH-PPV) embedded in a nonconducting polymer, poly(methyl methacrylate) (PMMA). BIC combines single molecule spectroscopic techniques previously introduced for the investigation of exciton/polaron interactions[40,110] with sub-diffraction single molecule imaging methods, such as photoactivated localization microscopy (PALM) and stochastic optical reconstruction microscopy (STORM)[116-118] that allow for the localization of fluorescent dyes in biological samples on the <10-nm scale. In contrast to PALM and STORM, BIC is designed to measure the distance scale of an electro-optical physical process, not just the molecular location. In this study, a semiconductor capacitor-like device structure (Fig. 4.1A) is used to controllably charge and discharge single polymer molecules with one or more p^+ by modulating the bias across the device in the appropriate range[110]. Holes are injected from an adjacent hole transport layer in contact with the single molecules.

4.2 EXPERIMENTAL SECTION

4.2.1 Sample Preparation

The device used for single molecule charge injection was a large area multilayer structure, as shown in Figure 4.1A. The device was fabricated bottom-up on a patterned indium tin oxide (ITO) coated quartz coverslip (Evaporated Coatings, Inc, sheet resistance of 110 Ω/□) by using previously described procedures,[110] with any changes noted below. Briefly, SiO_2 was deposited by inductively coupled plasma chemical vapor deposition (ICP-CVD) at 200 °C (Oxford Instruments, Plasmalab 80plus) for a film thickness of 70 nm as an insulating layer. The remaining device fabrication was performed in a dry N_2 environment (O_2 and H_2O concentrations < 5 ppm). Poly(methyl methacrylate) (PMMA, M_n = 101 kg/mol) was purchased from Sigma Aldrich CO. Poly[2-methoxy-5-(2'-ethylhexyloxy)-1,4-phenylenevinylene] (MEH-PPV, M_n = 150

kg/mol, PDI = 3.0) was purchased from Polymer Source Inc. and used without further purification. PMMA/MEH-PPV layers (25 nm) were deposited by spincoating from toluene (Sigma Aldrich, anhydrous 99.8%) and the MEH-PPV concentration was adjusted to obtain an areal density of ~0.1 molecules/μm^2 in the sample. Thermal evaporation was used to deposit the hole transport layers, 4,4-*N*,*N*-dicarbazole-biphenyl (CBP) (Sigma Aldrich, 98%), and *N*,*N*-bis(3-methylphenyl)-*N*,*N*-diphenylbenzidene (TPD) (Sigma Aldrich, 99%), and for the gold electrode (Cerac, 99.99%). Thermal depositions were carried out at 10^{-4} Pa, and typical rates were 1 Å/s as measured by a quartz crystal microbalance. Thicknesses for these layers were 25 nm for CBP and TPD and 50 nm for Au. All layer thickness measurements reported here were confirmed by atomic force microscopy (Digital Instruments, Dimension 3100) and/or ellipsometry (J A Woollam Co. Inc, M-2000). Before measurements on the microscopy setup, devices were wired and packaged in an inert environment to exclude water and oxygen.

The same type of devices was fabricated for BIC measurement on MEH-PPV nanoparticles (NPs). NPs were prepared by re-precipitation method in a dry N_2 environment. Briefly, a small aliquot of a concentrated solution of MEH-PPV (~1 mg/ml) in tetrahydrofuran is 'flash'-injected into a solution of poly(isobutyl methachrylate) (PIM, Acros, M_n = 300 kg/mol) in cyclohexane. The size of the resulting NPs (the radius of 25 ± 15 nm) was estimated by comparing the single NP fluorescence intensity distribution to that of a reference NP sample with a known size distribution (measured by Scanning Electron Microscopy). The resulting colloidal suspension is spin-cast to form the PIM/NP layer (10 nm), the NP concentration was adjusted to obtain an areal density of ~0.1 particles/μm^2 in the sample.

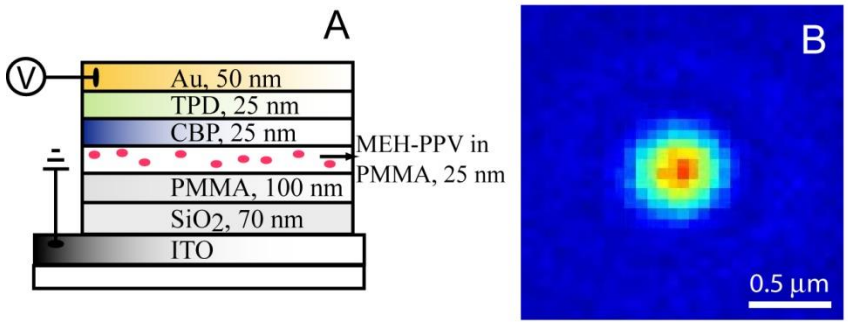

Figure 4.1: (A) Structure of the hole injection device used in these studies. (B) False color image of a single molecule of MEH-PPV imbedded in the hole-only device.

4.2.2 Experimental Setup

Studies were performed on an inverted wide-field microscope (Zeiss, Axiovert 100) with excitation from an Ar Kr ion laser (Melles Griot, 35-LTL-835). The output of the laser was filtered spatially with a prism and further resolved with a 488-nm interference filter (Semrock, Maxline). The light was circularly polarized using a λ/4 waveplate and the intensity was attenuated with neutral density filters to provide 50 W/cm^2 excitation. The FWHM of the spot size was measured to be 60 μm. Fluorescence was collected by a 100x oil immersion objective (Zeiss, Achrostigmat 1.25 NA) and was imaged on an EMCCD (Andor, iXon+) using a 2.5x tube lens for a total magnification of 250x (Figure 4.1B). A 488-nm holographic notch filter (Semrock, Stopline) was employed to eliminate residual laser line scatter from the fluorescence signal. Sample positioning was accomplished through the use of a closed loop piezoelectric *x-y* stage (Queensgate, NPS-100A) driven by a computerized controller (RHK, SPM1000), and bias modulation of the sample was done through a programmable function generator.

4.2.3 Centroid Fitting Procedure

Following image acquisition, data files were processed using a home written MATLAB program. Molecules were manually chosen from the image and fitted individually. To prevent fitting artifacts due to the Gaussian excitation profile of the laser, an area of 20x20 pixels surrounding the molecule of interest, excluding the molecule itself were fit to a plane and then subtracted from the region of interest, flattening the local background. Following the background subtraction, fitting for the centroid position was performed one of two ways. The first was a 2D least squares fit to a Gaussian distribution while the second was least squares fit employing a Gaussian mask algorithm.[119] Both fitting procedures produced identical centroid locations within error and the Gaussian least squares fitting was primarily used over the mask algorithm fitting

routine due to the increased computational time from the mask algorithm. Stage drift on the timescales of these experiments could not be ignored. In most cases, the drift observed was linear in nature, and a simple linear regression was performed on both the unaveraged X and Y centroid transients and subtracted. If the drift was obviously nonlinear in time, the data was discarded.

4.3 RESULTS AND DISCUSSION

The degree of charging of a particular molecule is indirectly measured by recording the synchronously averaged integrated intensity (I_{fl}) of its fluorescence spot (Figure 4.1B) as a function of the bias E(V) across the device, which is modulated periodically in a square-wave (Figure 4.2A). For the bias conditions in Figure 4.2 the quenching is about 60% during the more positive portion of the bias cycle, which corresponds to the injection of approximately one p^+ for a MEH-PPV macromolecule with a molecular weight (M_w) of ~ 150,000, i.e. the range of materials studied in Figure 4.2[40,110]. The fluorescence intensity centroid of the single CP molecule can be determined by a 2D Gaussian fitting procedure of the time-dependent fluorescence images. This centroid was displaced periodically in the sample (x, y) plane as the bias was modulated and, in turn, the fluorescence quenching was initiated because of the p^+ injection, see Figure 4.2B. The total bias-dependent centroid displacement was calculated from the orthogonal (X and Y) displacements in the laboratory frame.

A striking feature of the results in Figure 4.2B is that the centroid displacements as a function of bias are nearly identical for each cycle. This pattern allows for synchronous averaging of the displacement data, leading to an improved signal-to-noise ratio for the X and Y components of the centroid determination with a mean standard deviation for the X and Y position determination as small as 0.5 nm despite a diffraction limit of ~300 nm (Figure 4.2C). The plateaus in the X and Y component data in Figure

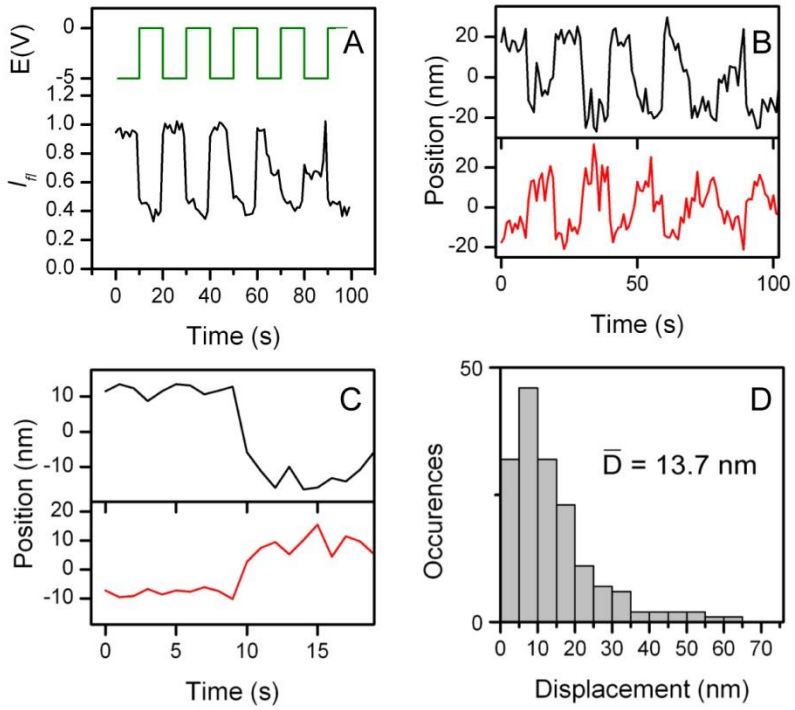

Figure 4.2: (A) F-V measurement of the molecule shown in Figure 4.1B where the fluorescence trajectory is shown in black and the applied bias is shown above, in green. (B) The centroid displacement of the fluorescence point spread function resulting from the applied bias shown in (A) where displacement in the X direction is shown in the top panel (black), and Y is shown in the bottom panel (red). (C) Synchronized average of the X (black line) and Y (red line) centroid displacement obtained from (B). (D) Histogram of the total centroid displacement (*D*) for 167 different single molecule MEH-PPV (MW = 150k) transients. Values peak at 9.8 nm while the mean value is 13.7 nm.

4.2C for the vast majority of the molecules investigated (>95%) exhibited roughly constant values during the uncharged (lower bias) and charged (higher bias) periods and reflected the X, Y centroid positions that correspond to these two cases. These data can be used to calculate the magnitude of the in-plane vector displacement, *D*, of the centroid induced by p^+ injection into the molecule. For the molecule portrayed in Figs. 4.2, A to C, this procedure gives a measured *D* value of 29.4 +/- 3.9 nm.

A histogram of *D* values for 167 molecules of MEH-PPV (Figure 4.2D) shows that the magnitudes of the displacements range from 0 to over 60 nm with a peak and mean displacement of 9.8 nm, and 13.7 nm, respectively. The p^+ induced quenching for the molecules in this histogram falls in the range of 40 to 80% with a mean of about 60%. Based on previous photoxidation studies, for single CP chains this quenching depth corresponds to ~1 charge per molecule[120]. The reproducibility of *D* (and its X and Y components) over repeated charging cycles implies energy transfer from excited chromophores to a single stationary (or trapped) p^+, which is injected to the same location along the polymer chain for all cycles for a given molecule. This is strong evidence for the previous proposal that a p^+ injected into a single polymer chain located on an organic electrode is trapped in a pre-existing site with a low-energy highest-occupied-molecule-orbital (HOMO)[110]. One candidate for a low-HOMO-energy site for p^+ is a location along the polymer chain where the chain make extraordinarily close contact with itself, allowing for pi stacking interactions which can stabilize the hole by delocalization[121].

It is unlikely that observed centroid displacements are caused by actual translocation of the CP molecule because the materials that comprise the device are rigid solids. Instead, we assign the observed displacement in centroid position to selective quenching of some of the ~100 different chromophores that comprise the 150,000 M_w multichromophoric single CP molecule. Based on previous non-spatially resolved

spectroscopic measurements and modeling studies[47], each single molecule is expected to be in a collapsed, approximately cylindrical conformation with dimensions in the ~5 x 200-nm range. Thus, despite the undoubtedly complex local intramolecular intensity pattern of emitting sites, the spatial substructure in each conjugated polymer is difficult to resolve directly because of the diffraction limit. To ensure no instrumental bias in the measurement, the average X and Y displacement for 136 molecules are presented in the histograms in Figure 4.3A and 4.3B along with the total displacement 4.3C. They show that there is no molecular preference for displacement in either the X or Y direction, which is further confirmed by a histogram of the displacement angle in the x-y plane shown in Figure 4.3D. This is consistent with an isotropic distribution of molecule orientations after the spincasting process. Fewer than 5% of the molecules in the devices showed no fluorescence intensity modulation nor centroid shift with the application of an electric bias, ruling out manipulation of the centroid by electric fields. These control experiments verified that the observed centroid displacements are not caused by potential artifacts, such as sloping background profiles, detector artifacts, or inaccuracies in the use of fitting with a single 2D Gaussian function to determine the centroid position for a closely spaced collection of emitting chromophores.

The dynamics of this displacement of the intensity centroid caused by trapped $\boldsymbol{p}^+$ can be explored by considering simulations of the quenching of a multichromophoric molecule. Because charge transfer processes are most effective at distances <1 nm, we hypothesize that the actual charge transfer quenching step is preceded by multiple Förster energy transfer events, each of which can operate at distances of ~ 5 nm. Presented in Figure 4.5A is a graphical representation of a polymer chain embedded in the charge injection device. The chain was generated by a previously described beads-on-a-chain Monte Carlo simulation that is capable of producing many different molecular

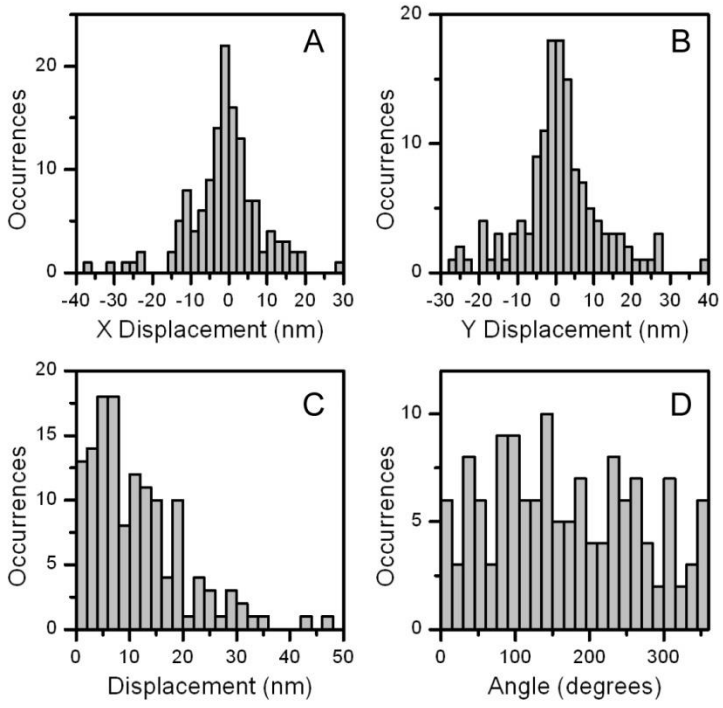

Figure 4.3: Histograms of 136 single molecule MEH-PPV (MW = 1000k) F-V transients where each molecule is an average of ten bias modulation cycles. (A) and (B) represent the centroid displacement of the fluorescence signal during bias modulation in the x and y direction, respectively while (C) and (D) represent the total displacement and angle of the centroid displacement in the X-Y plane, respectively.

configurations[47]. The exact conformation of a single polymer molecule is unknown; however given the extraordinary distances that centroid displacement is occurring over, one molecular axis must be relatively large compared to the others. In support of this hypothesis, lattice models with a fixed volume were constructed to simulate multichromophore molecule quenching via a Förster type process.

As a starting point for the simulations we make the following simplifying assumptions. Each emitting molecule is a rectangular prism comprised of an array of identical 1-nm cubic, chromophores, see Figure 4.4A and B for molecules of different shape and size. The florescence quenching is calculated from an incoherent sum of the intensities over the sites, j, with and without a single $\boldsymbol{p}^+$ located at site k. The intensity I of each site is calculated from

$$I = 1 - \frac{1}{1 + \left(\frac{d_{j,k}}{R_0} \right)^6} \tag{4.1}$$

Here R_0 is the Forster radius and $d_{j,k}$ is the distance between the sites of the specific emitting chromophore and $\boldsymbol{p}^+$. The centroid (actually the X, Y projection of the centroid) is calculated by summing over all chromophores. The results are further averaged over a random set of hole locations and orientation of the single molecule, producing a distribution (histogram) of D values, e.g. Figure 4.4D.

The simulations demonstrate that in order to reproduce the observed large >10 nm D values for a conjugated polymer molecule of the expected approximate molecular volume of 1800 $nm^3$of a collapsed conformation (assuming a MW of 900,000 and a density of 0.8g/cm^3), the molecule must have a highly asymmetric shape, such as Fig. 2A. The maximum value of D is ~1/3 of the long axis. Due to variation in the locations of the trapped $\boldsymbol{p}^+$ the D histogram for the highly asymmetric molecules includes some small D values. Much smaller D values are found for symmetrical molecules of the

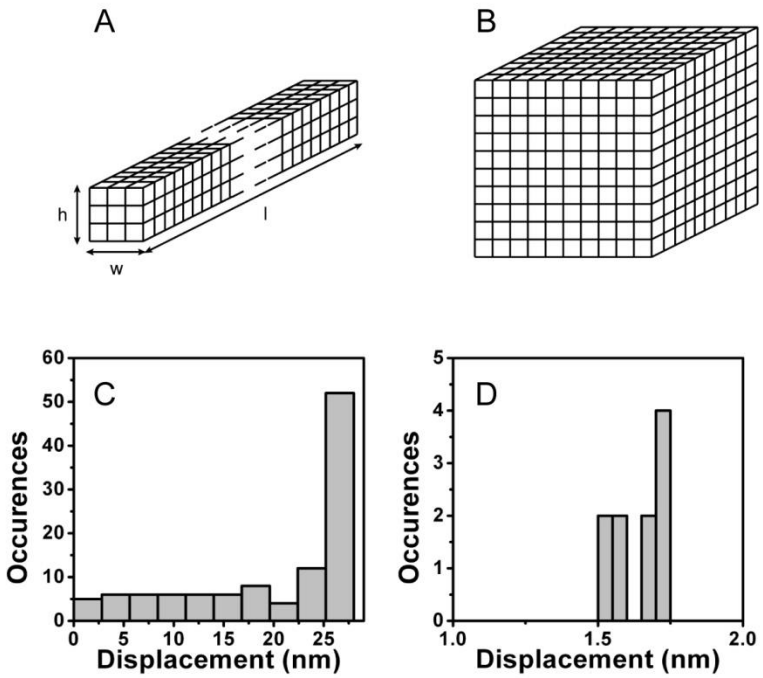

Figure 4.4: (A-B) molecular shape used for the simulation. (A) h = w = 3, l =111 (B) h = w = l = 10. The displacement histograms (C), (D) generated for the case when the hole was located at the bottom of the molecule. (w =2, h = 1 and summed over all values of l)

appropriate volume, such as in Figure 4.4B and D. Since the *D* value cannot exceed the actual physical length of the molecule, smaller *D* values are expected for the highly symmetrical molecules of the same polymer chain length. Considering the trends in the simulation we tentatively assign the width and shape of the *D* distribution (Figure 4.2D) primarily to a distribution of molecular shapes and to a lesser extent M.W. and the locations of $\boldsymbol{p}^{+}$. Furthermore, it should be emphasized that the assumption of a uniform spatial distribution of chromophores may be inaccurate for molecules that have two or more condensed conformational domains.

The results of these simulations suggest that only highly asymmetric configurations (a long, rectangular lattice array as opposed to a cubic one) can produce large centroid displacements. Additionally, current work on absorption polarization of single polymer chains of MEH-PPV demonstrates a single population of molecular conformations with a high anisotropy value.[100] Coupled with the large centroid displacements observed in this work, we propose that a needle-like structure as shown in Figure 4.5A is appropriate.

Using the molecular conformation shown in Figure 4.5A, a simulation similar to the lattice model was performed in which each bead is an individual chromophore. A random bead on the chain was assigned as a quenching site. For illustrative purposes, we used a single step Förster quenching mechanism as described in the supporting information, and varied the distance of energy transfer (R_0) relative to the length of the molecule (L_h). The impact of changing this distance on the centroid displacement is presented in Figure 4.5, B to D. Simulated average fluorescence intensity as a function of the ratio of R_0 and L_h is shown in Figure 4.5B. Unsurprisingly, values of R_0/L_h of 0 and 1 produce no fluorescence quenching and complete fluorescence quenching, respectively, whereas $R_0/L_h = 0.5$ produces 75% fluorescence quenching.

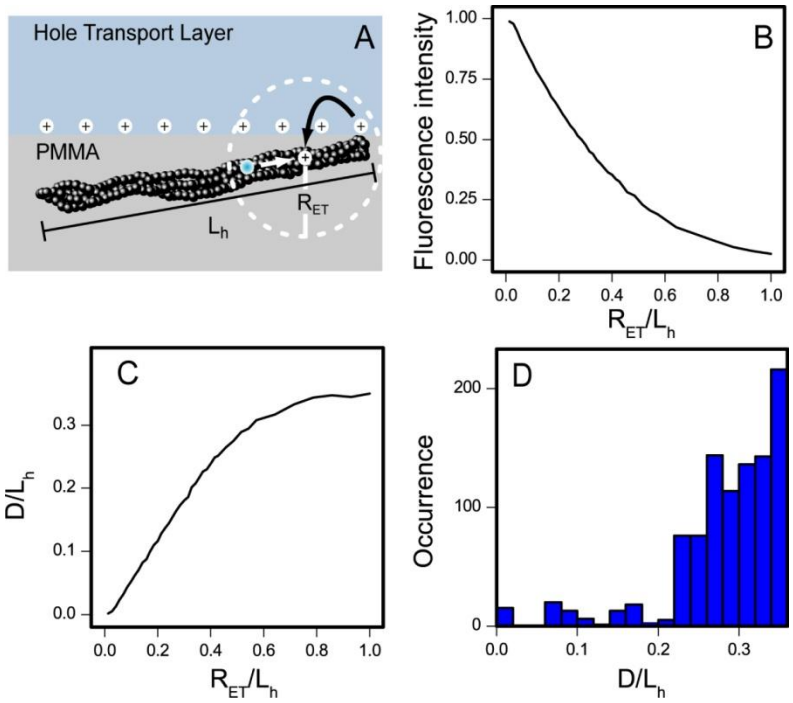

Figure 4.5: (A) Illustration representing a beads-on-a-chain model of a folded polymer chain, with length L_h(see text), at the CBP/PMMA interface. Injection and localization of a hole polaron from the CBP layer into the polymer chain is represented by the black arrow. Energy transfer of an exciton (cyan circle) on the chain is represented by the white arrow. The effective quenching radius of the hole polaron is shown with the white dashed circle with FRET radius R_0 (B) Average calculated fluorescence intensity from the molecule depicted in (A) as a function of the ratio of R_0 and L_h. (C) Average calculated centroid displacement as a fraction of the length L_h from the molecule depicted in (A) as a function of the ratio of R_0 and L_h. (D) Histogram of possible centroid displacement values calculated from the molecule depicted in (A) assuming a value of $R_0/L_h = 0.5$ for the quenching radius and that the quenching site can occupy any site on the chain. Centroid displacements are given as a fraction of the length of the chain, L_h.

Figure 4.5C compares average centroid displacement vs. energy transfer distance. The centroid displacement plateaued at a value of ~1/3 the length of the molecular axis at high values of R_0. Figure 4.5D plots the distribution of centroid displacements calculated for R_0/L_h = 0.5 and with this parameter, the displacements are weighted heavily between 25% and 35% of the length of the folded polymer chain. The large D values (e.g. >10 nm) thus imply that one molecular axis of the polymer chain must be at least 3 times the size of the observed displacement and are only observed for R_0 values that are >25 nm and in some cases >75 nm.

These R_0 values are much greater than the largest R_0 values calculated for Förster energy transfer between two well-aligned CP chromophores with excellent spectral overlap, i.e. R_0 <6 nm. Unsurprisingly, preceding the exciton quenching with a single-step, downhill energy transfer by a Förster mechanism is inconsistent with the observed centroid displacement results. Instead, it is likely that multistep interchromophore energy transfer precedes the actual quenching step. The bulk diffusion length of 5 nm[115] for energy migration in PPVs is, however, too small to explain the up to 60 nm observed exciton quenching lengths. It may be that energy diffusion is more rapid and occurs over a larger distance for single polymer chains than for bulk CP materials. BIC measurements of aggregated nanoparticles of MEH-PPV confirm this, showing an order of magnitude smaller centroid displacement upon charge injection (Figure 4.6). Single polymer chains are more ordered than chains in the bulk materials, and are more favorable for rapid energy diffusion. Furthermore, single polymer chains contain few if any "red" sites (low energy emitting sites), which are known to effectively trap excitons in bulk materials.[122]

Previous studies have modeled exciton relaxation in single conjugated polymer chains, suggesting that disorder in the chain prevents long distance energy transfer.[123]

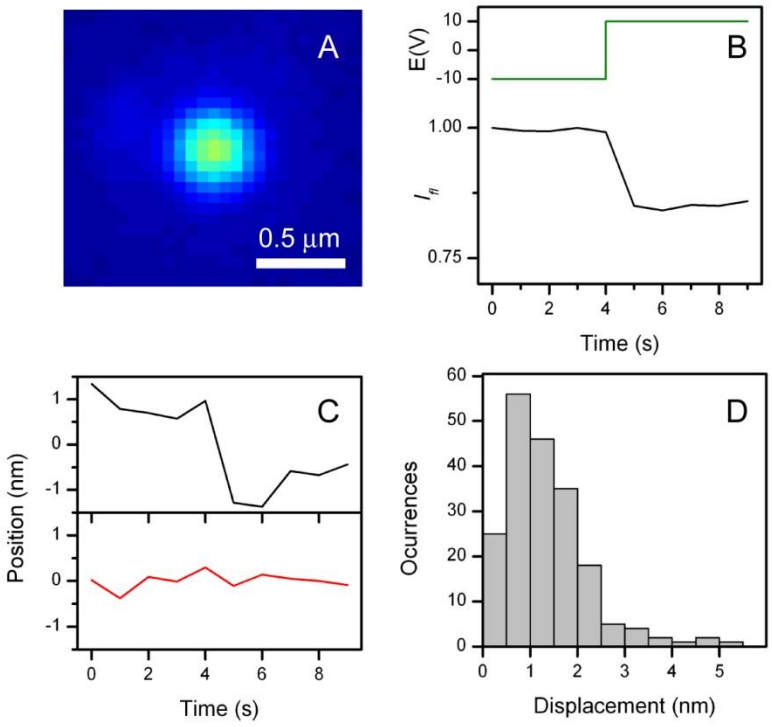

Figure 4.6: (A) False color image of a nanoparticle aggregate of MEH-PPV imbedded in the hole-only device. (B) F-V measurement of the nanoparticle shown in (A) where the fluorescence trajectory is shown in black and the applied bias is shown above, in green. (C) Synchronized average of the x (black line) and y (red line) centroid displacement obtained from (B). Histogram of the total centroid displacement for 195 different nanoparticle aggregates of MEH-PPV. Values peak at 0.8 nm while the mean value is 1.3 nm.

Directional energy transfer (i.e. energy funneling) in an ordered system toward the trapped polaron would be especially effective at producing large centroid displacements in the BIC experiment because it achieves a large displacement with a small number of hops. Energy funneling could be enhanced by a spatially dependent Stark effect on the S_1-S_0 energy gaps of the chromophores in the vicinity of p^+. This process would enhance both the rate and degree of directionality of the energy transfer process. Another hypothetical mechanism for enhanced energy funneling is an ultra long-range electron transfer involving rare delocalized electronic states [124].

The single molecule *D* measurements reported in Figure 4.2 correspond to quenching depths of ~ 60% which for 150,000 M_w. molecules corresponds to roughly one p^+. In order to explore the interaction of more than one p^+, we recorded *D* values for larger quenching depths. We used a bias waveform with a repetitive linear ramp function rather than the square wave used for the experiments in Figure 4.2. The X and Y components of the displacement are plotted in Figure 4.7B for various times on the synchronously averaged data. The biases that correspond to each time are written in red next to each X, Y pair and a line is drawn through the data to guide the eye. From -3.3 to -2.1 V the apparent X, Y displacements increase in magnitude because of an increase in the fraction of the time the molecule is occupied by a p^+. Throughout this bias range, the best-fit D value increases while the in-plane direction of displacement is unchanged. As the bias is varied to be even less negative, the Y displacement abruptly reverses. This reversal is assigned to quenching from a second and perhaps third charge in the molecule, which become a larger factor in the displacement data for the least negative biases. This experiment was reproduced for 50 molecules and an analogous effect was observed (Figure 4.8). These data suggest that the position of the second injected p^+ is not co-located with the injected hole but rather at a remote location. These results represent

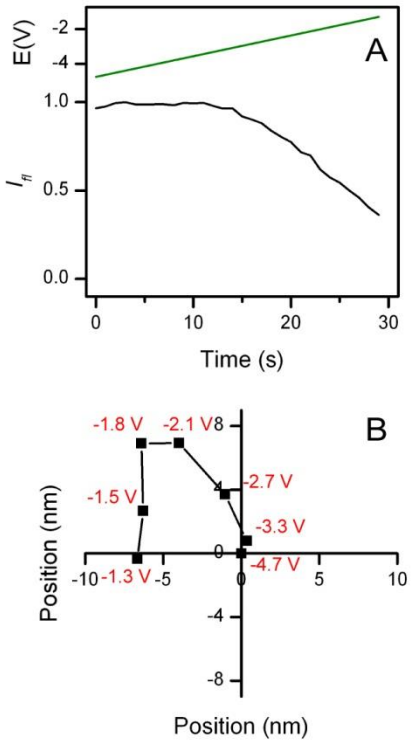

Figure 4.7: (A) Synchronously averaged fluorescence transient of a single molecule (black) with the ramp bias applied as shown above (green). (B) Synchronized average of the point spread function centroid position obtained from the single molecules shown in (A) with the voltage for each point shown in red (some points omitted for clarity).

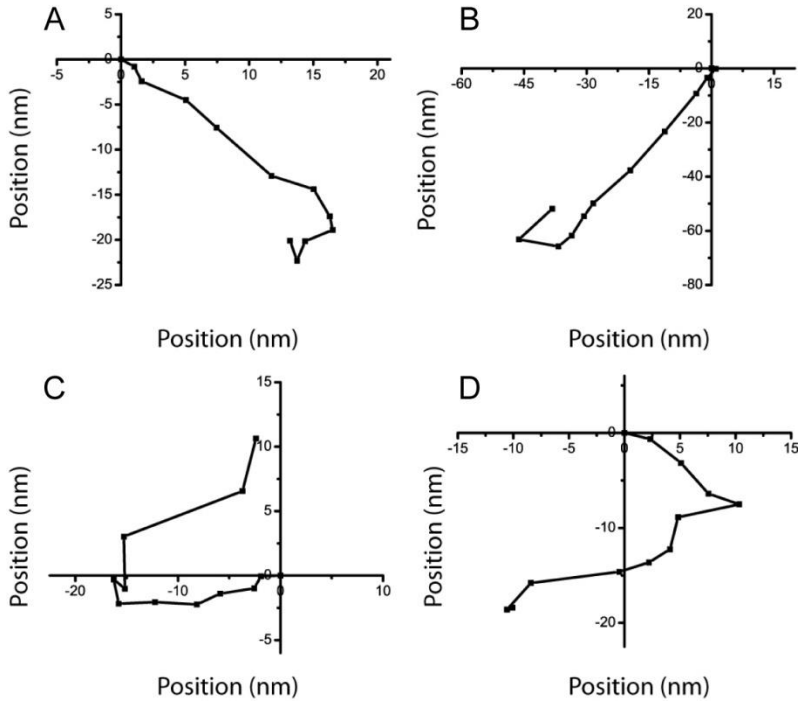

Figure 4.8: (A-D) Four examples of synchronized average of the point spread function centroid position obtained from the single molecules while the ramp voltage shown in Figure 4.7A was applied.

spatially resolved evidence against the bipolaron hypothesis—that the p^+ are not coupled. Instead, the location (perhaps random) of the trapped p^+ species is probably dictated by the location of low energy sites in the polymer chain conformation.

4.4 CONCLUSION

In conjugated polymers, radiative recombination of excitons (electron-hole pairs) competes with non-radiative thermal relaxation pathways. We visualized exciton quenching induced by hole polarons in single polymer chains in a device geometry. The distance-scale for quenching was measured by a new sub-diffraction, single molecule technique, bias-modulated intensity centroid spectroscopy, which allowed the extraction of a mean centroid shift of 14 nm for highly ordered, single-polymer nanodomains. This shift requires energy transfer over distances an order of magnitude greater than previously reported for bulk conjugated polymers, and far greater than predicted by the standard mechanism for exciton quenching, the unbiased diffusion of free excitons to quenching sites. Instead, multistep "energy funneling" to trapped, localized polarons is the likely mechanism for polaron-induced exciton quenching. It was speculated that the striking difference between the observation herein at the single chains and bulk conjugated polymers was possibly due to the morphological differences. Single polymer chains are more ordered than chains in the bulk materials, and are more favorable for rapid energy diffusion.

Acknowledgement for co-author contributions:
I would like to thank Dr. Joshua Bolinger and Dr. Mattew Traub for helping me performing the experiments, and Prof. Paul F. Barbara for designing the experiments.

Chapter 5:Self-assembly of highly ordered conjugated polymer aggregates with long-range energy transfer

This chapter was reproduced in part from: Vogelsang, J.; Adachi, T.; Brazard, J.; Bout, D. A. V.; Barbara, P. F. *Nat. Mater.* **2011**, *10*, 942-946.

5.1 INTRODUCTION

Applications of conjugated polymers (CP) in organic electronic devices such as light-emitting diodes and solar cells depend critically on the nature of electronic energy transport in these materials.[13,125-128] Single-molecule spectroscopy (SMS) has revealed their fundamental properties with molecular detail,[40-42,47,98-100,121,129] and recent reports suggest extraordinarily long-range energy transport over distances between 25 and 75 nm in single CP chains.[44,100,130] An important question arises as to whether these characteristics are sustained when CP chains agglomerate into a neat solid.[127] In this chapter, we demonstrate that the electronic energy transport in aggregates composed of tens of polymer chains takes place on a similar distance scale as that in single chains. A recently developed molecular-level understanding of solvent vapour annealing has allowed us to develop a technique to control the CP agglomeration process.[131] Aggregates with volumes of at least 45,000 nm^3 (molecular weight ~ 21MDa) maintain a highly ordered morphology and show pronounced fluorescence blinking behavior, indicative of substantially long-range energy transport. Our findings provide a new lens through which the ordering of single CP chains and the evolution of their morphological and optoelectronic properties can be observed, which will ultimately enable the rational design of improved CP-based devices.

5.2 EXPERIMENTAL SECTION

5.2.1 Setup and Sample Preparation

The wide-field fluorescence spectroscopy apparatus and acquisition conditions for imaging and fluorescence excitation polarization spectroscopy are described in detail elsewhere[100,131]. Poly[2-methoxy-5-(2'-ethylhexyloxy)1,4-phenylenevinylene] (MEH-PPV) was purchased from Polymer Source, Inc. and further purified via GPC with a polystyrene standard to obtain a M_n = 830 kDa with a PDI of 3.5. Poly(methylmethacrylate) (PMMA, M_n = 45 kDa, PDI = 2.2) was purchased from Sigma-Aldrich Co. Glass cover slips were cleaned in an acid piranha solution (hydrogen peroxide/sulfuric acid 1:3 in volume). Isolated chains of MEH-PPV embedded in a PMMA matrix were obtained by dynamically spin-coating from toluene. The PMMA film thickness was 200 nm, and the concentration of MEH-PPV in solution before spin-coating was ~10^{-13} mol L^{-1}, resulting in a final spot density of about 0.1 spots/μm² for the single-CP-chain samples. To avoid any photo-oxidation, samples were prepared in a glove box (MBraun, with O_2 and H_2O less than 5 ppm) and investigated in the microscope apparatus (see chapter 3) equipped with a home-built gas flow cell to purge the sample with nitrogen gas, preventing exposure of the sample to oxygen or moisture. To prepare the aggregates during SVA, a 50x-higher MEH-PPV concentration was used (~$5 \cdot 10^{-12}$ mol L^{-1}). These samples were additionally solvent vapor annealed with a V_g/V_b ≈ 0/100, 10/90, 20/80 and 40/60 for 30 minutes to generate four different sizes of aggregates (Figures 5.7 and 5.8). For SVA, the nitrogen gas was saturated with the respective solvent (chloroform-acetone mixture) by slowly purging the gas through a reservoir of the solvent mixture. The necessary solution ratio of the chloroform-acetone mixture was calculated by using a phase-diagram of the chloroform-acetone system at 22° C to obtain the above-mentioned chloroform/acetone vapor ratios, V_g/V_b. After SVA,

the solvent vapor was removed by purging the sample with pure nitrogen gas for a few minutes and all the optical measurements were performed under nitrogen atmosphere. The same excitation and acquisition conditions were applied to all samples. However, an intensity threshold above the intensity of single CP chains was applied to the aggregated samples to measure primarily aggregates.

5.2.2 Quenching Depth Analysis

Fluorescent transients of single CP chains and aggregates were acquired via time-resolved wide-field fluorescence microscopy and further analyzed with respect to the quenching depth of each blinking event with an algorithm written for MATLAB. First, the maximum intensity, I_{max}, of each transient was extracted by averaging over the 10 highest data points within the transient. This led to averaging over 1 s of the highest fluorescence intensity at a time resolution of 100 ms per data point. Second, a quenching or de-quenching step was identified after the following conditions were met: $\frac{|I(t)-I(t-\Delta t)|}{I_{\max}} \geq T$ and $\frac{|I(t+\Delta t)-I(t-2\Delta t)|}{I_{\max}} \geq T$ and $\frac{|I(t+2\Delta t)-I(t-3\Delta t)|}{I_{\max}} \geq T$ and $\frac{|I(t+3\Delta t)-I(t-4\Delta t)|}{I_{\max}} \geq T$ and $\frac{|I(t+4\Delta t)-I(t-5\Delta t)|}{I_{\max}} \geq T$ where I(t) is the intensity at time t, Δt the time resolution (here 100 ms) and T the threshold (here T = 0.15 was chosen primarily due to noise). Finally, the relative size of the quenching or de-quenching step, Q, was extracted using the following equation:

$$Q = \frac{1}{5}\sum_{i=0}^{4}\frac{|I(t+i\Delta t)-I(t+(i+1)\Delta t)|}{I_{\max}}$$

Therefore, only step sizes at which the quenching or de-quenching event was longer than 0.5 s were considered.

5.3 RESULTS AND DISCUSSION

To examine the energy transport process in large-scale ordered morphologies, we have developed a SVA technique to control the average size and morphological order of aggregates. The aggregation process can be controlled by a careful choice of the type and ratio of solvents used for SVA in films consisting of highly diluted fluorescent CPs in non-fluorescent polymer matrices (Figure 5.1). We directly monitored the aggregation process in a model system comprised of single chains of a prototypical CP poly[2-methoxy-5-(2'-ethylhexyloxy)-1,4-phenylenevinylene] (MEH-PPV) embedded in a poly(methyl methacrylate) (PMMA) host matrix via SMS techniques (see chapter 3 for details). During SVA, a polymer film resides in a heterogenous mixture of solid and liquid-like phases in which single CP chains undergo diffusion.[131] This diffusion of single CP chains is utilized to generate aggregates. The steady state of the aggregation process, in terms of the size and number of aggregates, can be rationalized by Ostwald ripening. The minimum size of stable aggregates is predetermined by the critical radius, R_c, which is given by the following[132]:

$$R_C = \left(\frac{2\sigma}{kT}\right) v \frac{C_\infty}{C - C_\infty} \quad \text{for} \quad C > C_\infty \tag{5.1}$$

where σ is the inter-phase surface tension between the solute and the solvent, v is the atomic or molecular volume of the solute, C the solute concentration and C_∞ is the saturation limit of the solute concentration. In our case, the CP is the solute and we make a simplification for the solvent that the surrounding medium, which consists of both the swollen host-matrix along with the solvents used for annealing, is altogether considered as the solvent.

An elegant way to facilitate aggregation is to keep C constant and decrease C_∞ (see equation 5.1). This is possible by choosing a host-matrix-selective solvent for SVA. The miscibility of a polymer and solvent can be described according to Flory-Huggins

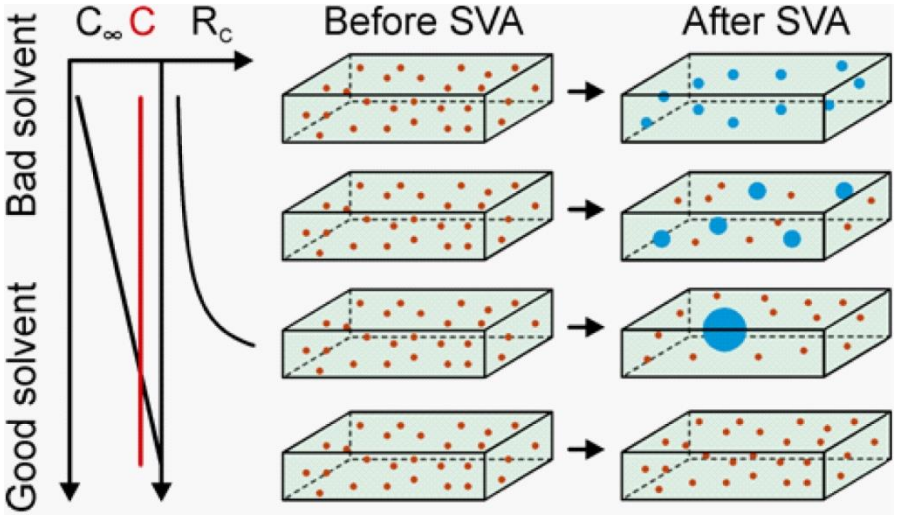

Figure 5.1: Controlled aggregation in highly diluted thin conjugated polymer/polymer films by solvent vapor annealing (SVA). An increase in the ratio of good/bad solvent increases the saturation limit, C_∞, of the conjugated polymer during SVA, whereas the overall conjugated polymer concentration, C, remains constant. The critical radius, R_C, which determines the minimum size of stable aggregates, increases until approaching infinity at $C_\infty > C$ (see equation 1). The evolution of a thin film is schematically illustrated upon SVA at different good/bad solvent ratios. The red dots represent single conjugated polymer chains, whereas the blue dots represent aggregates.

theory by the polymer-solvent interaction paramter χ. This parameter relates the difference of the enthalpy of interactions between polymers and solvents and the interactions of polymers and solvents with themselves. This difference is normalized to the temperature such that the polymer and solvent are completely miscible over the entire composition range when $\chi < 0.5$.[133] Therefore, a host-matrix-selective solvent, which will be referred to as a bad solvent, must have an interaction parameter $\chi < 0.5$ for the host matrix and $\chi > 0.5$ for the CP. Furthermore, C_∞ can be adjusted by mixing this solvent with a non-selective solvent for both phases, i.e., $\chi < 0.5$ for the host matrix and CP, which will be referred to as a good solvent. Figure 5.1 is a schematic representation of the expected evolution of a film at different good/bad-solvent vapor ratios, referred to as V_g/V_b. C_∞ will be small or even zero at a low V_g/V_b; therefore R_C is small, which will result in many small stable aggregates consisting of only a few chains (represented by the blue dots) and a low concentration of single CP chains (represented by the red dots). C_∞ will increase with increasing V_g/V_b, leading to an increase in R_C. This will produce fewer but larger aggregates as well as a higher single-CP-chain concentration. As C_∞ approaches C, R_C tends to infinity and no stable aggregates can be formed during SVA, resulting in a sample composed only of single CP chains as has already been observed for the SVA of MEH-PPV with toluene or chloroform.[131]

The wide-field fluorescence images in Figure 5.2 show how the MEH-PPV/PMMA thin films evolve after 30 minutes of SVA with different V_g/V_b, which clearly demonstrates the concept presented in Figure 5.1. Figure 5.2 on the left shows a sample before SVA with each fluorescent spot representing a single CP chain; the initial concentration of MEH-PPV was the same in each 200-nm-thick PMMA film illustrated in Figure 5.2. We chose chloroform and acetone as a good and bad solvent for MEH-PPV, respectively. Chloroform is a good solvent for both PMMA and MEH-PPV,[52]

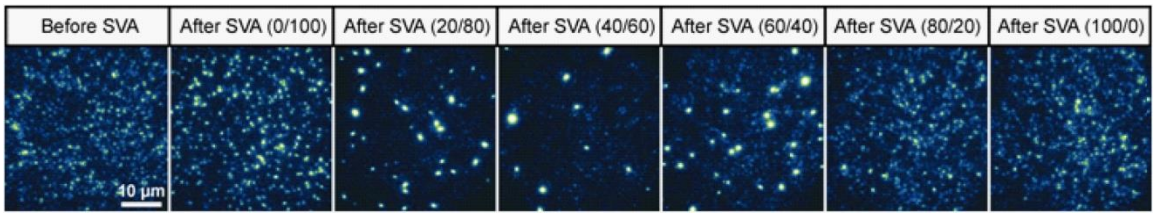

Figure 5.2: Wide-field fluorescence images of highly diluted MEH-PPV/PMMA thin films before and after undergoing different processing conditions. The chloroform/acetone ratio for 30 min SVA is denoted in parentheses above the images. The same MEH-PPV/PMMA concentrations were used for each sample. An excitation wavelength of 488 nm with an intensity of approximately 1.5 Wcm^{-2} was used, and the same z-scale was applied to all images.

whereas acetone is a bad solvent for MEH-PPV due to its polarity but is still a good solvent for PMMA.[134] A comparison of the film before and after 30 minutes of SVA (Figure 5.2) clearly demonstrates the formation of aggregates upon SVA as the number of fluorescent spots decreases and their intensity increases. As V_g/V_b increases, the aggregates grow in size, as indicated by the fact that there are fewer but brighter fluorescent spots. However, when V_g/V_b is excessively high, that is above 60/40, no stable aggregates can be formed as C_∞ becomes higher than C (Figure 5.2 on the right), which is further evidenced by the fast diffusion of dim fluorescent spots from single CP chains during SVA (Figure 5.3 on the right).

The dynamics during SVA were observed by time-resolved wide-field fluorescence microscopy at different vapor ratios of chloroform/acetone for SVA, V_g/V_b (Figure 5.3A-L). It can be seen how the diffusion dynamics of the aggregates change throughout the 30-minute-long SVA process. Small aggregates form at the beginning of SVA and grow upon further SVA until a steady state is reached. By comparing the movies acquired in the beginning of SVA (5-8 minutes) to the movies at the end (27-30 minutes), it can be clearly observed that the diffusion of the aggregates slows down with increasing size of the aggregates. This is also observed in the accumulated images of the movies (Figure 5.3A-L). Diffusing aggregates appear as elongated and blurred fluorescence spots that become spatially more confined at the end of SVA (Figure 5.3G-L) compared to the beginning of SVA (Figure 5.3A-F). This is especially clear for the lowest V_g/V_b value (0/100) at which almost no diffusion can be observed after 27 minutes of SVA. Furthermore, two different diffusion behaviors can be observed for high V_g/V_b: a fast diffusion of many dim particles and a slow diffusion of a few very bright particles. The former is attributed to the diffusion of single CP chains. As the solvent quality changes, the saturation limit, C_∞, increases, which allows individual chains to exist even

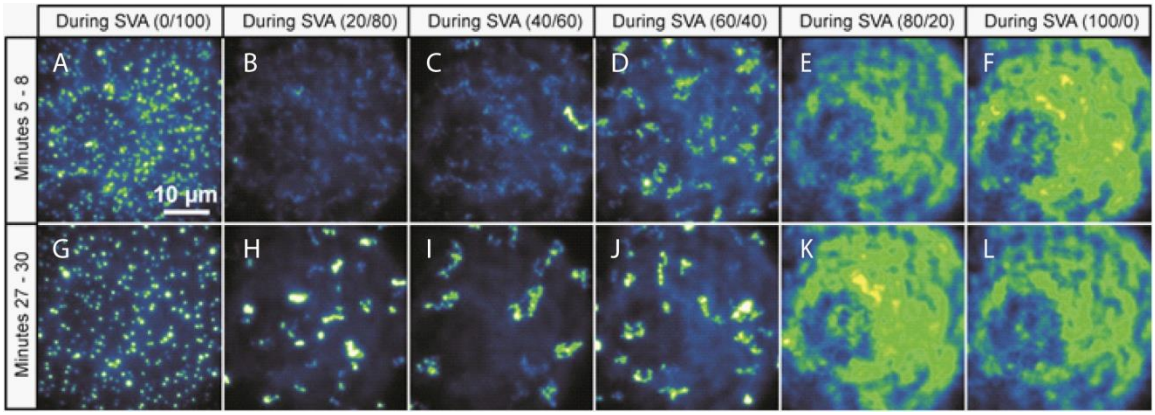

Figure 5.3: Wide-field fluorescence images of a PMMA film containing MEH-PPV accumulated over three minutes during solvent vapor annealing (SVA) at different timeframes and with different chloroform/acetone ratios (given in the parentheses). An excitation wavelength of 488 nm with an intensity of approximately 1.5 Wcm^{-2} was used.

after 30 minutes of SVA. The slow diffusion of the bright particles is related to the aggregates, which show an increase in brightness with ongoing SVA and a decrease in diffusion. Both are related to the growth of the aggregates. At a V_g/V_b > 80/20, only the fast diffusion of the single CP chains can be observed because the C_∞ of the environment becomes larger than the MEH-PPV concentration, *C,* and no stable aggregates can be formed. For concentrations at which aggregates are formed, it can be concluded that the swollen PMMA host matrix acts as a sieve for the aggregates and slows down the diffusion with increasing size of the aggregates; this prevents the aggregates from further agglomerating and ultimately precipitating. This can be seen by comparing the movies during SVA directly at the beginning of the SVA process (5-8 minutes) and at the end (27-30 minutes). The aggregates diffuse significantly slower at the end compared to the beginning, due to their increase in size, whereas the single CP chains diffuse always similar. As the solvent quality is enhanced, i.e., higher V_g/V_b ratio, the aggregates can diffuse more readily, indicating that the PMMA host-matrix is more swollen. This is likely the case because chloroform interacts more strongly with PMMA than does acetone.

By thresholding the intensity and counting the number of fluorescent spots, the number of single CP chains and aggregates can be quantified. Figure 5.4 shows the number of aggregates per imaging area (blue bars, Figure 5.4) and their fluorescence intensity (grey bars, Figure 5.4) measured from the samples shown in Figure 5.2 after SVA. An intensity threshold above the intensity of single CP chains was used to select only aggregates. The physical sizes of the aggregates are mainly below the diffraction limit, which makes particle analysis feasible. Figure 5.4 clearly demonstrates the growth of aggregates as their intensity increases and the number of particles decreases. At the

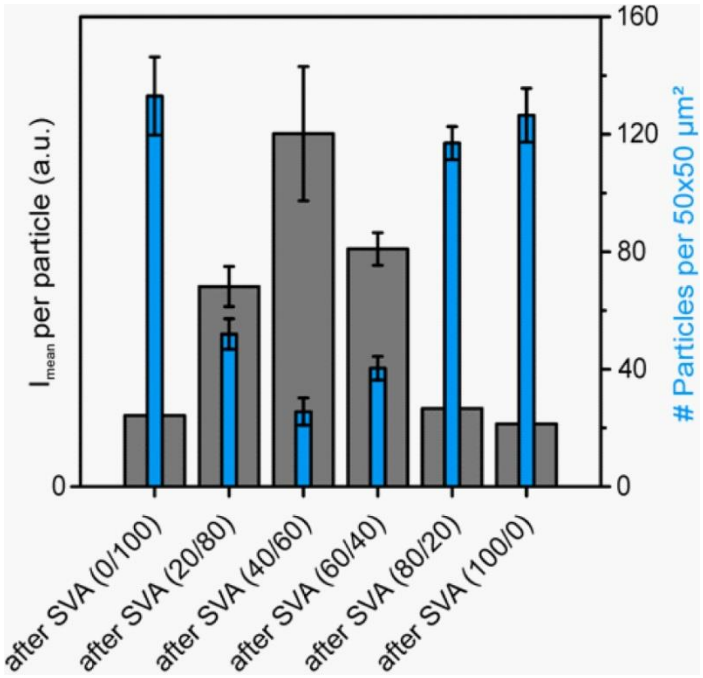

Figure 5.4: Bar graph of the number of aggregates (blue) per imaging area and their mean intensity, I_{mean} (grey), for six different SVA conditions. The chloroform/acetone ratio for 30 min SVA is denoted in parentheses. The mean and standard deviations were obtained by measuring five different areas of each sample.

initial MEH-PPV concentration (C = $5 \cdot 10^{-12}$ mol L^{-1}), the largest aggregates can be formed at a $V_g/V_b \approx 40/60$ using chloroform and acetone. The size of the aggregates decreases with a $V_g/V_b > 60/40$ as C_∞ becomes larger than C where equation 5.1 can no longer be applied, and the aggregates are no longer stable. By studying the evolution and diffusion behavior of the aggregates during SVA, it is shown that the swollen PMMA matrix acts like a sieve and restrains the diffusion of especially the aggregates, due to their increased size compared to single CP chains (Figure 5.3). The degree of swelling varies with V_g/V_b and prevents the aggregates from further agglomerating with themselves. It especially facilitates the formation of small aggregates at a low V_g/V_b.

The fluorescence intensity can be used to estimate the number of chains in aggregates. A comparison of the brightness of the MEH-PPV aggregates to the average number of chains incorporated in each aggregate required an estimation of the number of chains from the images collected before and after SVA. The average number of single chains per excitation area, $N_{SC,before}$, was measured before solvent vapor annealing (SVA) and compared to the average number of chains, $N_{SC,after}$, as well as the number of aggregates, $N_{A,after}$, after SVA. To discern between aggregates and single chains, a lower intensity threshold was used for the aggregates at which no fluorescent spots could be detected before SVA for this data set of 702 spots. Therefore, less than 0.14 % fluorescent spots were detected above this threshold before SVA. The same threshold was used as an upper threshold to count the number of single chains after SVA. The average number of chains per aggregate, $N_{SC\ per\ A}$, could be then estimated by

$$N_{SC\ per\ A} = \frac{N_{SC,before} - N_{SC,after}}{N_{A,after}} \tag{5.2}$$

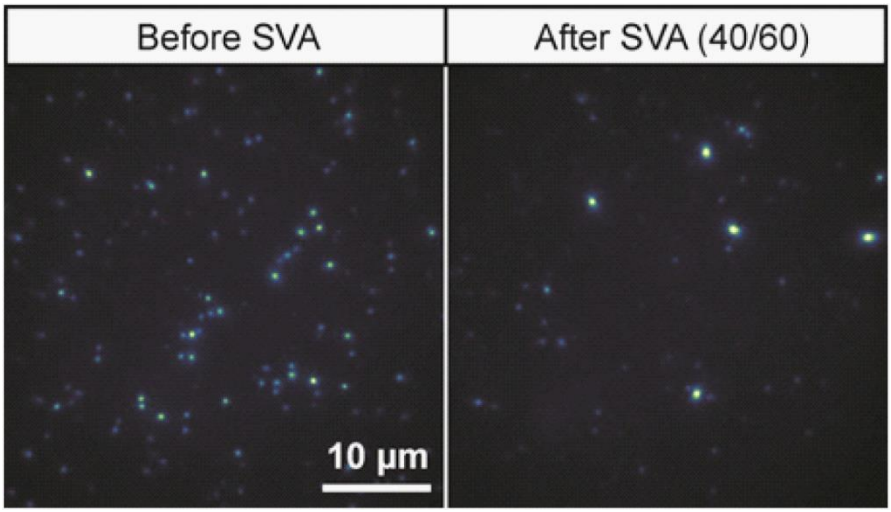

Figure 5.5: Wide-field fluorescence images of PMMA film containing MEH-PPV at single-molecule concentration after different processing conditions (Before SVA and same sample after 30 min of 40/60 chloroform/acetone SVA).

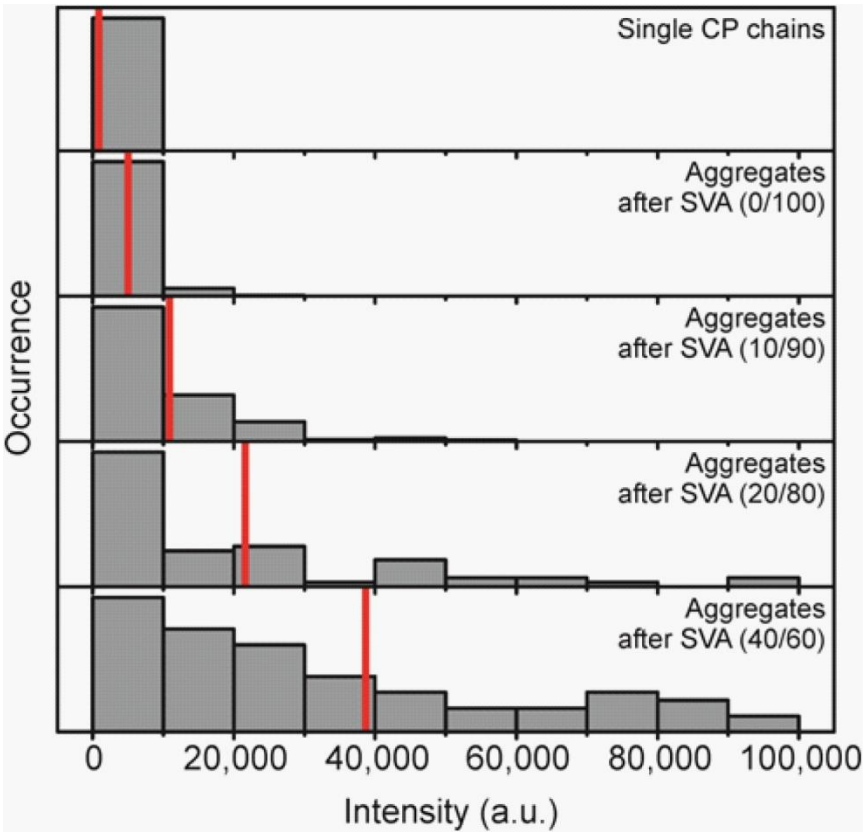

Figure 5.6: Experimental fluorescence intensity histograms for MEH-PPV particles under the same experimental conditions. The same MEH-PPV/PMMA concentrations were used for the aggregate samples, whereas a 50x-lower MEH-PPV concentration was used to study single CP chains. The chloroform/acetone vapor ratio for SVA is given in the parentheses. An intensity threshold slightly above the background was used for the single CP chains, whereas an intensity threshold above the maximum intensity of single MEH-PPV chains was applied to measure primarily aggregates. The red line represents the mean intensity for each sample.

By measuring five different areas from the sample shown in Figure 5.5, $N_{SC,before} = 140 \pm 14$, $N_{SC,after} = 70 \pm 13$ and $N_{A,after} = 5 \pm 1$ were measured by calculating the mean and standard deviation. This led to $N_{SC\ per\ A} = 14 \pm 5$. The mean intensity for the aggregates after SVA was measured to be $I_A = 14000 \pm 2200$, whereas the mean intensity for the single chains after SVA was measured to be $I_{SC} = 930 \pm 100$. From these calculations, it is clear that the intensity of the aggregates scales roughly with the number of incorporated chains. The mean intensity, I_{mean}, from the corresponding intensity histogram (Figure 5.6) is given for each sample.

Fluorescence excitation polarization spectroscopy was used to study the evolution of morphological order with an increasing number of CP chains in the aggregates. This spectroscopic technique has been used to probe the morphological order of multi-chromophoric systems by measuring the fluorescence intensity modulation while rotating the angle of linearly polarized excitation light in the *x*-*y* plane of the laboratory frame. The modulation depth, *M*, reflects the extent of alignment of chromophores within each single CP or aggregate[47]. For each single CP chain or aggregate, *M* was acquired and a histogram of a large number (150-200) of particles was obtained (Figure 5.7). The equilibrated conformation of single MEH-PPV chains is a highly ordered rod-like structure[100,131] as reproduced in Figure 5.7 (top histogram). The histogram shows high *M* values primarily above 0.5 with a peak around 0.8 and mean of 0.74 (Figure 5.7, red line). Further, Figure 5.7 shows the *M* histograms generated from the different sizes of aggregates. Surprisingly, as the aggregates grow in size, the *M* histograms show only a slight shift to lower values. Very similar distributions were observed until the mean intensity, I_{mean}, became ~25x higher than the I_{mean} of single CP chains (Figure 5.7). Only when the I_{mean} is ~45x higher than the I_{mean} of single CP chains do the *M* histograms of aggregates show a significant number of low *M* values with a mean value of 0.44 (Figure

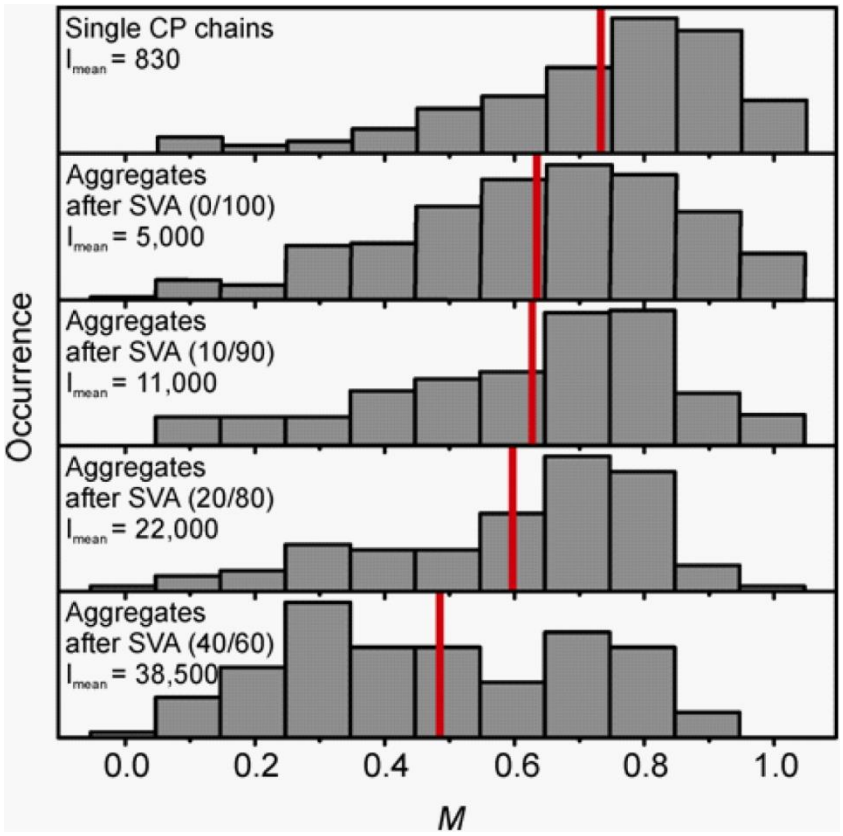

Figure 5.7: Experimental histograms of modulation depth, *M*, obtained by fluorescence excitation polarization spectroscopy. The red line represents the mean modulation depth. Single-molecule sample and aggregate sample were obtained after 30 min of SVA with chloroform/acetone vapor ratios as indicated in parentheses. An intensity threshold slightly above the background was used for the single CP chains sample, whereas an intensity threshold above the maximum intensity of single MEH-PPV chains was applied to measure primarily aggregates in the aggregate samples. The mean intensity, I_{mean}, of the particles is indicated to the left of each graph.

5.7). Nevertheless, a few high *M* values are still observed for these samples. Thus, the aggregates grow in a highly ordered fashion until they reach a size at which additional domains begin to form. These domains are not necessarily aligned with each other and lower the overall excitation anisotropy within an aggregate, as was observed for the largest formed aggregates (Figure 5.7).

Now, with aggregates of known size and chain order, we can utilize single-aggregate spectroscopy to probe energy transfer by examining how the aggregate fluorescence intensity changes with time as photochemical quenchers, such as radical cations[129], are randomly generated within the aggregate. For all of the aggregates, we observe the striking phenomenon of discrete fluorescence blinking that would be expected for single molecules or single CP chains (Figure 5.8a, b). Extraordinarily large jumps in fluorescence intensity, up to 33,000 counts (Figure 5.8b, red marker), can be observed, whereas the average fluorescence intensity of a single CP chain is only around 1,500-2,000 counts under the same experimental conditions (Figure 5.8a). This very simple but clear observation suggests that one quencher can quench up to several chains simultaneously and in this case, up to ~22 CP chains. This is a clear demonstration that a single photochemically generated quenching site can lower the quantum yield of neighboring CP chains as illustrated in the schematic drawing (Figure 5.8a and b, right). It was observed that energy transfer in single CP chains is manifested by strong blinking behavior[121,129]. Hence, we attribute the observed blinking behavior in highly ordered aggregates to the long-range energy transfer observed in single CP chains.

We further investigated the quenching depths of blinking events of aggregates of different sizes and compared them to those of single CP chains. As before, a single-CP-chain sample and samples containing aggregates of different sizes were prepared. These samples were investigated and compared via time-resolved wide-field fluorescence

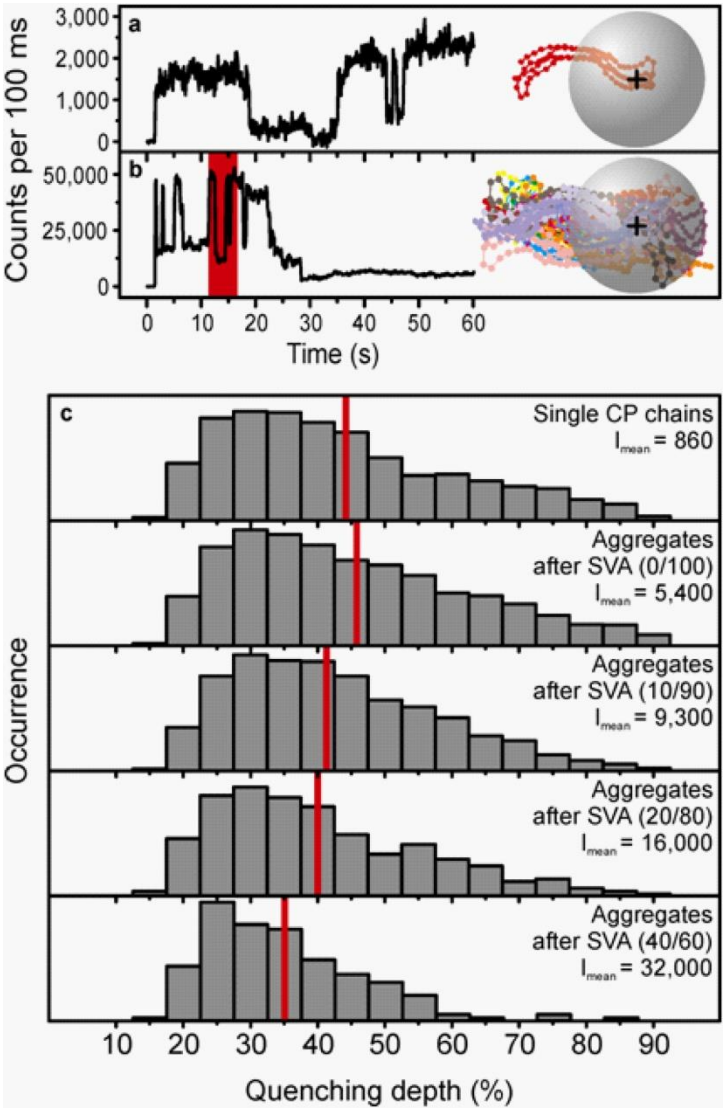

Figure 5.8: Representative single-particle fluorescence transients and quenching depth histograms. (a) A single MEH-PPV chain and (b) an MEH-PPV aggregate in a PMMA host matrix are shown under the same experimental conditions. The inset is a schematic representation of a single CP chain and an aggregate consisting of 25 CP chains with a fluorescence quencher. (c) Histograms of fluorescent quenching depths for different single MEH-PPV particles in an ensemble (see methods for the definition of a quenching event). The red line represents the mean quenching depth. The processing condition and the mean intensity, I_{mean}, of the particles is denoted in the upper right corner.

microscopy and were illuminated with a 10-fold increase in excitation intensity (15 Wcm^{-2}) compared to the previous measurements to induce a pronounced blinking behavior. For each particle, a fluorescent transient was extracted, as shown in Figure 5.8a, b. By using a self-written algorithm (see Experimental Section), the quenching depths from single-particle fluorescence transients were extracted and a large number (150-200) of particles were analyzed to generate a quenching depth histogram (Figure 5.8c). As can be seen, the mean quenching depth decreases slightly with increasing size of the aggregates. However, mean quenching depths of 40 % and 35 % can still be observed for aggregates with an $I_{mean} \approx$ 16,000 counts and 32,000 counts (Figure 5.8, red line), corresponding to aggregate sizes up to 19 and 37 CP chains, respectively. Even very large quenching depths above 70 % can be observed for a small subpopulation (5 % for aggregates with $I_{mean} \approx$ 16,000 and 2 % for aggregates with $I_{mean} \approx$ 32,000) of these largest aggregates.

To extract the minimum quenching radius necessary to explain the observed large quenching depths within the aggregates, lattice models with a fixed volume but different geometries were constructed by simulating multichromophore quenching via a Förster-type process. Within this theoretical model, the reasonable assumption is made that a blinking event is generated by one quencher due to the fact that blinking events appear as discrete events. This is the same type of simulation described in Chapter 4. Dimensions of 4 x 4 x 111 nm for individual chains (Figure 5.9A) were assumed by considering the fact that a single chain folds into an anisotropic rod conformation.[44,100] The average number of incorporated chains within an aggregate is estimated to be between 25 and 45 chains for the largest ordered domains based on fluorescence intensity and polarization modulation. The smallest volume of these ordered domains is estimated to be about 45,000 – 81,000

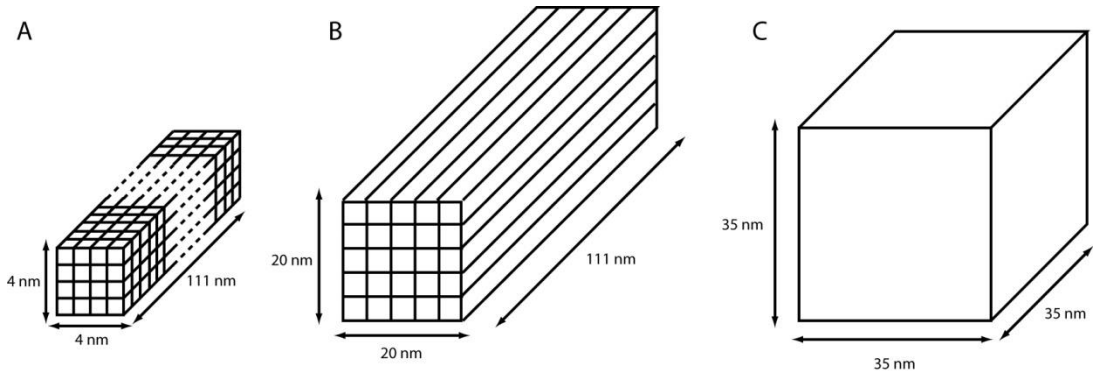

Figure 5.9: Molecular shape used for simulation. (A) Single polymer chain (4 x 4 x 111 nm). (B) Aggregates composed of 25 of the undeformed chains shown in (A). (C) Aggregates made up of 25 chains that are deformed to produce the minimum surface area of the aggregates.

nm^3 from the average molecular weight of the CP chains (M_n = 830 kDa) and the bulk density (0.8 g/ml). To prevent an overestimation of the energy transfer radius, we used the lower volume limit of 45,000 nm^3 corresponding to 25 single MEH-PPV chains. For self-assembled aggregates composed of 25 individual chains, we assumed two extreme cases of the aggregation process (Figure 5.9B and C). Figure 5.9B represents an anisotropic aggregate in which single chains are stacked on top of one another to form an aggregate with the smallest surface area possible without deforming the chains. This assumption is reasonable because individual chains are folded into rod conformations before acetone vapor annealing, and it is not likely that they can freely unfold during the annealing because acetone is a bad solvent for MEH-PPV. Figure 5.9C represents an aggregate composed of chains that deform to minimize the surface area of the aggregates as much as possible. This shape is the most isotropic, and one quencher can quench the fluorescence of these aggregates most effectively. The mean quenching depth for different quenching radii under two different geometries were simulated. The results from these simulations (Table 5.1) suggest a quenching radius of at least 25 – 30 nm for the anisotropic aggregate shape (Figure 5.9B) and 20 nm for the energetically less probable isotropic aggregate shape (Figure 5.9C), which corresponds to the 35 – 40 % average quenching depths illustrated in Figure 5.7 for aggregates with I_{mean} ≈ 16,000 and I_{mean} ≈ 32,000. Even a quenching radius of ~60 nm can be extracted for the subpopulation of observed large quenching depths above 70 % in the case of the anisotropic aggregate.

Although the single-step FRET model was used to estimate the energy transport scale within aggregates, it does not mean that the actual energy migration mechanism is the single-step FRET (see chapter 4 for discussion on energy migration mechanisms). Higher level of simulations is required to gain deeper insights of energy transport mechanism within these aggregates. Definitely, the isotropic energy transfer model does

R_0 (nm)	Mean quenching depth (%)		
	Single chain (4 x 4 x 111 nm)	Aggregate (20 x 20 x 111 nm)	Aggregate (35 x 35x 35 nm)
10	17	7	9
15	26	17	23
20	34	27	41
25	41	36	58
30	48	44	73
35	54	51	83
40	60	58	90
45	65	63	94
50	70	68	97
55	74	73	98
60	78	77	99

Table 5.1: Mean quenching depth for different sizes of MEH-PPV particles at different quenching radii R_0.

not perfectly reflect physical details due to the lack of considerations on the dipole alignment dependent parameters such as the refractive indices and the orientation factor κ^2. However, despite the fact that the details of the mechanism are not clear yet and only a simple model was used in this study, the simulation results shown here successfully demonstrated the length scale of energy transport by reproducing the experimental observations. These results clearly support the idea that the length scale of energy transfer in highly ordered conjugated polymer domains is extraordinary large, and it was demonstrated that this notion can be applied to larger domains that are composed of a number of chains.

5.4 CONCLUSION

Our results suggest an average energy transfer length that ranges from 25 – 30 nm up to 60 nm in bulk CP materials. In contrast, it has been previously shown that nanoparticles prepared by reprecipitation methods are disordered and do not show any fluorescence blinking behavior such as that observed in this study, which is an indication of very small energy transfer distances[135,136]. Furthermore, the energy transfer length in bulk (PPV)-based derivatives is only about 5 nm[115]. We believe the differences are due to the morphological order within these materials[44,135] and that the extraordinarily energy transfer is only present in highly ordered morphologies. This finding emphasizes the importance of the control of morphology and the use of bottom-up approaches to study CP properties, because ensemble characterization methods tend to be misleading due to the inherent complexity and heterogeneity of CP materials. The "bottom-up" approach conceived at the single-molecule level is now adapted to aggregates, so-called mesoscopic objects, by using SVA to control self-assembly. In conclusion, this work lays the foundation for a new field where the molecular-level and bulk-level understanding of conjugated polymers meet by presenting a unique approach to control CP aggregation

process and characterizing the opto-electronic properties of these self-assembled ordered aggregates. As the conditions of aggregation process are developed to grow even larger aggregates, additional characterization methods will be able to clarify properties such as the degree of crystallization or electrical mobility. As we observed extraordinarly long-range energy transport, other characterizations could show results that are also not found in traditonal bulk film studies. The aggregates could also extend their usefulness into fascinating applications such as electrically driven lasing in CP´s[137]. Finally, this method can be applied to study a broad variety of materials at the mesoscopic length scale, including homo-polymers as demonstrated here or block co-polymers, with which a large range of morphologies can be achieved[138-141].

Acknowledgement for co-author contributions:
I would like to thank Dr. Jan Vogelsang and Dr. Johanna Brazard for helping me performing the experiments, and Dr. Jan Vogelsang, Prof. David A. Vanden Bout and Prof. Paul F. Barbara for helping me designing the experiments.

Chapter 6: Regioregularity and Single Polythiophene Chain Conformation

This chapter was reproduced in part from: Adachi, T.; Brazard, J.; Ono, R. J.; Hanson, B.; Traub, M. C.; Wu, Z. Q.; Li, Z. C.; Bolinger, J. C.; Ganesan, V.; Bielawski, C. W.; Bout, D. A. V.; Barbara, P. F. *J. Phys. Chem. Lett.* **2011**, *2*, 1400-1404 and Adachi, T.; Brazard, J.; Ono, R.; Bielawski, C.; Vanden Bout, D. *Proc. SPIE* **2011**, *8098*, 80980F.

6.1 INTRODUCTION

The function of conjugated polymer-based devices (*e.g.*, light-emitting diodes, field-effect transistors, and photovoltaic devices) is critically affected by the morphology adopted by the polymeric material.[12,19,142-144] One of the critical factors in determining bulk polymer morphology is the role of side-chains.[145-147] It has been shown that the regioregularity of polymer chains (*i.e.*, the percentage of head-to-tail linkages between monomer units in the polymer backbone) affects both film morphologies and their properties.[31,148-152] While understanding fundamental polymer chain interactions within such morphologies is essential to optimizing and tailoring the performance of such systems, large scale heterogeneity and complexity[39,73] are a major obstacles to studying these issues in thin films, as bulk methods characterize only average properties. In contrast, single polymer chain studies allow the distribution of properties to be directly studied by probing the system one chain at a time.[40-42] The combination of single molecule spectroscopy and theoretical simulation in particular is powerful in understanding the mechanism of chain folding and its effect on the optoelectronic properties of conjugated polymers.[45-47,100,153] However, it remains unclear how regioregularity affects the conformation of isolated individual chains where interchain interactions are absent. Scanning tunneling microscopy (STM) studies on single

conjugated polymer chains have shown nearly identical extended rigid structures for both regioregular and regiorandom polymers.[154] In contrast, other STM studies of monolayers reveal that single regioregular chains adopt highly folded conformations.[155,156] From a theoretical perspective, many studies on single conjugated polymer chains conformation utilize simple bead-on-a-chain models that completely ignore side-chains. However, a recent report[157] defining the minimum size requirement for the proper simulation of oligothiophenes shows that side-chains are important in determining the dihedral torsion angle between thiophene rings, suggesting that side-chains could play a significant role in chain conformations even at the single chain level.

In this chapter, we have focused on understanding the role of side-chains on single poly(3-hexylthiophene) (P3HT) chain folding mechanisms. We performed single molecule fluorescence excitation polarization spectroscopy on isolated chains of both regioregular (*rr*-) and regiorandom (*rra*-) P3HT in PMMA host matrix to directly examine the effect of regioregularity on single P3HT chain conformations at room temperature. This technique has been used to probe the morphological order (*i.e.*, nematic-like parallel chain order) of single conjugated polymer chains, and addressed various contributions to the mechanism of single polymer chain folding.[47,76,100] Most importantly, a recent report has shown that the conformations measured for single chains in a PMMA matrix are very close to the equilibrated conformations.[131] Finally, molecular dynamics simulations on atomistic models of *rr*- and *rra*-P3HT chains were performed for comparison with the experimental results.

6.2 EXPERIMENTAL SECTION

6.2.1 General Procedure for Polymer Synthesis

All solvents were purchased from Thermo Fisher Scientific Inc. and used without further purification unless otherwise noted. All other chemicals were purchased from Sigma Aldrich Co., Alfa Aesar, or Thermo Fisher Scientific Inc., and were used as received. THF was dried over 3 Å molecular sieves and deoxygenated using a Vacuum Atmospheres Company solvent purification system. 2,5-Dibromo-3-hexylthiophene was prepared according to literature procedures.[158] All manipulations were performed under nitrogen using standard Schlenk techniques. ^{1}H NMR spectra were recorded using a Varian 400 or 500 MHz spectrometer. Chemical shifts are reported in delta (δ) units and expressed in parts per million (ppm) downfield from tetramethylsilane using the residual non-deuterated solvent as an internal standard. For ^{1}H NMR: $CDCl_3$, 7.24 ppm. Gel permeation chromatography (GPC) was performed at 40°C on a GPCmax VE-2001 (Viscotek) equipped with solvent and sample delivery module, and three fluorinated polystyrene columns (IMBHW-3078 and I-MBMMW-3078 and I-MBLMW-3078) arranged in series, and a UV-Vis photodiode array detector tuned at 450 nm. Number average molecular weight (M_n) and polydispersity indice (PDI) are reported relative to polystyrene standards in tetrahydrofuran (THF) stabilized with butylated hydroxytoluene (BHT). Absorption spectra were measured using 8453 UV-visible spectroscopy system (Agilent Technologie Inc.). Fluorescence spectra were measured using Varian Cary Eclipse fluorescence spectrophotometer (Agilent Technologie Inc.).

6.2.2 Synthesis of regioregular P3HT

Regioregular P3HT of varying molecular weights was synthesized according to literature procedures[158] by adjusting the initial monomer to catalyst mole ratios. In a typical polymerization, a 50 mL oven-dried Schlenk flask was charged with 2,5-dibromo-

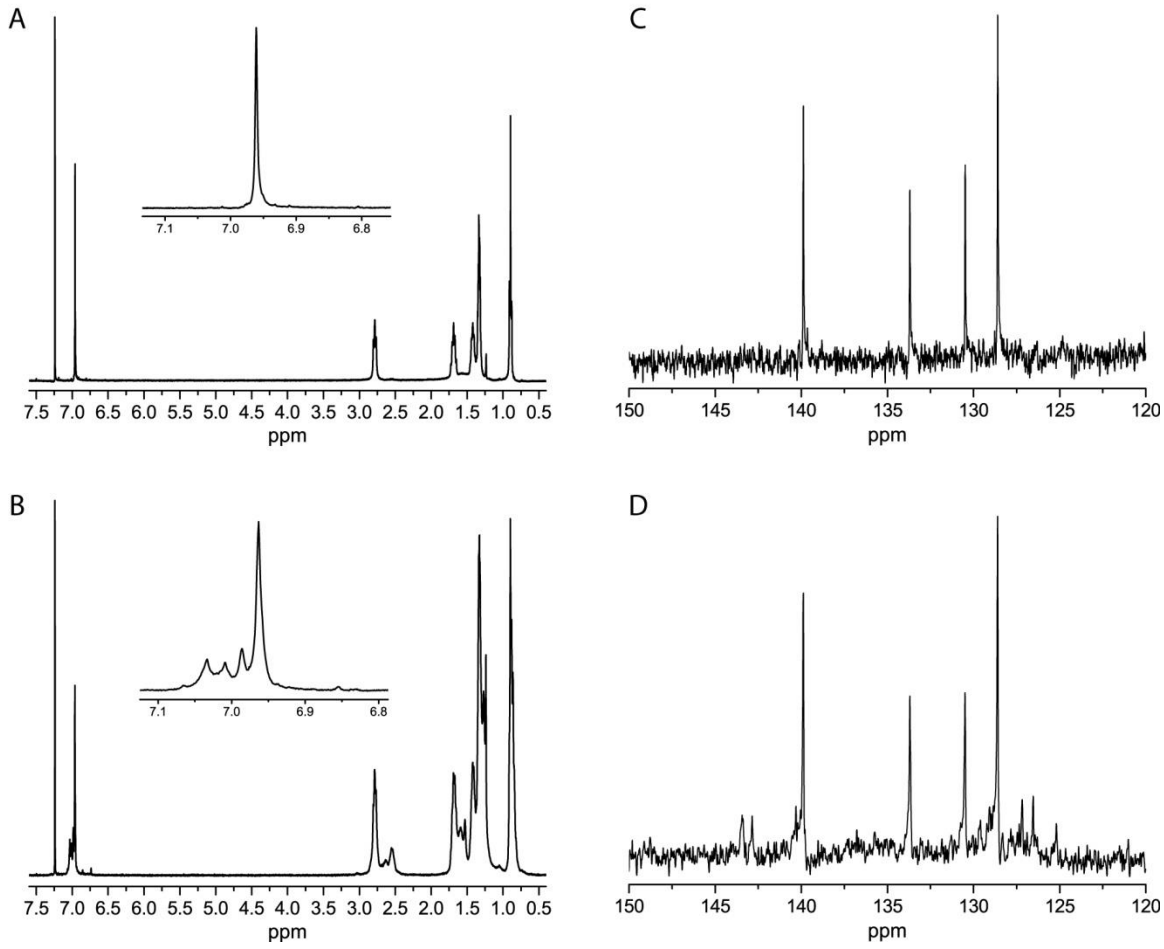

Figure 6.1: ^{1}H NMR spectra of (A) *rr*-P3HT (HT linkage of 97 %) and (B) *rra*-P3HT (HT linkage of 64%) and ^{13}C NMR spectra of the aromatic region of (C) *rr*-P3HT and (D) *rra*-P3HT. The insets in A and B show a spectra zoomed in around 7 ppm.

3-hexylthiophene (0.295 g, 0.90 mmol), dry THF (8.0 mL), and a stir bar. After 10 minutes of stirring at ambient temperature, isopropylmagnesium chloride (0.45 mL, 2.0 mol L^{-1} solution in THF) was added, and the resulting mixture was stirred at ambient temperature for 2 h. Ni(dppp)Cl_2 (1.9 mg, 0.0035 mmol) (dppp = 1,3-bis(diphenylphosphino)propane) was then added to the reaction mixture to initiate the polymerization. The progress of the reaction was monitored by GPC until the desired molecular weight was reached. The polymerization was quenched by the addition of a 5 mol L^{-1} HCl (aq.)/methanol mixture (5 mL). The precipitated solids were then collected in a Soxhlet thimble, and subjected to successive Soxhlet extractions with methanol, hexanes, and then chloroform. The pure polymer was isolated from the chloroform fraction (110 mg; 73% yield). GPC: M_n = 57 kDa, M_w/M_n = 1.09. ^{1}H NMR ($CDCl_3$, 400 MHz): δ 6.97 (s, 1H), 2.79 (t, 2H), 1.69 (m, 2H), 1.41 (br, 2H), 1.33 (m, 4H), 0.90 (t, 3H). ^{13}C NMR ($CDCl_3$, 150 MHz): δ 139.9, 133.7, 130.5, 128.6, 31.7, 30.5, 29.5, 22.6, 14.1 (Figure 6.1A).

6.2.3 Synthesis of regiorandom P3HT

Following a modified literature procedure[159] a 100 mL oven-dried two-neck flask was charged with anhydrous iron chloride ($FeCl_3$, 2.7 g, 16.4 mmol), dry chloroform (50 mL), and a stir bar. After stirring 15 minutes at room temperature, a THF solution of 3-hexylthiophene (0.8 g, 4.7 mmol in 10 mL THF) was added in one portion, and the reaction mixture stirred at room temperature for 4 h. The polymerization was quenched by the addition of NH_4OH (aq.) (15 mL). Unreacted monomer was separated from polymeric materials by precipitation from methanol, and collecting the precipitated solids by filtration. The crude polymer was then dissolved in 30 mL of chloroform, and further washed with NH_4OH (aq.) (2 x 30 mL), water (2 x 50 mL), and brine (50 mL), and dried over Na_2SO_4. Following removal of the solvent *en vacuo*, the polymer was dissolved in

10 mL of THF and filtered five times through neutral alumina to remove any traces of metal impurities. Concentration of the filtrate gave the pure polymer as a purple solid (0.38 g; 48% yield). Samples of varying molecular weights and narrow polydispersities were isolated by fractionation of this polymer by GPC. GPC: M_n = 129 kDa, M_w/M_n = 5.40. ^{1}H NMR ($CDCl_3$, 400 MHz): δ 7.07 (s), 7.03 (s), 7.01 (s), 6.99 (s), 6.97 (s), 2.79 (t), 2.64 (br), 2.55(br), 1.69 (br), 1.59 (br), 1.52 (br), 1.42 (br), 1.33–1.24 (br), 0.89 (br m). ^{13}C NMR ($CDCl_3$, 150 MHz): δ 143.4, 142.8, 139.9, 133.7, 130.5, 128.6, 127.2, 126.5, 31.7, 30.5, 29.5, 29.2, 22.6, 14.1 (Figure 6.1B).

6.2.4 Wide-field single molecule fluorescence excitation polarization spectroscopy

Single molecule fluorescence excitation polarization spectroscopy[47,100] was used to probe single chain conformation of *rr*- and *rra*-P3HT. Details of sample preparation and experimental setups were described elsewhere[100] and briefly shown in Figure 6.2. A wide-field fluorescence polarization apparatus was built based on an inverted microscope (Zeiss, Axiovert 200) with an NA 1.25 objective lens (Zeiss, Achrostigmat, 100×). Wide-field fluorescence detection was performed using EMCCD detector (Andor, model iXon$^+$ DU-897E). Multiple excitation sources (458, 488, 514 nm) were obtained from an Ar ion laser (Melles Griot, model 35 LAL-030-206) by separating individual line using a prism. To rotate a linearly polarized beam around the axis of propagation, electro-optical modulator (EOM, Fastpulse technology, model 3079-4), a voltage amplifier (Trek, model 601-1), and a programmable function generator (Wavetek, model 29A) were used as a method previously described.[82] The optimum voltage applied to EOM was slightly varied for each wavelength. The polarization ratio was larger than 15:1 at all angles of rotation. The excitation area was ~40 μm at full width at half maximum (FWHM) and the estimated excitation power was ~1 W/cm^2. Isolated single P3HT chains embedded in poly(methyl methacrylate) (PMMA) were obtained by spin-coating very low

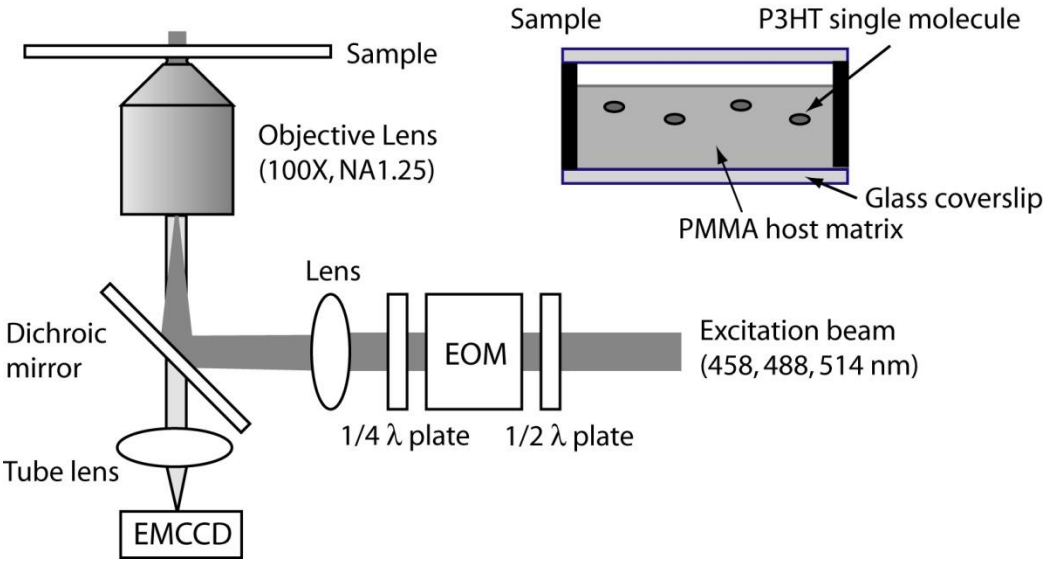

Figure 6.2: Schematic representation of single molecule wide-field fluorescence excitation polarization spectroscopy setup and the sample configuration.

concentration of P3HT in PMMA/Toluene solution. 15~20 individual molecules per image were monitored in the field of view (50×50 μm) of EMCCD. To avoid photooxidation during measurements, all the samples were prepared and sealed using an epoxy resin and a glass coverslip in a nitrogen filled glovebox. As expected, the fluorescence background level increased as the excitation wavelength was shifted to shorter wavelengths. The fluorescence intensity of individual spot was recorded while a linearly polarized excitation beam was rotated in the *x*-*y* lab frame. Fluorescence intensity trace as a function of a polarization angle, θ, was synchronously averaged over many cycles to increase a signal-to-noise ratio and each trace was fitted to the equation 6.1 to calculate the modulation depth, *M*, values.

$$I(\theta) \propto 1 + M \cos 2(\theta - \phi) \tag{6.1}$$

where ϕ is the angle of maximum absorption. As conjugated polymers are a multi-chromophoric system, an *M* value can be used to probe the alignment of individual chromophores (i.e. morphological order). The value of *M* approaches zero as more chromophores are randomly oriented, while it approaches one as more chromophores are aligned each other. To sample all the possible conformation and orientation of polymer chains, *M* values from hundreds of chains were measured and *M* histograms were constructed.

6.2.5 Molecular dynamics simulation methodology

Fully atomistic MD simulations were performed for single *rr*- and *rra*-P3HT chains of 120 repeat units utilizing the MD simulation package LAMMPS.[160] Simulation and molecular parameters (Lennard-Jones, nonbonded interactions, partial charges, bonds, angles, dihedrals, and out of plane angles) were adapted from previous work by Moreno *et al.*.[161] Parameters were validated by comparison with X-ray crystallography. All simulations employed the Langevin thermostat[162] coupled with a constant volume and

energy (microcanonical ensemble) time integration. Parallel tempering[163] with a temperature range of 350 – 750 K was used to accelerate chain collapse. Systems were simulated using a timestep of 0.1 fs, and all systems were simulated for a minimum of 5 ns.

6.3 Results and Discussion

Figure 6.3 shows the absorption and emission spectra of the synthesized *rr*-P3HT and *rra*-P3HT (samples before GPC fractionation) in chloroform. The absorption peak of the *rr*-P3HT samples occur at 454 nm while *rra*-P3HT absorbance is blue shifted with a peak at 420 nm. The fluorescence spectra (λ_{ex} = 488 nm) show that the fluorescence maxima of *rr*-P3HT and *rra*-P3HT occur at 577 nm and 572 nm, respectively. Similar results have been previously reported,[164-166] where the blue-shift of regiorandom polymers was attributed to the decrease of the effective conjugation length that results from the twisting of polymer chains due to repulsive interactions between two alkyl chains and a sulfur lone pair.[164] Taken in concert with their NMR spectra, these results verify that *rr*- and *rra*-P3HT were successfully synthesized.

Figures 6.4A and B show *M* histograms of *rr*- (M_n = 148 kDa) and *rra*-P3HT (M_n = 191 kDa), respectively. The two samples are clearly quite different from one another. The *M* histogram of *rr*-P3HT is highly peaked at 0.75 and the majority of molecules show high *M* values (> 0.5) indicating substantial alignment of the chromophores in *rr*-P3HT chains. The mean of the histogram is 0.63. In contrast, the *M* histogram of *rra*-P3HT is broad and lacking of any discernible features with a mean that is only 0.46. For both samples, ϕ values are randomly distributed at all angles for the ensemble of chains as expected from the random spin coating process. Although an *M* histogram is not a perfect representation of an inherent molecular anisotropy (*A*) histogram because the

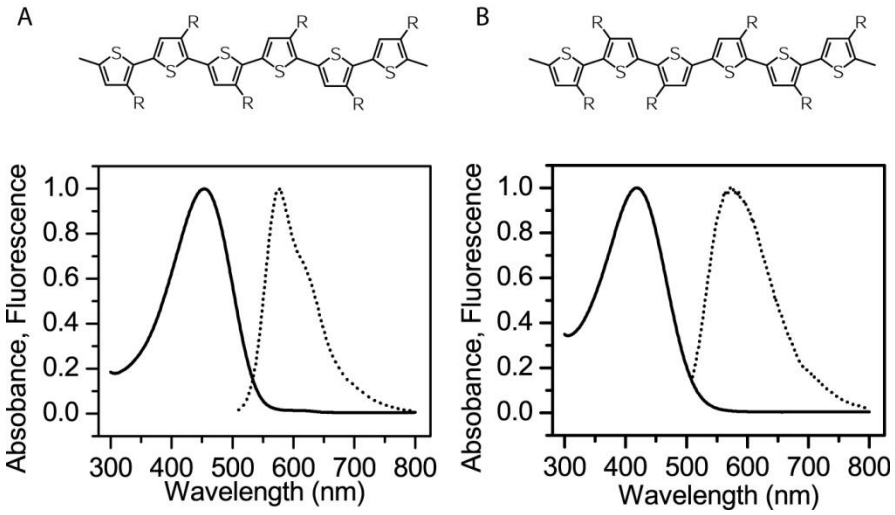

Figure 6.3: Absorption and fluorescence spectrum of (A) *rr*-P3HT and (B) *rra*-P3HT in chloroform. Chemical structure is shown above the spectra.

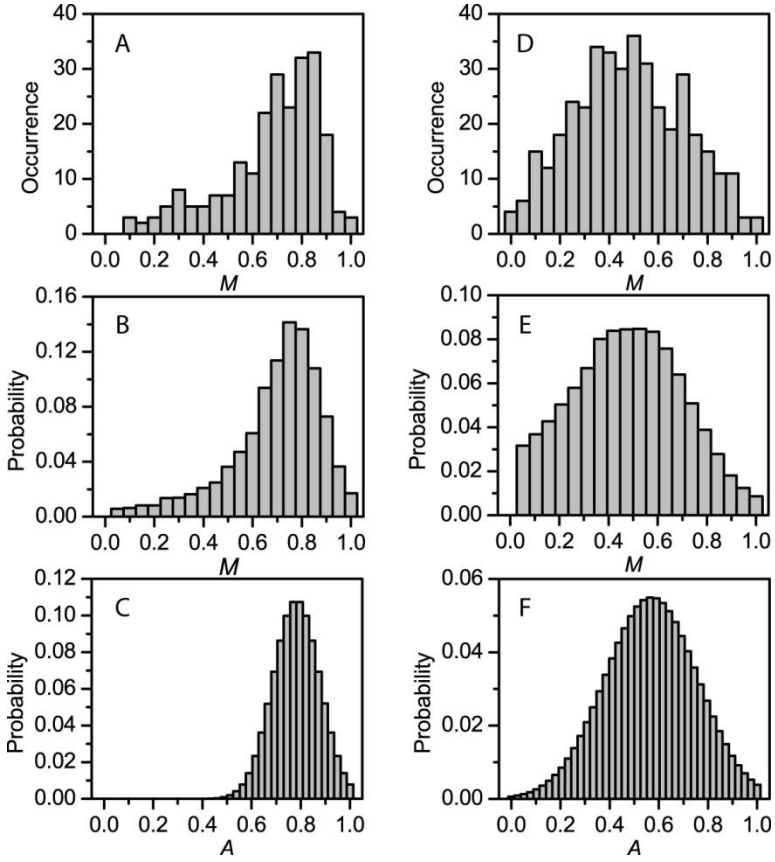

Figure 6.4: (A) Experimental modulation depth, *M*, histogram from 234 single *rr*-P3HT molecules measured at a 488 nm excitation. (B) Best fit histogram for the data shown in (A), calculated by a least-squares fitting procedure. (C) Anisotropy, *A*, distribution resolved by the best fit which generated the data shown in (B). (D) Experimental modulation depth, *M*, histogram from 398 single *rra*-P3HT molecules measured at a 488 nm excitation. (E) Best fit histogram for the data shown in (D), calculated by a least-squares fitting procedure. (F) Anisotropy, *A*, distribution resolved by the best fit which generated the data shown in (E).

value of *M* is a projection of absorption tensor on the x–y plane as described above, a molecular anisotropy (*A*) histogram can be extracted by using a model that takes the random distribution of molecular tilt angles and the polarization distortion effect of high numerical aperture microscope objective into consideration (see Chapter 2).[100] The best fit *M* histogram (Figure 6.4B, E) for the experimental results was calculated by using a least square fitting procedure, and the *A* histogram which gave the best fit *M* histograms are shown as Figure 6.4C and F for *rr*- and *rra*-P3HT, respectively. The *M* histogram of *rr*-P3HT was well-described by an empirical Gaussian *A* distribution with the mean of 0.78 and the standard deviation of 0.11. The *M* histogram of *rra*-P3HT was described by the *A* distribution with the mean of 0.57 and the standard deviation of 0.22. The quality of the fit for the *M* histogram of *rra*-P3HT was not as good as that of *rr*-P3HT because of its broadness and lack of distinct features, but it is sufficient enough to show that the *A* histogram of *rra*-P3HT has a broader distribution centered around a lower peak value than that of *rr*-P3HT.

Additionally, modulation depth studies were carried out on lower molecular weight ensembles for both polymers. Figures 6.5C and D show the *M* histograms of the lower molecular weight samples (*rr*-P3HT M_n = 35 kDa and *rra*-P3HT M_n = 45 kDa, respectively). Neither *rr*- nor *rra*-P3HT show any significant difference from the histograms measured for the higher molecular weight samples (Figure 6.4). The high anisotropy value and narrow distribution for the *rr*-P3HT clearly indicate that every single *rr*-P3HT chain folds into a highly ordered conformation while single *rra*-P3HT chains can assume a wide variety of conformations, as represented by both broad *M* and *A* histograms.

Based on the above results we conclude that the uniform head-to-tail (HT) linkages in *rr*-P3HT allow for the regular packing of a chain into a highly anisotropic

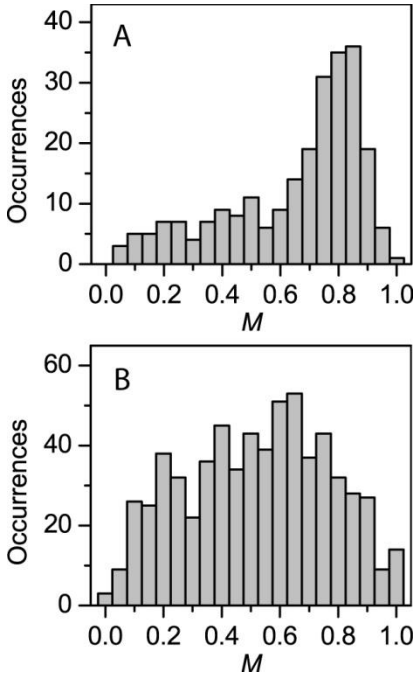

Figure 6.5: The experimental *M* histograms of (A) *rr*-P3HT (M_n = 35 kDa, PDI = 1.45) 242 molecules and (B) *rra*-P3HT (M_n = 45 kDa, PDI = 1.10) 646 molecules.

conformation. In contrast, as indicated by the significant number of low *M* values in the histogram of *rra*-P3HT, the non-HT linkages presumably twist the polymer backbone and disturb the order of a chain. We note that the histograms for *rra*-P3HT also include a number of anisotropic molecules in ensemble. These are not the result of a subset of lower molecular weight chains or the distribution would shift to higher values for the lower molecular weight sample. Instead, we speculate that the overall morphological effect of non-HT linkages for each chain is not identical due to possible variations of non-HT linkages along each chain. As a result, a wide range of chain conformations are possible for *rra*-P3HT ranging from unordered, isotropic arrangements of chromophores to others that are highly anisotropic.

The same type of measurements and analysis were performed at three different wavelengths. Figure 6.6 shows the *M* and *A* histograms of *rr*-P3HT measured at 458 nm (Figure 6.6A, D), 488 nm (Figure 6.6B, E) and 514 nm (Figure 6.6C, F), and Figure 6.7 shows those of *rra*-P3HT at 458 nm (Figure 6.7A, D), 488 nm (Figure 6.7B, E) and 514 nm (Figure 6.7C, F). The mean and the standard deviation of each histogram are summarized in Table 6.1. A general trend observed for both *rr*- and *rra*-P3HT is that the mean of *M* and *A* histograms increases as the excitation wavelength is shifted from 458 to 514 nm. It is well known that conjugated polymers are a multi-chromophoric system and there is a distribution of the conjugation length of chromophores. The results that the anisotropy of both *rr*- and *rra*-P3HT chains increases at the redder excitation suggest that the conjugation length of chromophores for highly ordered regions within a chain is longer than that for disordered regions. This is presumably due to a pi-pi stacking which not only stabilizes highly ordered chain packing but also extends the conjugation length of chromophores. Although there is a wavelength dependence on the observed anisotropy, the clear difference between *rr*- and *rra*-P3HT can be observed at all

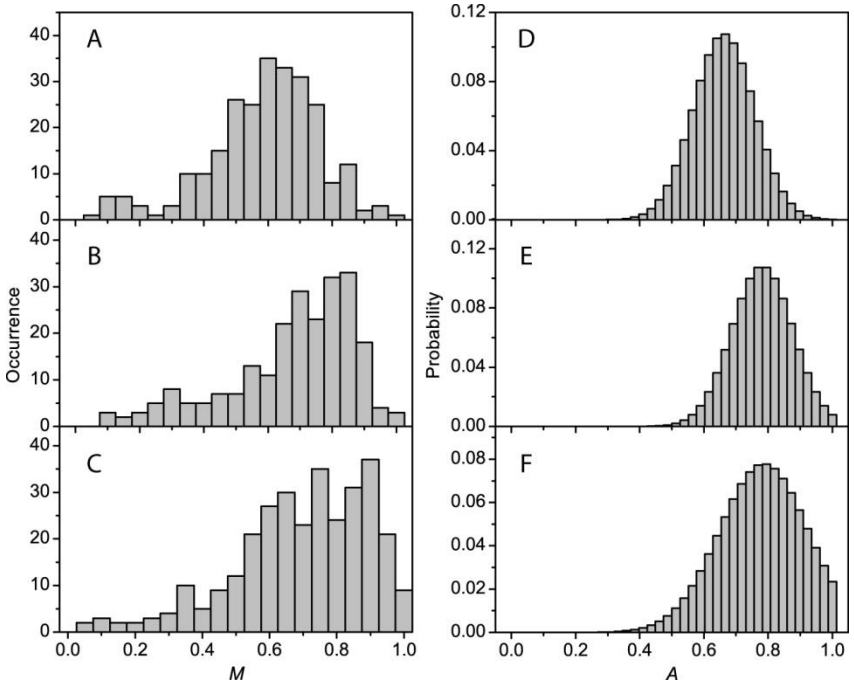

Figure 6.6: The modulation depth, *M*, histograms and corresponding anisotropy, *A*, distribution of *rr*-P3HT at different excitation wavelength. (A) and (D) at 458 nm excitation, (B) and (E) at 488 nm excitation, and (C) and (F) at 514 nm excitation.

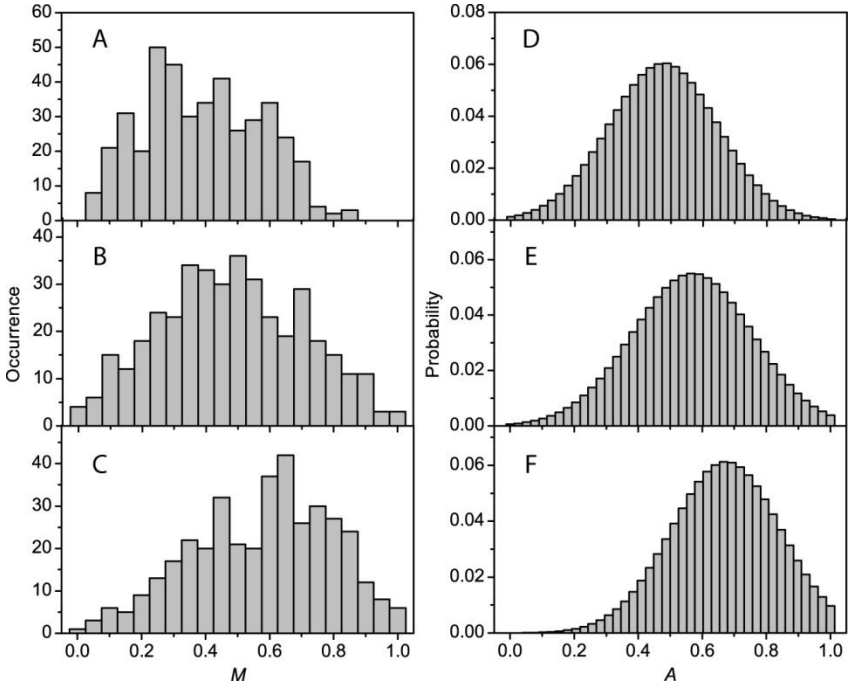

Figure 6.7: The modulation depth, *M*, histograms and corresponding anisotropy, *A*, distribution of *rra*-P3HT at different excitation wavelength. (A) and (D) at 458 nm excitation, (B) and (E) at 488 nm excitation, and (C) and (F) at 514 nm excitation.

wavelengths. The *A* histogram of *rr*-P3HT chains shows higher peak and narrower distribution than that of *rra*-P3HT at all the wavelengths. These results further strongly support the proposed idea that regioregularity is an important factor which governs single P3HT chain conformation. As the effect of regioregularity is observed at all excitation wavelengths, the previously reported differences between *rr*- and *rra*-P3HT at 488 nm were not due to an experimental artifact such as photoselection possibly caused by the use of a monochromatic laser line for probing chromophores, but reflected the conformational differences.

Based on the fluorescence intensity of *rr*- and *rra*-P3HT observed at each wavelength, we can roughly discuss the absorption spectrum of single chains. In chloroform, *rra*-P3HT has peak absorption at 420 nm and *rr*-P3HT at 453 nm. It is known that the absorption spectrum of P3HT shifts to longer wavelength from solution to bulk films due to more pronounced interchain interactions in bulk films.[152] Moreover, the spectral shape and peak position of absorption can be sensitively varied depending on polymer film morphologies.[152] It is yet not clear if the absorption spectrum of single chains in PMMA host matrix is similar to solution or bulk films as there has been no report on the absorption or the excitation spectrum of single P3HT chains. For *rr*-P3HT, the lowest fluorescence intensity is observed at 458 nm excitation and the intensity increases towards 514 nm. This indicates that there is some degree of red-shift in the absorption spectrum of single *rr*-P3HT chains from its solution phase. In contrast, for *rra*-P3HT, the lowest fluorescence intensity is observed at 514 nm and similar intensities are observed at 458 and 488 nm. These results are not sufficient to determine where the absorption peak of both compounds is, but they demonstrate that 514 nm is clearly on the red edge of the *rra*-P3HT sample, while it is closer to the peak of the *rr*-P3HT sample. These results indicate that the majority of conjugation length of chromophores within

Materials	λ_{exc} (nm)	Modulation depth		Fit	
		Mean	Std	Mean	Std
rr-P3HT	458	0.59	0.18	0.65	0.11
	488	0.68	0.20	0.78	0.11
	514	0.70	0.20	0.79	0.16
rra-P3HT	458	0.39	0.18	0.48	0.20
	488	0.48	0.22	0.57	0.22
	514	0.58	0.22	0.67	0.20

Table 6.1: Modulation depth and the best fit parameters by Gaussian function for *rr*- and *rra*-P3HT at different excitation wavelength

single *rr*-P3HT chains is longer than that in *rra*-P3HT. Along with *M* and *A* histograms at different wavelengths, qualitatively, we conclude that the distribution of the conjugation length which constructs the absorption spectrum is strongly correlated with the morphological order of each chain.

The absorption or the excitation spectrum of single P3HT chains will be very useful data to understand how the interactions within each chain affect the opto-electronic property. Based on our observations, the conjugation length of chromophores increases as the morphological order of a chain gets higher and therefore the absorption spectrum is most likely more shifted to lower energy. The spectral shift of P3HT is strongly correlated with the morphological order of a chain presumably because of the significance of pi-pi stacking within a chain. It could be even possible to more quantitatively characterize the correlation between the strength of interactions within each chain and its morphological order if the absorption or excitation spectrum of single P3HT chains is combined with our results presented here.

To gain insight into the above observations, we carried out molecular dynamics simulations on atomistic models of *rr*- and *rra*-P3HT chains. To this end, we considered two distinct single chains that were 30 monomers in length. In one case, the sequence of the chains was set to mimic the regioregular chain consisting of 97% HT linkages, while in the second case the regiorandom chain was modeled containing only 64% HT pairs. The chains were initially in a stretched conformation and were allowed to freely collapse. Parallel tempering[163] and an implicit solvent annealing using a Langevin thermostat[162] were used to accelerate the collapsing process and structure formation. The effect of regioregularity on the P3HT polymer chain conformations is clearly manifested in the collapsed conformations displayed in Figure 6.8 and 6.9. Examination of the regioregular

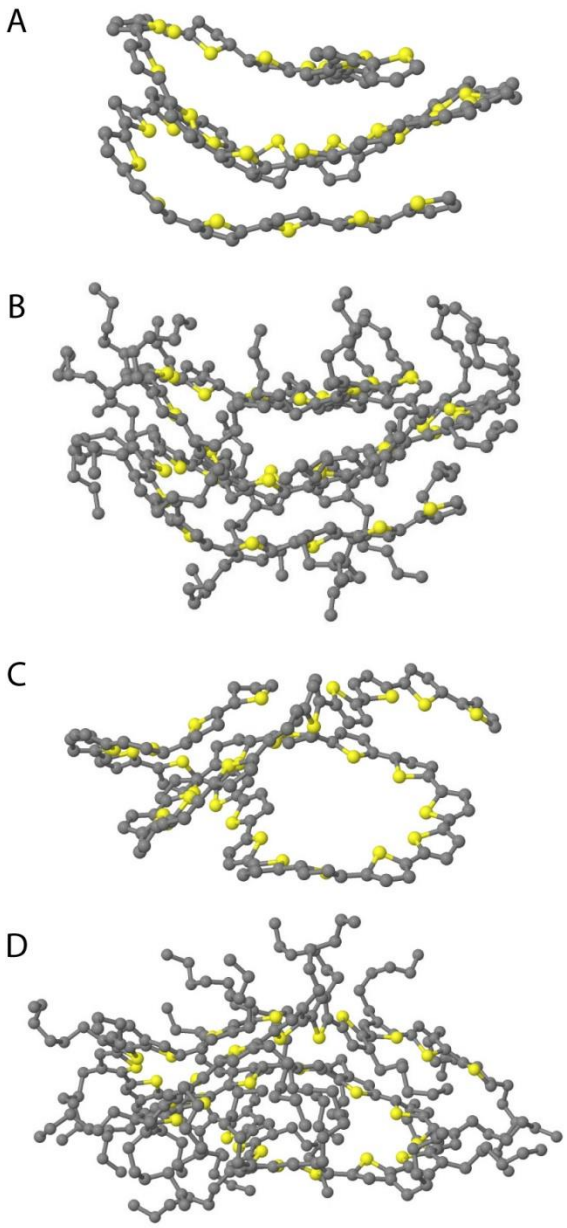

Figure 6.8: Sideview of a *rr*-P3HT 30 monomer chain conformation showing only backbones (A) and backbones with side-chains (B). Sideview of a *rra*-P3HT 30 monomer chain conformation showing only backbones (C) and backbones with side-chains (D). H-atom is not shown for clarity.

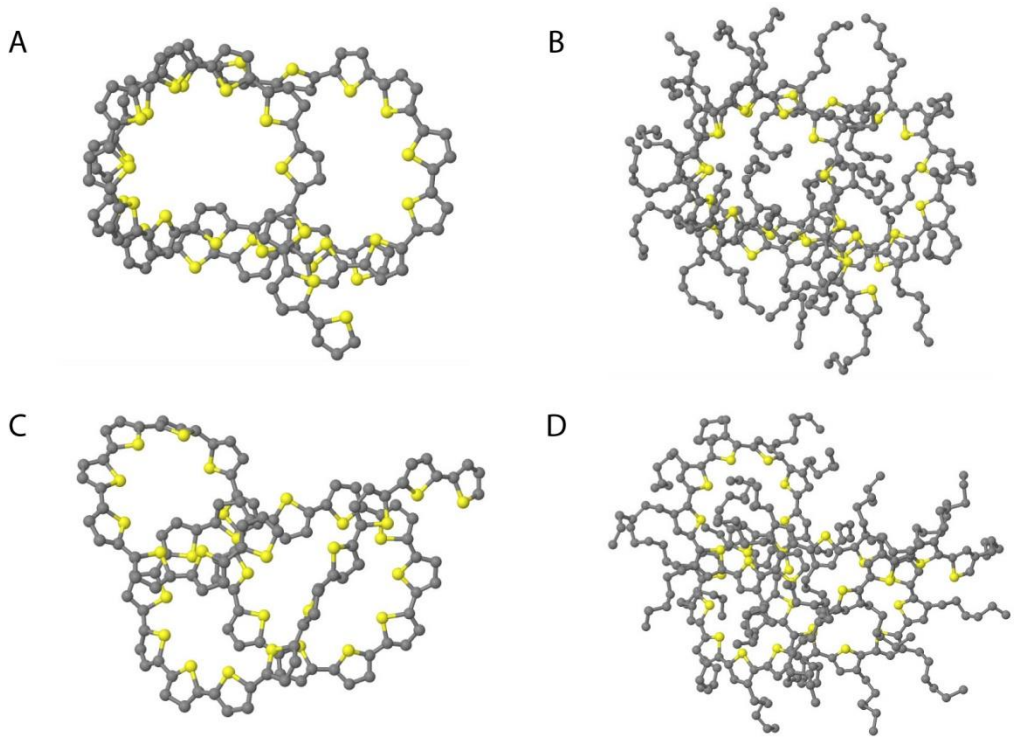

Figure 6.9: Topview of a *rr*-P3HT 30 monomer chain conformation showing only backbones (A) and backbones with side-chains (B). Topview of a *rra*-P3HT 30 monomer chain conformation showing only backbones (C) and backbones with side-chains (D). H-atom is not shown for clarity.

chain indicates the ability of the polymer to form well-aligned folded structures facilitated by the packing of alkyl side-chains. In contrast, while the regiorandom chain forms a similar folded hairpin structure, due to the steric interactions between the randomly located side-chain units, the backbone is twisted and is unable to form structures with the level of ordering seen for the regioregular polymers.

6.4 CONCLUSION

By using single molecule fluorescence excitation polarization spectroscopy, we demonstrate the importance of side-chains on single P3HT conformations even in the absence of interchain packing effects. With the regioregular polymer, every single P3HT chain yields a highly ordered conformation. However, as the percentage of HT linkages decreases, side-chain interactions perturb polymer chain conformations, resulting in the wider distribution of chain conformations. As the excitation wavelength is shifted from 458 to 514 nm, the observed anisotropy increases for both *rr*- and *rra*-P3HT. The results indicate that the conjugation length of the higher ordered region of a chain is longer presumably because a pi-pi stacking not only stabilizes a chain packing but also extends a chromophore length. These conclusions are well supported by molecular dynamics simulations on atomistic models of *rr*- and *rra*-P3HT chains. This indicates that regioregularity is a very important parameter for P3HT not just for the conjugation length and packing of chains in polymer films, but even for the conformation of the chain at the single molecule level. This is in contrast to poly[2-methoxy-5-(2'-ethylhexyloxy)-1,4-phenylenevinylene] (MEH-PPV) which has been shown to form highly ordered conformation even for regiorandom samples.[100] Moreover, computational studies of MEH-PPV suggest that both the electronic properties and the conformational states can be reasonably modeled ignoring the side-chains.[167] Such contrast between MEH-PPV and P3HT suggests that the role of side-chains in morphology control might be dependent on

the density of side-chains along a backbone.[145] For computational studies of P3HT, side-chains cannot be ignored because the chain conformations as well as the resulting optoelectonic properties are strongly affected by side-chain interactions. This clearly demonstrates that for computational studies of conjugated polymer conformations the details of simulations must be optimized depending on the system that is being studied. Finally, single *rr*- and *rra*-P3HT chains provide an excellent model system to study structure–property relationships of conjugated polymers, as the full range of conformations—from highly oriented to completely isotropic—can be achieved by tuning both the amount and placements of HT couplings.

Acknowledgement for co-author contributions:
I would like to thank Dr. Johanna Brazard, Dr. Joshua Bolinger and Dr. Mattew Traub for helping me performing the experiments, Mr. Robert Ono, Dr. Zicheng Li, Dr. Zong-Quan Wu, and Prof. Christopher Bielawski for synthesizing the polymers, Dr. Benjamin Hanson and Prof. Venkat Ganesan for performing the molecular dynamics simulations, and Prof. David. A. Vanden Bout and Prof. Paul F. Barbara for helping me designing the experiments.

Chapter 7: Conformational Effect on Energy Transfer in Single Polythiophene Chains

This chapter was reproduced in part from: Adachi, T.; Lakhwani, G.; Traub, M. C.; Ono, R. J.; Bielawski, C. W.; Barbara, P. F.; Vanden Bout, D. A. *J. Phys. Chem. B* ***2012****, 116, 9866-9872.*

7.1 INTRODUCTION

The morphology of conjugated polymers (CP) is a critical parameter in determining their electronic properties.[12,19,51,168] As such, it is important to control and define polymer morphologies and to understand how morphology affects energy transfer[169,170], which ultimately determines the performance of organic electronic devices that utilize CPs, such as photovoltaics and light emitting diodes. A major obstacle to establishing such structure-property relationships is the complex and heterogeneous nature of CP films that are composed of a myriad of three dimensional nano-scale domains.[39] Because of this heterogeneity, the use of bulk characterization methods measures an average property resulting from the various polymer chain interactions. This limits the ability of ensemble techniques to obtain a molecular level understanding of structure−property relationships. Single molecule spectroscopy has been a useful technique to simplify these problems and make them tractable.[40-42,171] For example, it was recently shown that single chains of poly[2-methoxy-5-(2'-ethylhexyloxy)-1,4-phenylenevinylene] (MEH-PPV) fold into highly ordered rod conformations[100,172] and the exciton migration within such single chains may extend over 25-75 nm.[44] However, developing a more complete understanding of energy transfer in these and other materials requires quantitative treatment of multiple polymer chain conformations.

In this work, we have studied the effects of conformation on energy transfer using single poly(3-hexylthiophene) (P3HT) chains with different degrees of regioregularity as

model systems of ordered and disordered CP conformations. Polythiophenes are an important class of compounds that have found use as photoactive materials in efficient organic photovoltaic devices.[31,94,144,173] Moreover, it was recently demonstrated that regioregularity[174,175] and side-chain steric effects[153] control the conformations of P3HT even at the single chain level where interchain interactions are absent. In short, regioregular (*rr*-) P3HT chains fold into a highly ordered conformations while chains of regiorandom (*rra*-) P3HT assume a wide variety of conformations, from ordered to disordered. By measuring the single chain fluorescence spectra and simultaneously the single molecule fluorescence polarization anisotropy of the aforementioned chains, we were able to evaluate the efficiency of energy transfer as a function of conformation.

The aforementioned technique has been used by several groups,[108,176-179] and can provide a quantitative understanding of energy transfer within polymer chains when the experimental results are compared with simulations. For example, despite the limitations of Förster Resonance Energy Transfer (FRET) for simulating energy transfer in conjugated polymers,[70,71,180] the experimental polarization anisotropy results and distribution of single chain emission peak energies from single chains of MEH-PPV can be well reproduced by a simple model of FRET in appropriate simulations.[176] Indeed, these results confirmed that the highly organized structure of single MEH-PPV chains enables excitons to efficiently find a relatively small number of low energy sites. By applying this method to P3HT of differing regioregularity, we demonstrate herein that the emission of chains with highly ordered conformations is dominated by a relatively small number of sites as compared to chains adopting disordered conformations. Collectively, these results provide the basis for a quantitative understanding of how local nanostructure affects energy transfer in conjugated polymers.

7.2 EXPERIMENTAL SECTION

7.2.1 Materials and Methods

97% HT-HT (HT = head-to-tail) coupling of *rr*-P3HT was synthesized by the Grignard metathesis (GRIM) method[158] and 64% HT-HT coupling *rra*-P3HT was synthesized by the oxidative polymerization of 3-hexylthiophene using $FeCl_3$ as the oxidant[159] as described previously.[175] P3HT with narrow polydispersity indices (PDIs) was obtained by fractionation using gel permeation chromatography (Viscotek, GPCmax VE-2001). For *rr*-P3HT, the number average molecular weight (M_n) = 148 kDa, PDI = 1.35, and for *rra*-P3HT, M_n = 191 kDa, PDI = 1.33. Isolated P3HT chains embedded in a PMMA film (200 nm) were obtained by spincoating PMMA/toluene solution containing ultralow concentration of P3HT. To avoid photo-oxidation, samples were made in a N_2 filled glove box and sealed using epoxy resin. Only a small fraction (< 5%) of molecules showed fluorescence blinking or bleaching behavior in our polarization experiments. To avoid convoluting the effects of photooxidation with the intrinsic photophysics of the system, these molecules were not included in histograms. More details of sample preparation can be found elsewhere.[175]

Single molecule fluorescence spectra were obtained from a confocal scanning microscope apparatus at room temperature. A 488 nm line of an Ar-Kr laser (Melles Griot, model 35 LAL-030-208) was focused through an objective lens (Zeiss, Achrostigmat, 100X, NA1.25) to excite single P3HT molecules. The excitation power was estimated as ~ 80 W/cm^2. Emitted light was filtered with a 488-nm notch filter and focused onto a spectrometer combined with a liquid N_2 cooled CCD (Princeton Instruments). An integration time of 20 seconds per spectrum was employed, and six individual spectra were collected for each molecule. Results were averaged over the six

spectra. When photobleaching of a molecule was observed during a measurement, only the spectra before bleaching were used for averaging.

A wide-field single molecule fluorescence polarization spectroscopy apparatus[176] was used to simultaneously probe the excitation and emission anisotropy of individual molecules. The apparatus employed was based on an inverted microscope (Zeiss, Axiovert 100) with a high NA objective lens (Zeiss, ApoPlano, 100X, NA1.4). The excitation source is a 488-nm line of an Ar ion laser (Melles Griot, model 35-IMA-040-208) and the linearly polarized excitation beam was rotated in the x-y frame around the axis of propagation by using an electro-optical modulator (EOM, Fastpulse technology, model 3079-4), a voltage amplifier (Trek, model 601-1), and a programmable function generator (Wavetek, model 29A) using a method previously described.[176] The illumination area was ~20 μm (FWHM) and the excitation power was estimated as ~1 W/cm^2. Emitted light was filtered through a 488-nm notch filter, passed through a Glan-Thompson polarizer (Newport) mounted on a computer-controlled rotation stage (Newport NSR-1) and focused onto an EMCCD camera (Andor, iXon$^+$ DU-897E). Fluorescence images were recorded at a fixed emission polarizer angle while excitation polarization was rotated from 0 to 180 degrees. The aforementioned measurement was repeated for six different angles of the emission polarizer. Excitation modulation curves were obtained by integrating fluorescence transients from all six emission polarizer angles, while emission modulation curves were obtained by integrating the fluorescence transients of each emission polarizer angle. Both excitation and emission modulation curves were fit to the eq 1:

$$I(\theta) \propto 1 + M \cos 2(\theta - \phi) \qquad (1)$$

to extract the modulation depth (M) and the phase angle (ϕ) representing the in-plane orientation of maximum absorption/emission. To probe all the possible conformation and

orientation of molecules in the laboratory frame, fluorescence transients from hundreds of molecules were measured and the histograms of excitation (M_{ex}), emission modulation depth (M_{em}) and the phase difference between excitation and emission polarization ($\Delta\phi$) were constructed. More details of the setup and the analysis are described elsewhere.[176]

7.2.2 FRET simulation

The Förster Resonance Energy Transfer (FRET) simulations were carried out using a Pauli master equation to describe the energy transfer rate between various chromophores within a single polymer chain and the probability of an excitation being at each specific chromophore at a given time. The details of simulations can be found in our previous report[176] and references therein.

A series of polymer chains (each of which is referred to herein as a conformation) have been obtained from previously reported Monte Carlo simulations using a beads-on-a-chain model.[47,181] A conformation in our simulation was made up of 200 beads, with the connection between each bead pair treated as an independent chromophore with a length equivalent to ~4 monomers. For conjugated polymers, the effective conjugation length (> 10 monomer units) was substantially larger than either the interchromophore distances or the FRET radius for single step energy transfer. In such cases, the efficiency of energy transfer as a function of distance typically falls off more slowly than $1/R^6$ for point dipoles, and line dipole treatments provide a more accurate approximation of energy transfer.[181,182] Additionally, recent results have suggested that energy transfer in conjugated polymers does not necessarily occur in the weak coupling limit[70,124] but through more efficient coherent energy transport. Because of the small size of our model chromophores relative to the actual chromophore length, we were restricted to a point dipole approximation in our energy transfer simulations. This limitation makes our simulation results of energy transfer rates less accurate, but the point-dipole model will

most likely underestimate the energy transfer rates relative to line dipole or coherent models unless the distance between chromophores are close to zero. Therefore, they provide an effective lower limit on the efficiency of energy transfer and demonstrates the effect of conformation in these systems.

The FRET rate between two chromophores depends on the distance between them, the orientation factor, the quantum yield of the donor chromophore, and their spectral overlap. The first two factors depend on the conformation of the chain used for the simulation. For example, an anisotropic conformation would have a high value of orientation factor between any given two chromophores because the probability of having the transition dipole moment of chromophores aligned in thesame direction is high, while an isotropic conformation would have more randomly arranged transition dipole moments and lower orientation factors. The spectral overlap between two chromophores depends on the emission spectrum of a donor chromophore and the absorbance spectrum of an acceptor chromophore. The absorbance spectrum shape of each chromophore site was simulated with a normalized lognormal function with a fixed bandwidth (2000 cm^{-1}), asymmetry (1.2) and a resonance energy randomly chosen from an energy distribution described below. Keeping the Stokes shift (500 cm^{-1}) unchanged for all chromophores, the spectral overlap was dependent upon the resonance energy given to the chromophores. The energy distribution of the chromophore sites was chosen to be a normalized bigaussian distribution obtained by using the following parameters: 1250 cm^{-1} as bandwidths of both gaussians with one peaked at 22000 cm^{-1} and another at 19500 cm^{-1}. The choice of parameters involved in the energy distribution and the Stokes shift were validated by comparing the ensemble emission histograms obtained from the simulation to that obtained via the experiment. The quantum yield of the donor

chromophores was taken to be 0.2.[183] The same energy distribution and Stokes shift were utilized for all of the polymer conformations.

In general, a FRET simulation performed for a hundred times for every conformation. In each simulation, the resonance energies of the chromophore sites were assigned randomly from the energy probability distributions. The changes in modulation depth were averaged over multiple tilt and twist angles in the laboratory frame. The simulation yielded histograms of modulation depths in excitation and emission, distance of energy transfer, the number of emitting chromophores and histograms of resonance energies of absorbance and emission.

7.3 RESULTS AND DISCUSSION

7.3.1 Single molecule fluorescence excitation/emission polarization spectroscopy

The change in modulation depth from excitation to emission for individual P3HT chains provides a snapshot of energy transfer within each chain.[176] In the limiting case of no energy transfer, the excitation and emission anisotropies should be identical, while in the case of complete energy funneling to a single chromophore, the emission anisotropy value would be unity.[177] Figure 7.1A shows the experimental histograms of simultaneously measured excitation (M_{ex}) and emission modulation depths (M_{em}) for 185 single *rr*-P3HT chains at 488 nm excitation. The M_{ex} histogram is highly peaked around 0.7 with a mean value of 0.69, consistent with previously reported results,[174,175] indicating that nearly every *rr*-P3HT chain folded into a highly ordered conformation. The peak for the M_{em} histogram was shifted to higher values, with a mean value of 0.74. For the majority of molecules, the M_{em} increased relative to its corresponding M_{ex} (Figure 7.3A).

The contrast between M_{ex} and M_{em} was more pronounced for *rra*-P3HT. Figure 7.2A shows the experimental histograms of M_{ex} and M_{em} from 195 chains. The M_{ex}

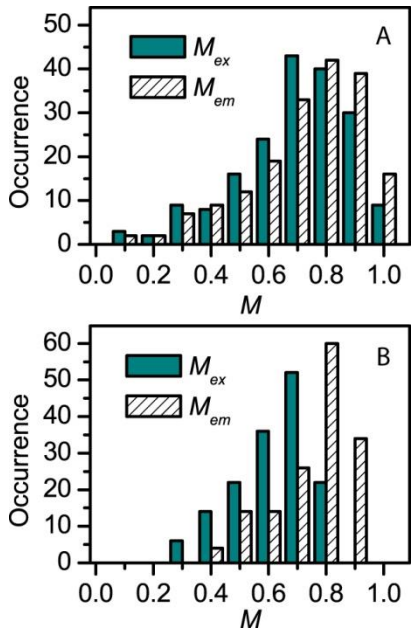

Figure 7.1: Single molecule excitation/emission correlation polarization anisotropy results of *rr*-P3HT. (A) The experimental and (B) the simulated histograms of excitation and emission polarization modulation depth.

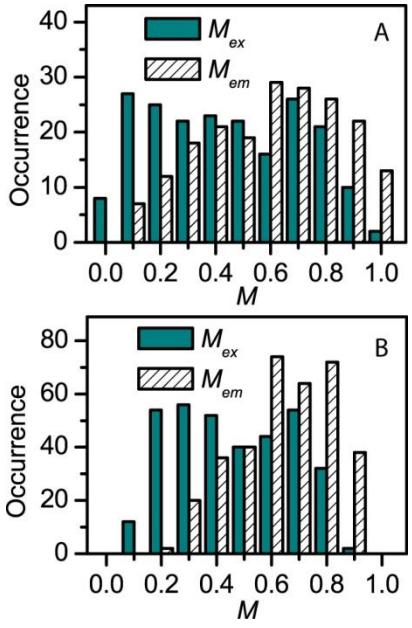

Figure 7.2: Single molecule excitation/emission correlation polarization anisotropy results of *rra*-P3HT. (A) The experimental and (B) the simulated histograms of excitation and emission polarization modulation depth.

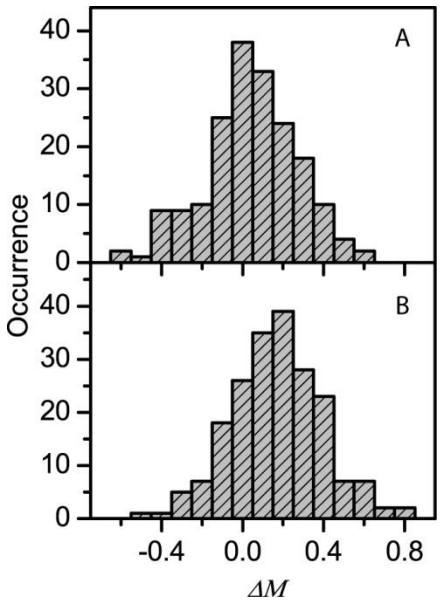

Figure 7.3: Histograms of the difference between excitation and emission polarization modulations for individual molecules. (A) *rr*-P3HT and (B) *rra*-P3HT.

histogram was broad and featureless with the mean value of 0.45, which was similar to the result previously reported.[174,175] On the other hand, the M_{em} histogram was highly peaked around 0.7 with the mean value of 0.62. With respect to the results obtained for *rr*-P3HT, more chains of *rra*-P3HT show increased *M* values (Figure 7.3B).

One of the major differences between *rr*- and *rra*-P3HT is the histogram of $\Delta\phi$ values (Figure 7.4). $\Delta\phi$ represents the difference between the orientation of maximum absorption and emission. Only small $\Delta\phi$ is expected from *rr*-P3HT because the majority of chromophores are aligned with respect to each other in highly ordered chains and energy transfers between aligned chromophores should not yield a significant change in φ. However, a large $\Delta\phi$ can be observed from *rra*-P3HT, particularly for more disordered chain conformations. In fact, Figure 7.4 shows that the distribution of $\Delta\phi$ values for *rra*-P3HT spreads toward much larger values than that for *rr*-P3HT. This trend can also be observed from the sub-ensemble $\Delta\phi$ histograms of *rra*-P3HT (Figure 7.5). The $\Delta\phi$ values for large M_{ex} values (>0.7, highly ordered chains) were much smaller than those for small M_{ex} values (<0.4, disordered chains). The same can be observed for *rr*-P3HT (Figure 7.6). The strong correlation between M_{ex} and $\Delta\phi$ values confirmed that there is energy transfer in single chains of P3HT.

7.3.2 Single molecule fluorescence spectra

Fluorescence spectra of single P3HT chains provide additional experimental data for evaluating energy transfer simulations. Single molecules of *rr*- and *rra*-P3HT provide a particularly valuable test case for these experiments because of their drastic differences in conformation. Figures 7.7A and E show the ensemble averaged fluorescence spectrum from 100 single molecules of *rr*- and *rra*-P3HT, respectively. Fluorescence spectra of both *rr*- and *rra*-P3HT in chloroform solution are shown as the red solid curve. While the *rra*-P3HT spectrum is almost identical to its solution spectrum (Figure 7.7E), the *rr*-

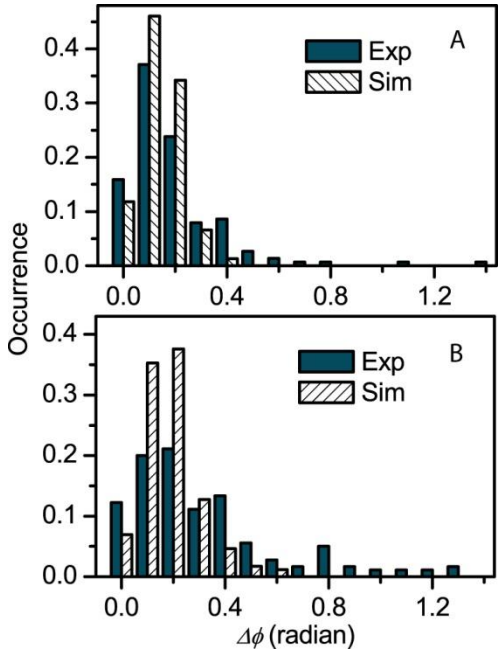

Figure 7.4: The histograms of experimental and simulated phase difference between excitation and emission polarization of each molecule from (A) *rr*-P3HT and (B) *rra*-P3HT.

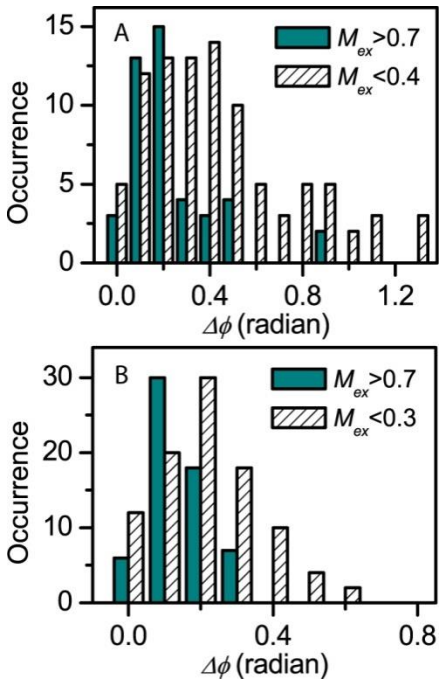

Figure 7.5: (A) Experimental and (B) simulated **s**ub-ensemble histogram of phase difference between excitation and emission polarization modulation of *rra*-P3HT.

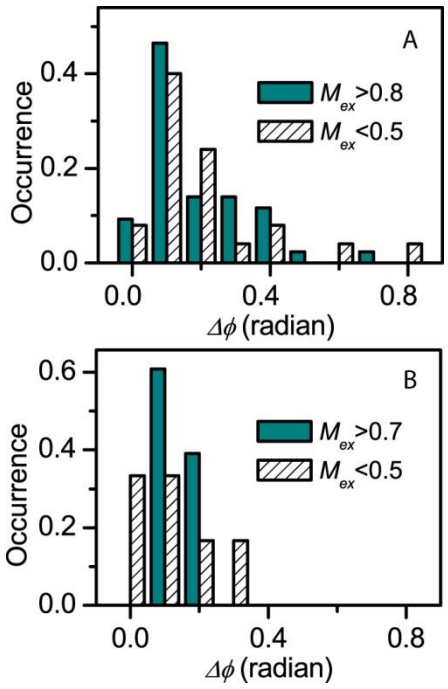

Figure 7.6: (A) Experimental and (B) simulated sub-ensemble histogram of phase difference between excitation and emission polarization modulation of *rr*-P3HT.

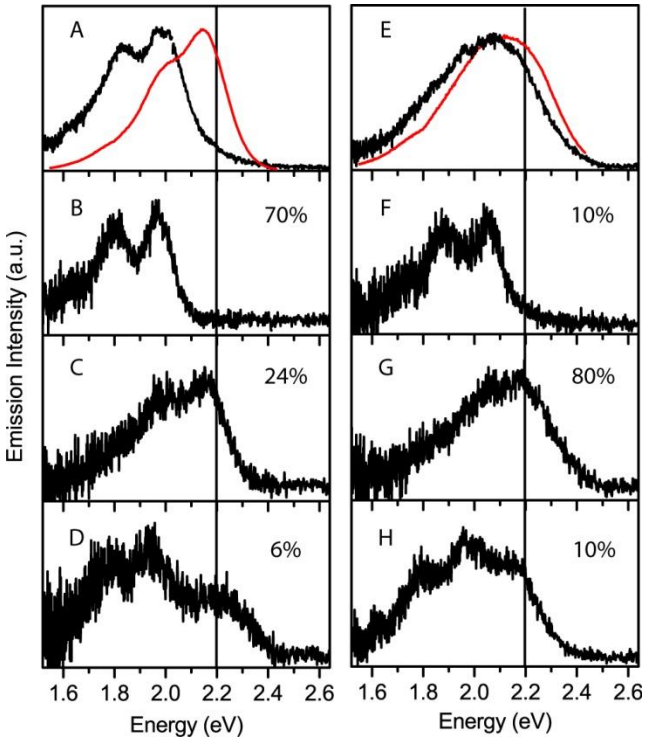

Figure 7.7: Ensemble fluorescence spectrum (black curve) and solution spectrum (red curve) of (A) rr-P3HT and (E) rra-P3HT. Representative single molecule fluorescence spectra of (B-D) rr-P3HT and (F-H) rra-P3HT. The probability of spectrum observed is shown as inset. A vertical line is inserted at 2.2 eV.

P3HT spectrum shows substantial bathochromic shift relative to its solution spectrum (Figure 7.7A).

Single molecule fluorescence spectra can be roughly categorized into three classes as shown in Figures 7.7B-D for *rr*-P3HT and 7.7F-H for *rra*-P3HT, respectively. Class 1 (Figure 7.7B and F) showed well-defined Franck-Condon progressions with a single 0-0 peak energy which is red-shifted relative to that recorded in solution. These spectra imply either efficient funneling to a single chromophore or formation of multiple energetically similar exciton traps. Interestingly, the spectral shape of single P3HT chain is different from that of bulk films. The bulk film fluorescence spectrum could not be fit to Franck-Condon progression.[58,61] We speculate that the difference was due to the existence of strong interchain interactions in bulk films that were absent in the single chains despite the fact that they were folding into ordered conformations. Class 2 (Figure 7.7C and G) showed broad, featureless spectra with peak wavelengths similar to that of the solution fluorescence spectrum while Class 3 (Figure 7.7D and H) appeared to be composed of multiple well-defined vibronic progressions.[184] These latter two classes suggested to us that energy is funneled to a multitude of chromophores with overlapping spectra (Class 2) and to multiple local low-energy sites with different peak energies (Class 3).

Clear correlations were observed between the conformation of the polymer chains and their emission spectra. For the well-ordered *rr*-P3HT, ~70% of molecules in the ensemble show a class 1 spectrum; for *rra*-P3HT, ~80% of molecules show a class 2 spectrum. The relationships clearly indicate that clearly indicates that the ordered structure of *rr*-P3HT chains facilitates formation of and energy funneling to low energy exciton traps. In contrast, the higher degree of disorder of the *rra*-P3HT leads to emission from a broader array of chromophores. The peak energy distribution of 0−0 emission

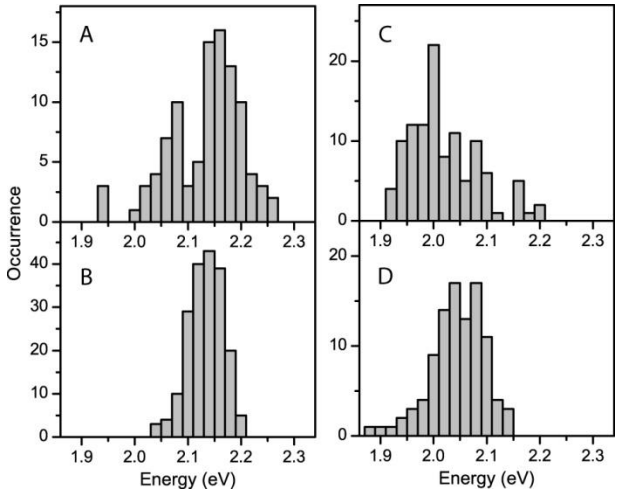

Figure 7.8: The peak wavelength distribution of single molecule spectrum of (A) *rra*-P3HT and (C) *rr*-P3HT. Simulated emission peak distribution of (B) disordered and (D) ordered conformation.

lines of rr- and rra-P3HT (Figures 7.8A,B) further indicated that the emission of *rr*-P3HT occur from lower energy sites than that of *rra*-P3HT.

A smaller fraction of each set show the reverse behavior: class 2 spectra were observed from 24% of the *rr*-P3HT spectra, potentially corresponding to the lower M_{ex} molecules in the ensemble. On the other hand, 10% of *rra*-P3HT single molecule spectra show red-shifted class 1 characteristics. These chains may correspond to rra-P3HT with high M_{ex} values whereas the remaining 5−10% of each distribution falls into the intermediate class 3. More detailed resolution of overlapping chromophore spectra in conjugated polymers can be obtained by measuring at lower temperature;[122,185] however, this falls beyond the scope of this report.

7.3.3 FRET model simulations on different chain conformations and the comparison with the experimental results

To quantify the effects of chain conformations on energy transfer, FRET simulations were performed on several different model polymer conformations. (shown in Figure 7.9) In order to focus specifically on the effects of chain ordering, all parameters aside from polymer conformation were set to the same values as described in the experimental section. We used a highly ordered rod conformation with a radius of gyration (R_g) of 20 nm and the anisotropy of the absorption tensor (A) of 0.8 as a model for *rr*-P3HT. These conformational parameters reasonably reproduced the experimental M_{ex} histogram of *rr*-P3HT (Figure 7.1). For *rra*-P3HT, there was no single conformation that reproduced the corresponding broad experimental M_{ex} histogram (Figure 7.2A); however, it was possible to simulate most of the experimental data with a combination of only two conformations. In this study, we used a disordered and collapsed conformation with R_g of 20 nm and A of 0.13 and a relatively extended chain conformation with R_g of 81 nm and A of 0.7. While these conformations clearly do not sample the full range of

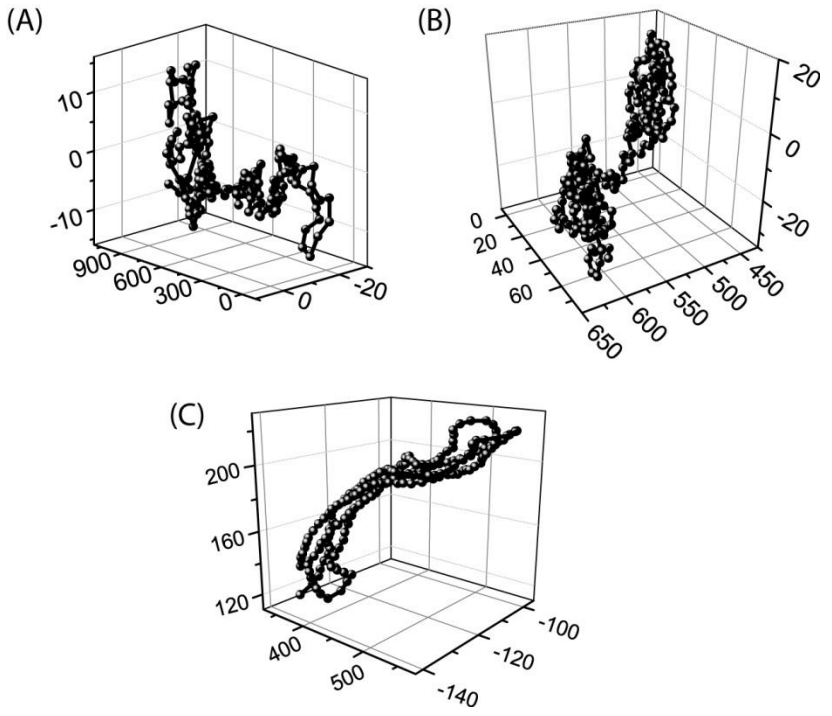

Figure 7.9: Plotted chain conformations of (A) disordered chain with a radius of gyration (R_g) of 81 nm and the anisotropy of the absorption tensor (A) of 0.7, (B) disordered chain with R_g of 20 nm and A of 0.13, and (C) ordered chain with R_g of 20 nm and A of 0.8. The scale of axes is adjusted for clarity.

Acknowledgement for co-author contributions:
I would like to thank Dr. Girish Lakhwani and Dr. Mattew Traub for helping me performing the experiments, Mr. Robert Ono and Prof. Christopher Bielawski for synthesizing the polymers, Dr. Girish Lakhwani for performing the FRET model simulations, and Prof. David. A. Vanden Bout and Prof. Paul F. Barbara for helping me designing the experiments.

conformations present in such a heterogeneous sample, the combination of these two conformations could reproduce the broad experimental M_{ex} histogram (Figure 7.2B). In contrast to approaches that do not include a specific model of chain conformation and model energy transfer without distance dependence or spectral overlap,[108] the approach described herein provides a direct means to understand and test the effects of chain conformation on the energy transfer.

FRET simulations using the conformations described above successfully reproduced all the experimental results of both *rr*- and *rra*-P3HT. Figures 7.1B and 7.2B show the simulated M_{em} histograms which are similar to the experimental results (*cf.* Figures 7.1A and 7.2A). Figure 7.4 shows the simulated $\Delta\varphi$ histograms, and $\Delta\phi$ values are distributed toward larger values for the simulations of the disordered conformations than that of the ordered conformation, as experimentally observed for *rr*- and *rra*-P3HT. Beyond these excitation and emission anisotropy results, the histograms of fluorescence peak wavelength were also reproduced. Figures 7.8B and D show the simulated peak wavelength histograms. The peak wavelengths of the ordered conformation are centered at much lower energies than those of the disordered conformation, and the peak position of both histograms is similar to the experimental data.

The simulations allow us to further quantify the effect of conformation on energy transfer efficiency. The number of sites from which excitons ultimately emit, after energy transfer events within the fluorescence lifetime, can be used to quantify the energy transfer efficiency. Because the initial number of sites and the fluorescence lifetime are the same for both ordered and disordered conformations, the final number of emitting sites is dependent on the rate of each energy transfer process. The number of emitting sites in the ordered conformation is ~9 sites (~5%) while that in the disordered conformations is ~22 sites (~10%). These observations are consistent with the differences

in the emission spectra observed for the two polymers. The fewer emitting sites for the *rr*-P3HT leads to more uniform spectra that are peaked at lower energy. The larger number of emitting sites in the *rra*-P3HT yields a broader distribution of emission energies that have not funneled to the lowest energy sites. This result directly demonstrates the effects of conformation on energy transfer in conjugated polymers. Forster *et al.* previously studied the fluctuation of the emission polarization in single chains of polythiophene derivatives (−100 monomers per chain) and reported that the energy transfer was inefficient in the system.[186] The current work also observes emission from more than a single site (or even a few sites), but the efficiency is gauged to depend on the conformation of the polymer. Disordered conformations such as those of *rra*-P3HT (or the polythiophene with bulky side chains in ref [186]) yield a larger number of emitting sites than the well-ordered *rr*-P3HT.

The current study underscores the role of conformation on energy transfer in single chains of conjugated polymers. Also of significance is that we show that a simple FRET model simulation using only a few conformations could reproduce all the experimental data. In particular, the fact that only two model conformations reasonably reproduces the the experimental results for *rra*-P3HT indicates that such models may be used as a framework to further capture the details of properties of single conjugated polymer chains. Quantum calculations that deal with the details of polymer chains such as the influence of local conformation[46] and interchain/intrachain interactions[187-189] are important, but these calculations are typically limited to polymer chains that are much smaller than actual CP samples due to computational limitations. However, such calculations can guide the incorporation of an energy distribution reflective of the structure into our model framework and will provide a more comprehensive

understanding of energy transfer within local nanostructures of conjugated polymer bulk films.

7.4 CONCLUSION

Simultaneously measured excitation and emission polarization anisotropies from individual *rr*- and *rra*-P3HT chains and single molecule fluorescence spectra were compared with a FRET model simulation on ordered and disordered chain conformations. From these experiments, an increase in the mean single chain polarization anisotropy from excitation to emission was observed for both *rr*- and *rra*-P3HT. The majority of single *rr*-P3HT fluorescence spectra showed a red-shifted and well-defined Franck-Condon progression while that of *rra*-P3HT showed broad and featureless spectra which are almost identical to the solution spectrum. The peak emission wavelengths of *rr*-P3HT are at substantially lower energy than those of *rra*-P3HT. Simulations using a simple FRET model reproduced these experimental results and quantified that the energy transfer within polymers having ordered conformations was at least twice more efficient than for those in disordered conformations. Excitons may be transferred further to reach fewer and lower energy sites in more ordered conformations, resulting in uniform lower energy emission peaks. Disorder in the chain conformation may have disrupted the energy transfer and resulted in emission from a greater number of sites with various energies which yielded a broad and featureless spectrum. Collectively, these results demonstrate that the chain conformation can significantly alter the transfer of energy in single chains. In bulk films, both intra- and interchain interactions play important roles within complicated polymer networks. Using single chains as a model system, an understanding intrachain energy transfer can be obtained. Future work will examine the dependence of intra- and inter-molecular interactions on energy transfer to develop model frameworks for progressively more complex and larger scale polymer systems.

Chapter 8: Interchain Chromophore Interactions and Photophysics in Polythiophene Aggregates

8.1 INTRODUCTION

Poly(3-hexylthiophene) (P3HT) is a widely studied model compound to understand the mechanism of organic photovoltaic devices.[12,19,142,173] How chains are oriented and packed in bulk films is a critical factor in determining the interchain couplings of chromophores and therefore the performance of devices. However, the fundamental understanding of the effect of chain couplings on various physical properties is often limited in ensemble characterization methods due to the complicated and heterogeneous nature of bulk film morphology.[39,40] Single molecule spectroscopy of conjugated polymers is a great tool to simplify the complication.[40-42,99] In chapter 7, we compared the efficiency of energy transfer between ordered and disordered single conjugated polymer chains using P3HT with different degree of regioregularity (*i.e.*, the percentage of head-to-tail linkages between monomer units in the polymer backbone). The comparison between the results from experiments and a simulation quantified that energy transfer in an ordered conformation is at least twice more efficient than that in a disordered conformation. The studies in single chains mainly probe the morphological effect on intrachain energy transfer, and, as a next step, it is necessary to study interchain energy transfer that is important process in bulk films.

Herein, we demonstrated the morphological effect on the efficiency of energy transfer in the isolated aggregates of conjugated polymer chains, where interchain interactions play important roles. In chapter 5, we have developed a technique to control the aggregation process of conjugated polymers by applying solvent vapor annealing (SVA).[190] This allowed us to prepare isolated polymer aggregates with define morphological order, and the aggregates formed from poly[2-methoxy-5-(2'-

ethylhexyloxy)1,4-phenylenevinylene] (MEH-PPV) were highly ordered. The studies in such a new model system revealed that exciton diffusion in highly ordered MEH-PPV aggregates can be as long as 20-60 nm. By applying this technique for P3HT with different degree of regioregularity, we were able to form ordered and disordered P3HT aggregates. This demonstrates that SVA can be applied for the aggregation of not only MEH-PPV but also other polymer systems. The comparison of the time transients of the fluorescence intensity between regioregular (*rr*-) and regiorandom (*rra*-) P3HT aggregates clearly showed the morphological effect on energy transfer. Furthermore, the quantitative analysis of the fluorescence time transients may have indicated the existence of fast interchain energy transfer mechanism.

8.2 EXPERIMENTAL SECTION

P3HT with different degree of regioregularity (*i.e.*, the percentage of head-to-tail linkages between monomer units in the polymer backbone) was synthesized and further purified by using a GPC to obtain narrow molecular weight distribution[175] as previously described in Chapter 6. Here, M_n =10kDa, PDI =1.1 for *rr*-P3HT and M_n =48kDa, PDI = 1.33 for *rra*-P3HT were prepared. Both polymers were spincoated from toluene/PMMA solution on a glass substrate in a N_2 filled glove box. Samples were transferred to a home-built gas flowing chamber and fluorescence images were acquired by using a home-built wide-field microscopy apparatus[100,131] (see details in Chapter 2 and 3) under N_2 flow to prevent a photo-degradation of P3HT. Figure 8.1A shows a wide-field fluorescence image of a *rr*-P3HT/PMMA thin film. The concentration of P3HT molecules is much higher (100-200 times) than a sample typically used for single molecule experiments. The number of molecules within a field of view before and after solvent vapor annealing was determined by counting molecules using a home written MATLAB program (Chapter 2). The concentration of molecules in the film before

solvent vapor annealing was too high to count the number of molecules. Therefore, the number of molecules was obtained for a film spincoated from a diluted solution, and then the counted number was multiplied by a dilution factor. For Figure 8.1A, there were about 5000 molecules in the field of view.

The morphological order of aggregates was probed by excitation polarization spectroscopy[100] described in Chapter 2. Briefly, linearly polarized excitation beam was rotated in the *x*-*y* plane of a lab frame. Fluorescence intensity was measured as a function of excitation angle θ, and a resulting fluorescence intensity transient (I) was fitted to the equation:

$$I(\theta) \propto 1 + M\cos 2(\theta - \phi) \tag{8-1}$$

to extract the modulation depth, M, which reflects the extent of alignment of chromophores within each conjugated polymer aggregate. ϕ is the orientation of maximum absorption.

Fluorescent transients of single conjugated polymer aggregates were acquired via time-resolved wide-field fluorescence microscopy and further analyzed with respect to the quenching depth of each blinking event with an algorithm written for MATLAB (Chapter 5).[190] First, the maximum intensity, I_{max}, of each transient was extracted by averaging over the 10 highest data points within the transient. This led to averaging over 10 s of the highest fluorescence intensity at a time resolution of 1 s per data point. Second, a quenching or de-quenching step was identified after the following conditions were met:

$\frac{|I(t) - I(t-\Delta t)|}{I_{\max}} \geq T$ and $\frac{|I(t+\Delta t) - I(t-2\Delta t)|}{I_{\max}} \geq T$ and $\frac{|I(t+2\Delta t) - I(t-3\Delta t)|}{I_{\max}} \geq T$ and $\frac{|I(t+3\Delta t) - I(t-4\Delta t)|}{I_{\max}} \geq T$ and $\frac{|I(t+4\Delta t) - I(t-5\Delta t)|}{I_{\max}} \geq T$ where I(t) is the intensity at time t, Δt the time resolution (here 1 s) and T the threshold (here T = 0.2 was chosen primarily due

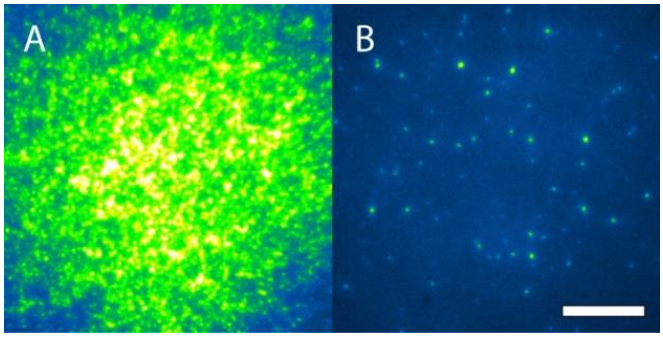

Figure 8.1: Wide-field fluorescence images of a *rr*-P3HT/PMMA thin film (A) before and (B) after solvent vapor annealing with a mixture of acetone and chloroform. Scale bar is 10 μm.

to noise). Finally, the relative size of the quenching or de-quenching step, Q, was extracted using the following equation:

$$Q = \frac{1}{5}\sum_{i=0}^{4} \frac{\left|I(t+i\Delta t) - I(t+(i+1)\Delta t)\right|}{I_{\max}}$$

Therefore, only step sizes at which the quenching or de-quenching event was longer than 5 s were considered.

8.3 Results and Discussion

By annealing samples using a carefully chosen solvent vapor, aggregates of P3HT chains were obtained (Figure 8.1B). The solvent has to be a good solvent for PMMA to swell the host matrix, but at the same time it has to be a bad solvent for P3HT to cause the aggregation of the chains. As described in Chapter 5, the size of aggregates can be tuned by controlling the quality of solvents, and this process was qualitatively explained by Ostwald ripening.[132]

$$R_C = \left(\frac{2\sigma}{kT}\right) v \frac{C_\infty}{C - C_\infty} \quad \text{for} \quad C > C_\infty \tag{8.1}$$

where σ is the inter-phase surface tension between the solute and the solvent, v is the atomic or molecular volume of the solute, C the solute concentration and C_∞ is the saturation limit of the solute concentration. Here, a mixture of acetone and chloroform at the vapor ratio of 70/30 was used to obtain as large aggregates as possible. After 40 minutes of solvent vapor annealing, the number of spots was significantly decreased as shown in Figure 8.1B. The size of these aggregates was below the diffraction limit of light, which made particle analysis feasible. Based on the number of spots before and after SVA, the average number of chains per aggregate was estimated to be about 100 chains (~1MDa) for *rr*-P3HT. The same experiments were performed for *rra*-P3HT, and the average number of chains per aggregate was estimated to be about 30 chains (~1.4 MDa)

There were three differences between the results reported for the MEH-PPV/PMMA system (Chapter 5) and the P3HT/PMMA system herein. First, there was no molecule in a background of P3HT aggregates after SVA (Figure 8.1B). For MEH-PPV/PMMA film, there were a number of single molecules observed even after SVA.[190] It can be explained as that, in the case of MEH-PPV, the concentration (C) of MEH-PPV in the system drops to the saturation concentration (C_∞) before all the molecules form aggregates. No aggregation occurs at the condition of C below C_∞. Therefore, a resulting film after SVA contains both large aggregates and many single chains. As the solubility of P3HT is lower than MEH-PPV in this experimental condition,[191,192] C_∞ for P3HT can be expected to be lower. We speculate that this low C_∞ made it possible for all molecules to aggregate before C dropped below C_∞ and resulted in a film with relatively homogenous aggregates and no single molecule in the background.

Second, although the mixture ratio of 60/40 was expected to yield even larger aggregates, every trial at this ratio resulted in different number and size of aggregates for P3HT/PMMA system. It was speculated that such irreproducibility was due to much smaller molecular weight of P3HT used herein (10 kDa) compared with 830 kDa for MEH-PPV in Chapter 5. For a small molecular weight of polymers, the solubility might change drastically when the acetone/chloroform mixture ratio was changed from 70/30 to 60/40. If R_c of aggregates were too high, it could result in a film with a few large aggregates. Reproducing such a film can be extremely difficult and in fact a few large aggregates were observed in some cases for the solvent mixture of 60/40. Considering the reproducibility of the experiments, the solvent ratio of 70/30 was used to obtain the largest P3HT aggregates possible.

Third, the significant decrease of the fluorescence quantum yield was observed from single chains to aggregates. Although the number of chains per aggregate is

estimated to be 100, the fluorescence intensity of P3HT aggregates was only 2-3 times higher than that of single chains. For the case of MEH-PPV, the intensity of aggregates was roughly proportional to the number of molecules per aggregate and a good anti-correlation between the number of aggregate per image and the average intensity of aggregates was obtained.[190] It is known that the quantum yield of fluorescence of P3HT as a solid film is 20 times lower than that as a solution.[59,62-64] The mechanism has been still debated, but it is generally agreed that strong interchain interactions facilitate any type of nonradiative decay path. The observation of such strong fluorescence quenching indicates the existence of strong interchain interactions within P3HT aggregates. This phenomenon prevented us from using the fluorescence intensity to estimate the number of chains within aggregates, and the size of aggregates in this study was estimated by solely relying on counting the number of molecules before and after SVA.

The morphology of *rr*- and *rra*-P3HT aggregates showed a significant difference. Figure 8.2A and B show the histogram of *M* values for *rr*- and *rra*-P3HT aggregates, respectively. The majority of *rr*-P3HT aggregates showed high *M* values (>0.6) and the histogram with the peak value of 0.9 and the mean value of 0.78. In contrast, the majority of *rra*-P3HT aggregates showed low *M* values (<0.4) and the histogram with the peak value of 0.3 and the mean value of 0.35. It was previously shown that the side-chains affect the morphology even at the single chain level where there is no interchain interaction (Chapter 6). Here, the contrast between *rr*- and *rra*-P3HT for aggregates is much higher compared to that for single chains. Even for *rra*-P3HT, molecules with high *M* values were observed in the case of single chains (Chapter 6). However, in the case of aggregates, the histogram showed almost no molecule with high *M* values for *rra*-P3HT (Figure 8.2B). The results indicate that the morphology of aggregates reflect the conformation of single chains in some extent. It is clear that all the individual chains have

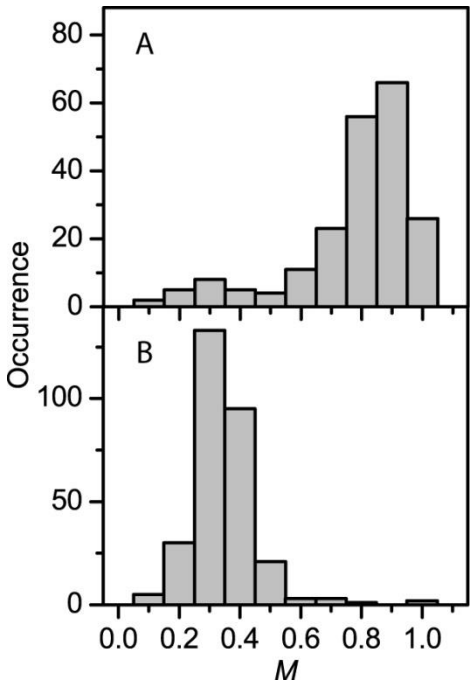

Figure 8.2: Modulation depth histograms of self-assembled aggregated of (A) *rr*-P3HT and (B) *rra*-P3HT.

to assume highly ordered conformation to assemble highly ordered aggregates. As shown in the case of *rra*-P3HT, the inclusion of disordered chains for the assembly of aggregates causes disordered morphology.

To examine the morphological effect on energy transfer, fluorescence transients as the function of time were measured. The fluorescence intensity of aggregates changes with time as photochemical quenchers, such as radical cations[129], are randomly generated within aggregates. It has been shown that the blinking behavior of fluorescence transients is the indication of efficient energy transfer in conjugated polymer domains (Chapter 4, 5). Figure 8.3A and B show typical fluorescence transients from *rr*-P3HT aggregates. All the aggregates showed such a discrete fluorescence blinking as observed in Figure 8.3A and B. For the aggregate in Figure 8.3A, the total fluorescence intensity was quenched in one-step. In the case of Figure 8.3B, several quenching steps were observed. By using the algorithm described in the experimental section, the histogram of quenching depth per blinking event was constructed from 86 aggregates (Figure 8.4). The mean quenching depth of the histogram was 0.51, and a number of blinking steps with more than 50 % of quenching depth were observed. These results indicate that there is efficient energy transfer within ordered aggregates.

In contrast, no discrete fluorescence blinking was observed from *rra*-P3HT aggregates. Figure 8.3C and D show typical fluorescence transients from *rra*-P3HT aggregates. All the aggregates showed this type of continuous fluorescence decay as a function of time, and a discrete blinking that was observed for *rr*-P3HT was not observed. At the same criteria used for the quenching depth analysis of *rr*-P3HT, no blinking step was found. It should be noted that Figure 8.3C and D were measured under an air environment. Under N_2 flow, the fluorescence transient of *rra*-P3HT aggregates was very stable, and no blinking or decay was observed. This is probably because a few

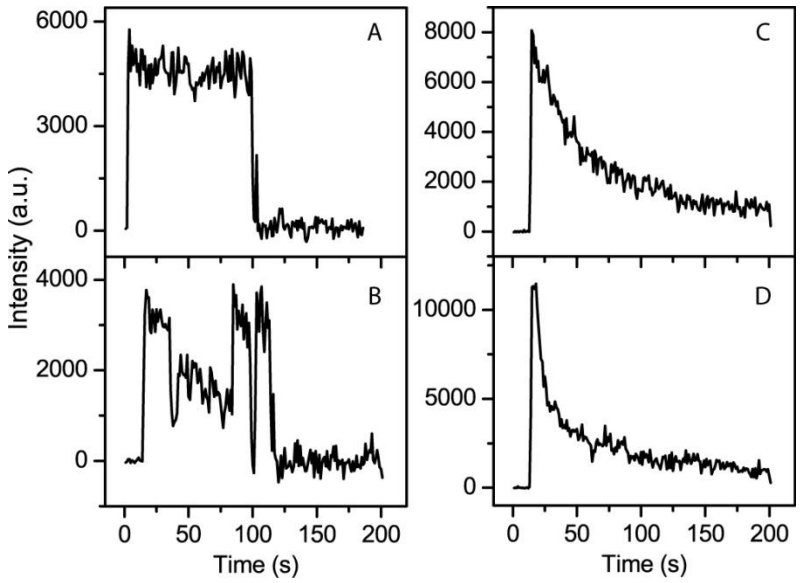

Figure 8.3: A fluorescence intensity transient of (A-B) *rr*-P3HT and (C-D) *rra*-P3HT aggregates under continuous irradiation of 488 nm laser line.

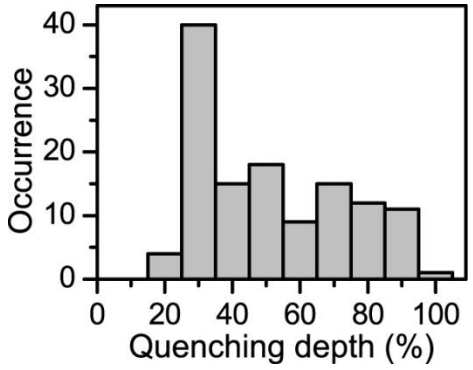

Figure 8.4: Quenching depth histogram of *rr*-P3HT aggregates.

oxygen molecules (quenchers) are not enough to quench any observable amount of the fluorescence of *rra*-P3HT aggregates. These results suggest that energy transfer in disordered aggregates is much less efficient than that in ordered aggregates. Based on the level of fluctuation in the transients of *rra*-P3HT (300±240 counts, which is equivalent to ~2-5 % of maximum intensity), the efficiency of energy transfer in disordered aggregated can be estimated as at least 10-20 times less than that in ordered aggregates.

The difference of the energy transfer efficiency between ordered and disordered morphology is more significant when the size of polymer domains increases from single chains to aggregates. In single chains of *rr*- and *rra*-P3HT, it was reported that energy transfer in ordered chains was at least twice more efficient than that in disordered chains (Chapter 7). The study of *rr*- and *rra*-P3HT aggregates herein showed that the difference between ordered and disordered aggregates could be at least 10-20 times. The important difference between the case of single chains and aggregates is the effect of interchain interactions. Therefore, these studies demonstrate that morphology plays more critical role for interchain energy transfer than intrachain energy transfer. It is reasonable to assume that the efficiency of energy transfer in disordered single chains and aggregates is not so different, and then these results further indicate that interchain energy transfer is more efficient than intrachain energy transfer in ordered domains.

In general, energy transfer in conjugated polymers is modeled based on the Förster Resonance Energy Transfer (FRET).[69,71,193] How to treat intra- and interchain energy transfer without under- or overestimating has been one of the central goals of these theoretical approaches. Hennebicq *et.al* reported that interchain energy transfer may be faster than intrachain energy transfer in the model system of polyindenofluorene endcapped with perylene derivatives.[193] They suggested that interchain energy transfer is faster as a result of electronic couplings and intrachain energy transfer is limited because

it occurs through hoppings of energy along a chain. Although our observations may agree with Hennebicq *et.al*, our results are not yet enough to fully discuss if inter- and intrachain energy transfer occurs through different mechanisms. However, the drastic decrease of fluorescence quantum yield from single chains to aggregates indicates the existence of strong interchain interactions in aggregates. Understanding how these interactions affect the electronic states of aggregates is an important next step to clarify the mechanism of why interchain energy transfer is faster than intrachain energy transfer.

8.4 CONCLUSION

By using the SVA assisted self-assembly of single conjugated polymer chains, *rr*- and *rra*-P3HT aggregates were successfully prepared. This demonstrated that the SVA can be used for assembling not only MEH-PPV but other polymer systems. The morphological order of aggregates reflected single chain conformations in some extent, and highly ordered aggregates were prepared from *rr*-P3HT, while disordered aggregates were prepared from *rra*-P3HT. A significant difference was observed for the fluorescence transients of *rr*- and *rra*-P3HT aggregates. All of *rr*-P3HT aggregates showed a discrete fluorescence blinking. On the other hand, *rra*-P3HT aggregates never showed a blinking but showed continuous decay of fluorescence intensity instead. These results further indicate that the morphological order is a critical parameter that controls energy transfers. Quantitative analysis of the fluorescence transients suggested that energy transfer in ordered aggregates is at least 10-20 times more efficient than that in disordered aggregates. By comparing these results to the case of single chains, it is clear that the difference of the energy transfer efficiency between ordered and disordered morphology is more significant when the size of polymer domains increases from single chains to aggregates. This suggests that morphology plays more critical role for interchain energy transfer than intrachain energy transfer, and indicate that interchain energy transfer is

more efficient than intrachain energy transfer. These may further imply that the energy transfer models in conjugated polymers require different mechanisms for intra- and interchain energy transfer.

Chapter 9: Outlook

The goal of this dissertation is to establish a quantitative understanding of conjugated polymer morphology and function. Single molecule spectroscopy was used to simplify the complexity and heterogeneity of systems, and the study was developed from single chains to aggregates. Some of my efforts undertaken with very talented colleagues were successful, and I believe we could make important discoveries and contributions in this field. At the same time, I am well aware of the limitations confronting conjugated polymer research and even more so of the way in which I can and must improve myself to obtain a clearer picture of the morphology and function of conjugated polymers. Having finished graduate school, I am much more frustrated with my ability and knowledge as a scientist than when I started because there is a huge gap between the truths I want to uncover and the limitations of what I can do at this point. Here I provide an outlook of what I believe to be the future of conjugated polymer research.

The biggest frustration is the limitation of the characterization methods I used to measure the morphology of conjugated polymers. As described in Chapter 2, single molecule fluorescence excitation polarization spectroscopy allows us to measure the degree of the alignment of chromophores along a chain. When all the chromophores within a chain are oriented along one direction, we obtain a modulation depth value (M) of one. On the other hand, when all the chromophores are oriented along completely random directions, M is zero. I referred to polymer chains with high M values as adopting a "highly ordered conformation" and those with low M values as adopting a "disordered conformation". "Is it sufficient to represent polymer morphology by a single number?" Unfortunately (frustratingly), the answer is no, and I illustrated the limitation of this value in fully representing polymer morphology (Figure 9.1). One way to obtain greater insight beyond this limitation is to seek help from theoretical simulations to generate

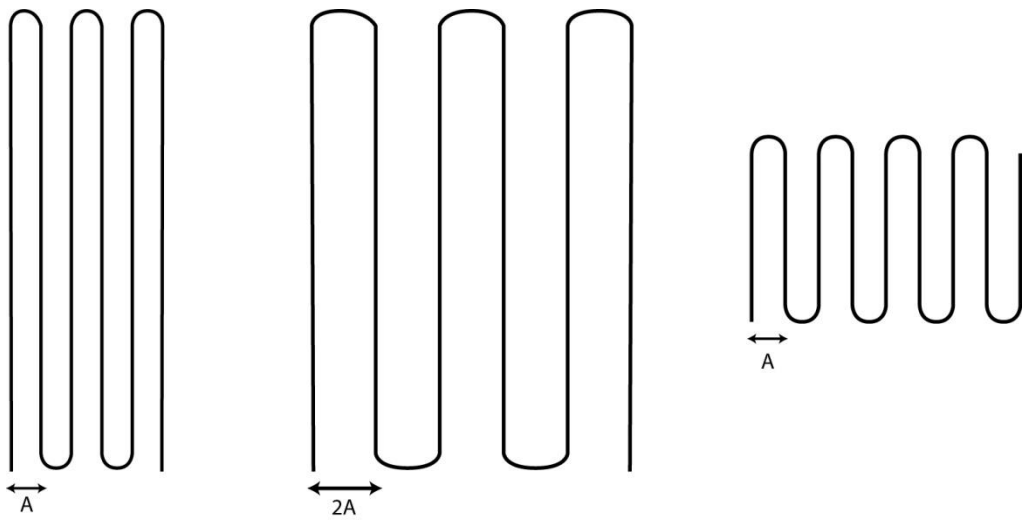

Figure 9.1: Simple cartoons of three different polymer chain conformations which all give the *M* value as one. As long as the direction of a polymer backbone is same, the difference in the number of chain bending or the distance between neighboring chains (shown as A or 2A) does not make a difference in the *M* value.

morphology that matches our observations. However, it would be ideal for us to invent a new experimental method that provides us further details regarding polymer morphology. Although this is challenging because the signal level from single polymer chains or aggregates is very low, further information about polymer morphology can provide a more robust understanding of the structure-property relationship and lead to the development of better models.

One good place to look for a hint may be in the research field of liquid crystals.[194-196] The order parameter is a construct used in this field to quantify the degree to which molecular axes are aligned along a particular reference direction. In polymer research, the order parameter is known as the second order of Herman's orientation function P_2. The orientation functions are Legendre polynomials, and the M value was derived from the second order of the orientation function. Because only P_2 is currently used to characterize polymer morphology, there are still possibilities to use higher-order orientation functions. Even with P_2, there is room for modification to obtain further information. In fact, in liquid crystals, it is possible to distinguish between nematic, smectic, and crystal phases by using the second order parameter. I have not yet discovered how to gain this information through the fluorescence of single chains, but doing so could be an important breakthrough.

Another limitation of single molecule spectroscopy is that it mostly relies on fluorescence signals. The measurement of absorption[197-199] or excitation spectra[200-202] at the single molecule level was recently demonstrated, and this could be a great breakthrough in understanding conjugated polymers. Still, this is not enough. The ideal measurement would be single molecule X-ray diffraction spectroscopy (XRD). Needless to say, the scattering from single molecules is simply too low for X-ray diffraction spectroscopy. However, the crystal size requirement for XRD has continued to decrease

with recent developments in instrumentation, and there might be a brilliant trick yet to be discovered to achieve single molecule XRD. A number of research fields will benefit from such a technique. Besides a breakthrough in instrumentations, an immediate valid approach might be the preparation of homogenous solid state samples using any type of host framework. There are reports that show such robust molecular frameworks can be used to precisely tune the molecular arrangements of dyes, conjugated oligomers and so on.[203,204] This approach might provide new prospects for understanding the structure-function relationship in a relatively short time.

Finally, it can never been forgotten that it is necessary to bridge our knowledge from the single molecule level toward the bulk level. In conjugated polymers, it is necessary to use single molecule spectroscopy to minimize the complexity of problems and to sort out the heterogeneity of objects. There have been many important discoveries in the last 15 years, and it is time to merge them with the study of bulk films. It is not a simple task, and this has to be done carefully with "no rush". Fortunately, we have invented a method through which single chains can be slowly assembled into aggregates (Chapter 5 and 8). This has enabled us to make a transition from single chains to the bulk level with a minimum increase in complexity and heterogeneity. Applying this aggregation method to various materials will lead to a series of new discoveries. This could finally enable us to find the "key" to controlling the morphology and function of bulk solid conjugated polymer films.

There are a plenty of challenges, none of which is easy. That is why life is so much fun.

Bibliography

(1) Rossky, P. J.; Walker, G. C. Paul F. Barbara (1953~2010). *Science* **2010**, *330*, 1191.

(2) Masuhara, H.; Furube, A. With Deep Condolence to Prof. Paul F. Barbara of University of Texas at Austin. *Photochemistry* **2011**, *42*, 41-42.

(3) http://www.utexas.edu/faculty/council/2011-2012/memorials/barbara.pdf

(4) Tabor, R. *Science and Consciousness*; BookSurge Publishing: Austin TX, USA, 2008.

(5) Sniegowski, P. D.; Lenski, R. E. Mutation and Adaptation: The Directed Mutation Controversy in Evolutionary Perspective. *Annu. Rev. Ecol. Evol. Syst.* **1995**, *26*, 553-578.

(6) Foster, P. L. Adaptive Mutation - The Uses of Adversity. *Annu. Rev. Microbiol.* **1993**, *47*, 467-504.

(7) Brisson, D. The directed mutation controversy in an evolutionary context. *Crit. Rev. Microbiol.* **2003**, *29*, 25-35.

(8) Heidenreich, E. Adaptive mutation in Saccharomyces cerevisiae. *Crit. Rev. Biochem. Mol. Biol.* **2007**, *42*, 285-311.

(9) Arias, A. C.; MacKenzie, J. D.; McCulloch, I.; Rivnay, J.; Salleo, A. Materials and Applications for Large Area Electronics: Solution-Based Approaches. *Chem. Rev.* **2010**, *110*, 3-24.

(10) Hoppe, H.; Sariciftci, N. S. Organic solar cells: An overview. *J. Mater. Res.* **2004**, *19*, 1924-1945.

(11) Gunes, S.; Neugebauer, H.; Sariciftci, N. S. Conjugated polymer-based organic solar cells. *Chem. Rev.* **2007**, *107*, 1324-1338.

(12) Coakley, K. M.; McGehee, M. D. Conjugated polymer photovoltaic cells. *Chem. Mater.* **2004**, *16*, 4533-4542.

(13) Friend, R. H.; Gymer, R. W.; Holmes, A. B.; Burroughes, J. H.; Marks, R. N.; Taliani, C.; Bradley, D. D. C.; Dos Santos, D. A.; Bredas, J. L.; Logdlund, M.; Salaneck, W. R. Electroluminescence in conjugated polymers. *Nature* **1999**, *397*, 121-128.

(14) Gustafsson, G.; Cao, Y.; Treacy, G. M.; Klavetter, F.; Colaneri, N.; Heeger, A. J. Flexible light-emitting-diodes made from soluble conducting polymers. *Nature* **1992**, *357*, 477-479.

(15) Burroughes, J. H.; Bradley, D. D. C.; Brown, A. R.; Marks, R. N.; Mackay, K.; Friend, R. H.; Burns, P. L.; Holmes, A. B. LIGHT-EMITTING-DIODES BASED ON CONJUGATED POLYMERS. *Nature* **1990**, *347*, 539-541.

(16) Dimitrakopoulos, C. D.; Mascaro, D. J. Organic thin-film transistors: A review of recent advances. *IBM J. Res. Dev.* **2001**, *45*, 11-27.

(17) Dimitrakopoulos, C. D.; Malenfant, P. R. L. Organic thin film transistors for large area electronics. *Adv. Mater.* **2002**, *14*, 99-+.

(18) Brédas, J.-L.; Beljonne, D.; Coropceanu, V.; Cornil, J. Charge-Transfer and Energy-Transfer Processes in π-Conjugated Oligomers and Polymers: A Molecular Picture. *Chem. Rev.* **2004**, *104*, 4971-5004.

(19) Hoeben, F. J. M.; Jonkheijm, P.; Meijer, E. W.; Schenning, A. About supramolecular assemblies of pi-conjugated systems. *Chem. Rev.* **2005**, *105*, 1491-1546.

(20) Kline, R. J.; McGehee, M. D. Morphology and charge transport in conjugated polymer. *Polym. Rev.* **2006**, *46*, 27-45.

(21) Wong, L. Y.; Png, R. Q.; Silva, F. B. S.; Chua, L. L.; Repaka, D. V. M.; Shi-Chen; Gao, X. Y.; Ke, L.; Chua, S. J.; Wee, A. T. S.; Ho, P. K. H. Interplay of Processing, Morphological Order, and Charge-Carrier Mobility in Polythiophene Thin Films Deposited by Different Methods: Comparison of Spin-Cast, Drop-Cast, and Inkjet-Printed Films. *Langmuir* **2010**, *26*, 15494-15507.

(22) Nguyen, T. Q.; Schwartz, B. J.; Schaller, R. D.; Johnson, J. C.; Lee, L. F.; Haber, L. H.; Saykally, R. J. Near-field scanning optical microscopy (NSOM) studies of the relationship between interchain interactions, morphology, photodamage, and energy transport in conjugated polymer films. *J. Phys. Chem. B* **2001**, *105*, 5153-5160.

(23) Nguyen, T. Q.; Yee, R. Y.; Schwartz, B. J. Solution processing of conjugated polymers: the effects of polymer solubility on the morphology and electronic properties of semiconducting polymer films. *J. Photochem. Photobiol., A* **2001**, *144*, 21-30.

(24) Tsao, H. N.; Cho, D.; Andreasen, J. W.; Rouhanipour, A.; Breiby, D. W.; Pisula, W.; Mullen, K. The Influence of Morphology on High-Performance Polymer Field-Effect Transistors. *Adv. Mater.* **2009**, *21*, 209-+.

(25) Wu, Z.; Petzold, A.; Henze, T.; Thurn-Albrecht, T.; Lohwasser, R. H.; Sommer, M.; Thelakkat, M. Temperature and Molecular Weight Dependent Hierarchical Equilibrium Structures in Semiconducting Poly(3-hexylthiophene). *Macromolecules* **2010**, *43*, 4646-4653.

(26) Koynov, K.; Bahtiar, A.; Ahn, T.; Cordeiro, R. M.; Horhold, H. H.; Bubeck, C. Molecular weight dependence of chain orientation and optical constants of thin films of the conjugated polymer MEH-PPV. *Macromolecules* **2006**, *39*, 8692-8698.

(27) Verilhac, J. M.; LeBlevennec, G.; Djurado, D.; Rieutord, F.; Chouiki, M.; Travers, J. P.; Pron, A. Effect of macromolecular parameters and processing conditions on supramolecular organisation, morphology and electrical transport properties in thin layers of regioregular poly(3-hexylthiophene). *Synth. Met.* **2006**, *156*, 815-823.

(28) Menon, A.; Dong, H. P.; Niazimbetova, Z. I.; Rothberg, L. J.; Galvin, M. E. Polydispersity effects on conjugated polymer light-emitting diodes. *Chem. Mater.* **2002**, *14*, 3668-3675.

(29) Koppe, M.; Brabec, C. J.; Heiml, S.; Schausberger, A.; Duffy, W.; Heeney, M.; McCulloch, I. Influence of Molecular Weight Distribution on the Gelation of P3HT and Its Impact on the Photovoltaic Performance. *Macromolecules* **2009**, *42*, 4661-4666.

(30) Surin, M.; Hennebicq, E.; Ego, C.; Marsitzky, D.; Grimsdale, A. C.; Mullen, K.; Bredas, J. L.; Lazzaroni, R.; Leclere, P. Correlation between the microscopic morphology and the solid-state photoluminescence properties in fluorene-based polymers and copolymers. *Chem. Mater.* **2004**, *16*, 994-1001.

(31) Kim, Y.; Cook, S.; Tuladhar, S. M.; Choulis, S. A.; Nelson, J.; Durrant, J. R.; Bradley, D. D. C.; Giles, M.; Mcculloch, I.; Ha, C. S.; Ree, M. A strong

regioregularity effect in self-organizing conjugated polymer films and high-efficiency polythiophene: fullerene solar cells. *Nature Mater.* **2006**, *5*, 197-203.

(32) Schuettfort, T.; Watts, B.; Thomsen, L.; Lee, M.; Sirringhaus, H.; McNeill, C. R. Microstructure of Polycrystalline PBTTT Films: Domain Mapping and Structure Formation. *ACS Nano* **2012**, *6*, 1849-1864.

(33) Kuehn, S.; Pingel, P.; Breusing, M.; Fischer, T.; Stumpe, J.; Neher, D.; Elsaesser, T. High-Resolution Near-Field Optical Investigation of Crystalline Domains in Oligomeric PQT-12 Thin Films. *Adv. Funct. Mater.* **2011**, *21*, 860-868.

(34) Rivnay, J.; Noriega, R.; Northrup, J. E.; Kline, R. J.; Toney, M. F.; Salleo, A. Structural origin of gap states in semicrystalline polymers and the implications for charge transport. *Phys. Rev. B* **2011**, *83*.

(35) Moons, E. Conjugated polymer blends: linking film morphology to performance of light emitting diodes and photodiodes. *J. Phys.: Condens. Matter* **2002**, *14*, 12235-12260.

(36) Kulkarni, A. P.; Jenekhe, S. A. Blue light-emitting diodes with good spectral stability based on blends of poly(9,9-dioctylfluorene): Interplay between morphology, photophysics, and device performance. *Macromolecules* **2003**, *36*, 5285-5296.

(37) Chappell, J.; Lidzey, D. G.; Jukes, P. C.; Higgins, A. M.; Thompson, R. L.; O'Connor, S.; Grizzi, I.; Fletcher, R.; O'Brien, J.; Geoghegan, M.; Jones, R. A. L. Correlating structure with fluorescence emission in phase-separated conjugated-polymer blends. *Nature Mater.* **2003**, *2*, 616-621.

(38) Hoppe, H.; Glatzel, T.; Niggemann, M.; Schwinger, W.; Schaeffler, F.; Hinsch, A.; Lux-Steiner, M. C.; Sariciftci, N. S. Efficiency limiting morphological factors of MDMO-PPV : PCBM plastic solar cells. *Thin Solid Films* **2006**, *511*, 587-592.

(39) Groves, C.; Reid, O. G.; Ginger, D. S. Heterogeneity in Polymer Solar Cells: Local Morphology and Performance in Organic Photovoltaics Studied with Scanning Probe Microscopy. *Acc. Chem. Res.* **2010**, *43*, 612-620.

(40) Barbara, P. F.; Gesquiere, A. J.; Park, S. J.; Lee, Y. J. Single-molecule spectroscopy of conjugated polymers. *Accounts of Chemical Research* **2005**, *38*, 602-610.

(41) Laquai, F.; Park, Y. S.; Kim, J. J.; Basche, T. Excitation Energy Transfer in Organic Materials: From Fundamentals to Optoelectronic Devices. *Macromol. Rapid Commun.* **2009**, *30*, 1203-1231.

(42) Lupton, J. M. Single-Molecule Spectroscopy for Plastic Electronics: Materials Analysis from the Bottom-Up. *Adv. Mater.* **2010**, *22*, 1689-1721.

(43) Fu, Y.; Lakowicz, J. R. Spectroscopy: A closer look at polymer annealing. *Nature* **2011**, *472*, 178-179.

(44) Bolinger, J. C.; Traub, M. C.; Adachi, T.; Barbara, P. F. Ultralong-Range Polaron-Induced Quenching of Excitons in Isolated Conjugated Polymers. *Science* **2011**, *331*, 565-567.

(45) Sumpter, B. G.; Kumar, P.; Mehta, A.; Barnes, M. D.; Shelton, W. A.; Harrison, R. J. Computational study of the structure, dynamics, and photophysical properties of conjugated polymers and oligomers under nanoscale confinement. *J. Phys. Chem. B* **2005**, *109*, 7671-7685.

(46) Barford, W.; Lidzey, D. G.; Makhov, D. V.; Meijer, A. J. H. Exciton localization in disordered poly(3-hexylthiophene). *J. Chem. Phys.* **2010**, *133*, 0445041-0445046.

(47) Hu, D. H.; Yu, J.; Wong, K.; Bagchi, B.; Rossky, P. J.; Barbara, P. F. Collapse of stiff conjugated polymers with chemical defects into ordered, cylindrical conformations. *Nature* **2000**, *405*, 1030-1033.

(48) Vogelsang, J.; Lupton, J. M. Solvent Vapor Annealing of Single Conjugated Polymer Chains: Building Organic Optoelectronic Materials from the Bottom Up. *J. Phys. Chem. Lett* **2012**, *3*, 1503-1513.

(49) Bassler, H.; Schweitzer, B. Site-Selective Fluorescence Spectroscopy of Conjugated Polymers and Oligomers. *Acc. Chem. Res.* **1998**, *32*, 173-182.

(50) Lupton, J. M. Chromophores in Conjugated Polymers—All Straight? *Chemphyschem* **2012**, *13*, 901-907.

(51) Schwartz, B. J. Conjugated polymers as molecular materials: How chain conformation and film morphology influence energy transfer and interchain interactions. *Annu Rev Phys Chem* **2003**, *54*, 141-172.

(52) Traiphol, R.; Sanguansat, P.; Srikhirin, T.; Kerdcharoen, T.; Osotchan, T. Spectroscopic study of photophysical change in collapsed coils of conjugated polymers: Effects of solvent and temperature. *Macromolecules* **2006**, *39*, 1165-1172.

(53) Collison, C. J.; Rothberg, L. J.; Treemaneekarn, V.; Li, Y. Conformational effects on the photophysics of conjugated polymers: A two species model for MEH-PPV spectroscopy and dynamics. *Macromolecules* **2001**, *34*, 2346-2352.

(54) Levine, I. N. *Molecular spectroscopy*; Wiley: New York, USA, 1975.

(55) Atkins, P.; Friedman, R. *Molecular Quantum Mechanics*; Oxford university press: New York, USA, 2005.

(56) Byron, C. M.; Werner, T. C. Experiments in synchronous fluorescence spectroscopy for the undergraduate instrumental chemistry course. *J. Chem. Educ.* **1991**, *68*, 433.

(57) Cornil, J.; Beljonne, D.; Calbert, J. P.; Brédas, J. L. Interchain Interactions in Organic π-Conjugated Materials: Impact on Electronic Structure, Optical Response, and Charge Transport. *Adv. Mater.* **2001**, *13*, 1053-1067.

(58) Clark, J.; Silva, C.; Friend, R. H.; Spano, F. C. Role of intermolecular coupling in the photophysics of disordered organic semiconductors: Aggregate emission in regioregular polythiophene. *Phys. Rev. Lett.* **2007**, *98*.

(59) Cook, S.; Furube, A.; Katoh, R. Analysis of the excited states of regioregular polythiophene P3HT. *Energy Environ. Sci.* **2008**, *1*, 294-299.

(60) Gaab, K. M.; Bardeen, C. J. Wavelength and temperature dependence of the femtosecond pump-probe anisotropies in the conjugated polymer MEH-PPV: Implications for energy-transfer dynamics. *J. Phys. Chem. B* **2004**, *108*, 4619-4626.

(61) Brown, P. J.; Thomas, D. S.; Kohler, A.; Wilson, J. S.; Kim, J. S.; Ramsdale, C. M.; Sirringhaus, H.; Friend, R. H. Effect of interchain interactions on the absorption and emission of poly(3-hexylthiophene). *Phys. Rev. B* **2003**, *67*, 064203.

(62) Samuel, I. D. W.; Magnani, L.; Rumbles, G.; Murray, K.; Stone, B. M.; Moratti, S. C.; Holmes, A. B. Photoluminescence in poly(3-hexylthiophene). *Proc. SPIE* **1997**, *3145*, 163-170.

(63) Greenham, N. C.; Samuel, I. D. W.; Hayes, G. R.; Phillips, R. T.; Kessener, Y. A. R. R.; Moratti, S. C.; Holmes, A. B.; Friend, R. H. Measurement of Absolute Photoluminescence Quantum Efficiencies in Conjugated Polymers. *Chem. Phys. Lett.* **1995**, *241*, 89-96.

(64) Li, Y. N.; Vamvounis, G.; Holdcroft, S. Tuning optical properties and enhancing solid-state emission of poly(thiophene)s by molecular control: A postfunctionalization approach. *Macromolecules* **2002**, *35*, 6900-6906.

(65) Aasmundtveit, K. E.; Samuelsen, E. J.; Mammo, W.; Svensson, M.; Andersson, M. R.; Pettersson, L. A. A.; Inganas, O. Structural ordering in phenyl-substituted polythiophenes. *Macromolecules* **2000**, *33*, 5481-5489.

(66) Theander, M.; Svensson, M.; Ruseckas, A.; Zigmantas, D.; Sundstrom, V.; Andersson, M. R.; Inganas, O. High luminescence from a substituted polythiophene in a solvent with low solubility. *Chem. Phys. Lett.* **2001**, *337*, 277-283.

(67) Brazard, J.; Ono, R. J.; Bielawski, C. W.; Barbara, P. F.; Vanden Bout, D. A. Mimicking Conjugated Polymer Thin-Film Photophysics with a Well-Defined Triblock Copolymer in Solution. *J. Phys. Chem. B* **2012**.

(68) Guo, J. M.; Ohkita, H.; Benten, H.; Ito, S. Near-IR Femtosecond Transient Absorption Spectroscopy of Ultrafast Polaron and Triplet Exciton Formation in Polythiophene Films with Different Regioregularities. *J. Am. Chem. Soc.* **2009**, *131*, 16869-16880.

(69) Westenhoff, S.; Daniel, C.; Friend, R. H.; Silva, C.; Sundstrom, V.; Yartsev, A. Exciton migration in a polythiophene: Probing the spatial and energy domain by line-dipole Forster-type energy transfer. *J. Chem. Phys.* **2005**, *122*.

(70) Hwang, I.; Scholes, G. D. Electronic Energy Transfer and Quantum-Coherence in pi-Conjugated Polymers. *Chem. Mater.* **2011**, *23*, 610-620.

(71) Wong, K. F.; Bagchi, B.; Rossky, P. J. Distance and orientation dependence of excitation transfer rates in conjugated systems: Beyond the Forster theory. *J. Phys. Chem. A* **2004**, *108*, 5752-5763.

(72) For several papers which deal with morphology of conjugated polymer and related issues, see the special issues of Mullen, K.; Swager, T. M., Advanced Polymer Design and Synthesis, Acc. Chem. Res. 2008, 41, and Bredas, J.-L.; Durrant, J. R., Organic Photovoltaics, Acc. Chem. Res. 2009, 42

(73) Bout, D. A. V.; Kerimo, J.; Higgins, D. A.; Barbara, P. F. Near-field optical studies of thin-film mesostructured organic materials. *Acc. Chem. Res.* **1997**, *30*, 204-212.

(74) Link, S.; Hu, D.; Chang, W. S.; Scholes, G. D.; Barbara, P. F. Nematic Solvation of Segmented Polymer Chains. *Nano Letters* **2005**, *5*, 1757-1760.

(75) Barbara, P. F.; Chang, W. S.; Link, S.; Scholes, G. D.; Yethiraj, A. Structure and dynamics of conjugated polymers in liquid crystalline solvents. *Annu. Rev. Phys. Chem.* **2007**, *58*, 565-584.

(76) Hu, D.; Yu, J.; Padmanaban, G.; Ramakrishanan, S.; Barbara, P. F. Spatial Confinement of Exciton Transfer and the Role of Conformational Order in Organic Nanoparticles. *Nano Letters* **2002**, *2*, 1121-1124.

(77) Wong, K. F.; Skaf, M. S.; Yang, C. Y.; Rossky, P. J.; Bagchi, B.; Hu, D. H.; Yu, J.; Barbara, P. F. Structural and electronic characterization of chemical and conformational defects in conjugated polymers. *J. Phys. Chem. B* **2001**, *105*, 6103-6107.

(78) The number average molecular weight and PDI were reported by Polymer Source Inc. and measured by absolute GPC using triple detection method.

(79) The number average molecular weight and PDI were reported by American Dye Source Inc. and measured by absolute GPC using triple detection method.

(80) Axelrod, D. Fluorescence Polarization Microscopy. *Methods in Cell Biology* **1989**, *30*, 333-352.

(81) Forkey, J. N.; Quinlan, M. E.; Goldman, Y. E. Protein structural dynamics by single-molecule fluorescence polarization. *Prog. Biophys. Mol. Biol.* **2000**, *74*, 1-35.

(82) Higgins, D. A.; VandenBout, D. A.; Kerimo, J.; Barbara, P. F. Polarization-modulation near-field scanning optical microscopy of mesostructured materials. *J. Phys. Chem.* **1996**, *100*, 13794-13803.

(83) Siano, D. B.; Metzler, D. E. BAND SHAPES OF ELECTRONIC SPECTRA OF COMPLEX MOLECULES. *Journal of Chemical Physics* **1969**, *51*, 1856-&.

(84) Liu, C.; Muthukumar, M. Langevin dynamics simulations of early-stage polymer nucleation and crystallization. *J. Chem. Phys.* **1998**, *109*, 2536-2542.

(85) Allen, M. P.; Tildesley, D. J. *Computer Simulations of Liquids*; Clarendon, Oxford, 1987.

(86) Orion, I.; Buisson, J. P.; Lefrant, S. Spectroscopic studies of polaronic and bipolaronic species in n-doped poly(paraphenylenevinylene). *Physical Review B* **1998**, *57*, 7050-7065.

(87) Noguchi, H.; Yoshikawa, K. Morphological variation in a collapsed single homopolymer chain. *Journal of Chemical Physics* **1998**, *109*, 5070-5077.

(88) Granstrom, M.; Petritsch, K.; Arias, A. C.; Lux, A.; Andersson, M. R.; Friend, R. H. Laminated fabrication of polymeric photovoltaic diodes. *Nature* **1998**, *395*, 257-260.

(89) Sirringhaus, H.; Brown, P. J.; Friend, R. H.; Nielsen, M. M.; Bechgaard, K.; Langeveld-Voss, B. M. W.; Spiering, A. J. H.; Janssen, R. A. J.; Meijer, E. W.; Herwig, P.; de Leeuw, D. M. Two-dimensional charge transport in self-organized, high-mobility conjugated polymers. *Nature* **1999**, *401*, 685-688.

(90) Nguyen, T. Q.; Martini, I. B.; Liu, J.; Schwartz, B. J. Controlling interchain interactions in conjugated polymers: The effects of chain morphology on exciton-exciton annihilation and aggregation in MEH-PPV films. *J. Phys. Chem. B* **2000**, *104*, 237-255.

(91) Ma, W. L.; Yang, C. Y.; Gong, X.; Lee, K.; Heeger, A. J. Thermally stable, efficient polymer solar cells with nanoscale control of the interpenetrating network morphology. *Adv. Funct. Mater.* **2005**, *15*, 1617-1622.

(92) Kline, R. J.; McGehee, M. D.; Kadnikova, E. N.; Liu, J. S.; Frechet, J. M. J.; Toney, M. F. Dependence of regioregular poly(3-hexylthiophene) film morphology and field-effect mobility on molecular weight. *Macromolecules* **2005**, *38*, 3312-3319.

(93) Reyes-Reyes, M.; Kim, K.; Carroll, D. L. High-efficiency photovoltaic devices based on annealed poly(3-hexylthiophene) and 1-(3-methoxycarbonyl)-propyl-1-phenyl-(6,6)C-61 blends. *Appl. Phys. Lett.* **2005**, *87*.

(94) Yang, X. N.; Loos, J.; Veenstra, S. C.; Verhees, W. J. H.; Wienk, M. M.; Kroon, J. M.; Michels, M. A. J.; Janssen, R. A. J. Nanoscale morphology of high-performance polymer solar cells. *Nano Lett.* **2005**, *5*, 579-583.

(95) Hor, A. M.; Loutfy, R. O. Solvent-Induced Dimorphic Transformation in Magnesium Phthalocyanine and Its Effect on the Photoactivity. *Thin Solid Films* **1983**, *106*, 291-301.

(96) Law, K. Y. Organic Photoconductive Materials - Recent Trends and Developments. *Chem. Rev.* **1993**, *93*, 449-486.

(97) Miller, S.; Fanchini, G.; Lin, Y. Y.; Li, C.; Chen, C. W.; Su, W. F.; Chhowalla, M. Investigation of nanoscale morphological changes in organic photovoltaics during solvent vapor annealing. *J. Mater. Chem.* **2008**, *18*, 306-312.

(98) Muls, B.; Uji-i, H.; Melnikov, S.; Moussa, A.; Verheijen, W.; Soumillion, J. P.; Josemon, J.; Müllen, K.; Hofkens, J. Direct measurement of the end-to-end distance of individual polyfluorene polymer chains. *Chemphyschem* **2005**, *6*, 2286-2294.

(99) Woll, D.; Braeken, E.; Deres, A.; De Schryver, F. C.; Uji-i, H.; Hofkens, J. Polymers and single molecule fluorescence spectroscopy, what can we learn? *Chem. Soc. Rev.* **2009**, *38*, 313-328.

(100) Adachi, T.; Brazard, J.; Chokshi, P.; Bolinger, J. C.; Ganesan, V.; Barbara, P. F. Highly Ordered Single Conjugated Polymer Chain Rod Morphologies *J. Phys. Chem. C* **2010**, *114*, 20896-20902.

(101) Gesquiere, A. J.; Lee, Y. J.; Yu, J.; Barbara, P. F. Single Molecule Modulation Spectroscopy of Conjugated Polymers. *J. Phys. Chem. B* **2005**, *109*, 12366-12371.

(102) Nguyen, T. Q.; Doan, V.; Schwartz, B. J. Conjugated polymer aggregates in solution: Control of interchain interactions. *J. Chem. Phys.* **1999**, *110*, 4068-4078.

(103) Aharon, E.; Breuer, S.; Jaiser, F.; Kohler, A.; Frey, G. L. Effect of the solvent on the conformation of isolated MEH-PPV chains intercalated into SnS2. *Chemphyschem* **2008**, *9*, 1430-1436.

(104) Chow, T. S. Molecular Interpretation of the Glass-Transition Temperature of Polymer-Diluent Systems. *Macromolecules* **1980**, *13*, 362-364.

(105) Doumenc, F.; Bodiguel, H.; Guerrier, B. Physical aging of glassy PMMA/toluene films: Influence of drying/swelling history. *Eur. Phys. J. E Soft Matter* **2008**, *27*, 3-11.

(106) Woell, D.; Uji-I, H.; Schnitzler, T.; Hotta, J. I.; Dedecker, P.; Herrmann, A.; De Schryver, F. C.; Muellen, K.; Hofkens, J. Radical polymerization tracked by single molecule spectroscopy. *Angew. Chem. Int. Ed.* **2008**, *47*, 783-787.

(107) Lin, H. Z.; Tian, Y. X.; Zapadka, K.; Persson, G.; Thomsson, D.; Mirzov, O.; Larsson, P. O.; Widengren, J.; Scheblykin, I. G. Fate of Excitations in Conjugated

Polymers: Single-Molecule Spectroscopy Reveals Nonemissive "Dark" Regions in MEH-PPV Individual Chains. *Nano Lett.* **2009**, *9*, 4456-4461.

(108) Mirzov, O.; Bloem, R.; Hania, P. R.; Thomsson, D.; Lin, H.; Scheblykin, I. G. Polarization Portraits of Single Multichromophoric Systems: Visualizing Conformation and Energy Transfer. *Small* **2009**, *5*, 1877-1888.

(109) Craig, I. M.; Tassone, C. J.; Tolbert, S. H.; Schwartz, B. J. Second-harmonic generation in conjugated polymer films: A sensitive probe of how bulk polymer crystallinity changes with spin speed. *J. Chem. Phys.* **2010**, *133*, 044901.

(110) Bolinger, J. C.; Fradkin, L.; Lee, K. J.; Palacios, R. E.; Barbara, P. F. Light-assisted deep-trapping of holes in conjugated polymers. *Proceedings of the National Academy of Sciences of the United States of America* **2009**, *106*, 1342-1346.

(111) Lim, S. H.; Bjorklund, T. G.; Bardeen, C. J. The role of long-lived dark states in the photoluminescence dynamics of poly(phenylene vinylene) conjugated polymers. II. Excited-state quenching versus ground-state depletion. *Journal of Chemical Physics* **2003**, *118*, 4297-4305.

(112) Bolinger, J.; Lee, K. J.; Palacios, R. E.; Barbara, P. F. Detailed Investigation of Light Induced Charge Injection into a Single Conjugated Polymer Chain. *Journal of Physical Chemistry C* **2008**, *112*, 18608-18615.

(113) Salleo, A.; Street, R. A. Light-induced bias stress reversal in polyfluorene thin-film transistors. *Journal of Applied Physics* **2003**, *94*, 471-479.

(114) Adams, D. M.; Kerimo, J.; O'Connor, D. B.; Barbara, P. F. Spatial imaging of singlet energy migration in perylene bis(phenethylimide) thin films. *Journal of Physical Chemistry A* **1999**, *103*, 10138-10143.

(115) Markov, D. E.; Amsterdam, E.; Blom, P. W. M.; Sieval, A. B.; Hummelen, J. C. Accurate measurement of the exciton diffusion length in a conjugated polymer using a heterostructure with a side-chain cross-linked fullerene layer. *J. Phys. Chem. A* **2005**, *109*, 5266-5274.

(116) Betzig, E.; Patterson, G. H.; Sougrat, R.; Lindwasser, O. W.; Olenych, S.; Bonifacino, J. S.; Davidson, M. W.; Lippincott-Schwartz, J.; Hess, H. F. Imaging intracellular fluorescent proteins at nanometer resolution. *Science* **2006**, *313*, 1642-1645.

(117) Moerner, W. E. New directions in single-molecule imaging and analysis. *Proceedings of the National Academy of Sciences of the United States of America* **2007**, *104*, 12596-12602.

(118) Rust, M. J.; Bates, M.; Zhuang, X. W. Sub-diffraction-limit imaging by stochastic optical reconstruction microscopy (STORM). *Nature Methods* **2006**, *3*, 793-795.

(119) Thompson, R. E.; Larson, D. R.; Webb, W. W. Precise nanometer localization analysis for individual fluorescent probes. *Biophys. J.* **2002**, *82*, 2775-2783.

(120) Yu, J.; Song, N. W.; McNeill, J. D.; Barbara, P. F. Efficient exciton quenching by hole polarons in the conjugated polymer MEH-PPV. *Israel Journal of Chemistry* **2004**, *44*, 127-132.

(121) Yu, J.; Hu, D. H.; Barbara, P. F. Unmasking electronic energy transfer of conjugated polymers by suppression of O-2 quenching. *Science* **2000**, *289*, 1327-1330.

(122) Kim, D. Y.; Grey, J. K.; Barbara, P. F. A detailed single molecule spectroscopy study of the vibronic states and energy transfer pathways of the conjugated polymer MEH-PPV. *Synth. Met.* **2006**, *156*, 336-345.

(123) Dykstra, T. E.; Hennebicq, E.; Beljonne, D.; Gierschner, J.; Claudio, G.; Bittner, E. R.; Knoester, J.; Scholes, G. D. Conformational Disorder and Ultrafast Exciton Relaxation in PPV-family Conjugated Polymers. *J. Phys. Chem. B* **2009**, *113*, 656-667.

(124) Collini, E.; Scholes, G. D. Coherent Intrachain Energy Migration in a Conjugated Polymer at Room Temperature. *Science* **2009**, *323*, 369-373.

(125) Wang, H. L.; MacDiarmid, A. G.; Wang, Y. Z.; Gebler, D. D.; Epstein, A. J. Application of polyaniline (emeraldine base, EB) in polymer light-emitting devices. *Synth. Met.* **1996**, *78*, 33-37.

(126) Shaheen, S. E.; Brabec, C. J.; Sariciftci, N. S.; Padinger, F.; Fromherz, T.; Hummelen, J. C. 2.5% efficient organic plastic solar cells. *Appl. Phys. Lett.* **2001**, *78*, 841-843.

(127) Bardeen, C. Exciton Quenching and Migration in Single Conjugated Polymers. *Science* **2011**, *331*, 544-545.

(128) Hide, F.; DiazGarcia, M. A.; Schwartz, B. J.; Heeger, A. J. New developments in the photonic applications of conjugated polymers. *Acc. Chem. Res.* **1997**, *30*, 430-436.

(129) VandenBout, D. A.; Yip, W. T.; Hu, D. H.; Fu, D. K.; Swager, T. M.; Barbara, P. F. Discrete intensity jumps and intramolecular electronic energy transfer in the spectroscopy of single conjugated polymer molecules. *Science* **1997**, *277*, 1074-1077.

(130) Habuchi, S.; Onda, S.; Vacha, M. Mapping the emitting sites within a single conjugated polymer molecule. *Chem. Commun.* **2009**, 4868-4870.

(131) Vogelsang, J.; Brazard, J.; Adachi, T.; Bolinger, J. C.; Barbara, P. F. Watching the Annealing Process One Polymer Chain at a Time. *Angew. Chem. Int. Ed.* **2011**, *50*, 2257-2261.

(132) Lifshitz, I. M.; Slyozov, V. V. The kinetics of precipitation from supersaturated solid solutions. *J. Phys. Chem. Solids* **1961**, *19*, 35-50.

(133) Brandrup, J.; Immergut, E. H.; Grulke, A. A.; R., B. D. *Polymer Handbook*, 4th ed.; Wiley, New York, 1999, 1999.

(134) Peng, J.; Kim, D. H.; Knoll, W.; Xuan, Y.; Li, B. Y.; Han, Y. C. Morphologies in solvent-annealed thin films of symmetric diblock copolymer. *J. Chem. Phys.* **2006**, *125*, 8.

(135) Grey, J. K.; Kim, D. Y.; Norris, B. C.; Miller, W. L.; Barbara, P. F. Size-dependent spectroscopic properties of conjugated polymer nanoparticles. *J. Phys. Chem. B* **2006**, *110*, 25568-25572.

(136) Szymanski, C.; Wu, C. F.; Hooper, J.; Salazar, M. A.; Perdomo, A.; Dukes, A.; McNeill, J. Single molecule nanoparticles of the conjugated polymer MEH-PPV, preparation and characterization by near-field scanning optical microscopy. *J. Phys. Chem. B* **2005**, *109*, 8543-8546.

(137) Samuel, I. D. W.; Turnbull, G. A. Organic semiconductor lasers. *Chem. Rev.* **2007**, *107*, 1272-1295.

(138) van der Veen, M. H.; de Boer, B.; Stalmach, U.; van de wetering, K. I.; Hadziioannou, G. Donor-acceptor diblock copolymers based on PPV and C-60: Synthesis, thermal properties, and morphology. *Macromolecules* **2004**, *37*, 3673-3684.

(139) Lindner, S. M.; Huttner, S.; Chiche, A.; Thelakkat, M.; Krausch, G. Charge separation at self-assembled nanostructured bulk interface in block copolymers. *Angew. Chem.-Int. Edit.* **2006**, *45*, 3364-3368.

(140) Zhang, Q. L.; Cirpan, A.; Russell, T. P.; Emrick, T. Donor-Acceptor Poly(thiophene-block-perylene diimide) Copolymers: Synthesis and Solar Cell Fabrication. *Macromolecules* **2009**, *42*, 1079-1082.

(141) Yang, C.; Lee, J. K.; Heeger, A. J.; Wudl, F. Well-defined donor-acceptor rod-coil diblock copolymers based on P3HT containing C-60: the morphology and role as a surfactant in bulk-heterojunction solar cells. *J. Mater. Chem.* **2009**, *19*, 5416-5423.

(142) Clarke, T. M.; Durrant, J. R. Charge Photogeneration in Organic Solar Cells. *Chem. Rev.* **2010**, *110*, 6736-6767.

(143) Sirringhaus, H. Device physics of Solution-processed organic field-effect transistors. *Adv. Mater.* **2005**, *17*, 2411-2425.

(144) Osaka, I.; McCullough, R. D. Advances in molecular design and synthesis of regioregular polythiophenes. *Acc. Chem. Res.* **2008**, *41*, 1202-1214.

(145) Kline, R. J.; DeLongchamp, D. M.; Fischer, D. A.; Lin, E. K.; Richter, L. J.; Chabinyc, M. L.; Toney, M. F.; Heeney, M.; McCulloch, I. Critical role of side-chain attachment density on the order and device performance of polythiophenes. *Macromolecules* **2007**, *40*, 7960-7965.

(146) Park, Y. D.; Kim, D. H.; Jang, Y.; Cho, J. H.; Hwang, M.; Lee, H. S.; Lim, J. A.; Cho, K. Effect of side chain length on molecular ordering and field-effect mobility in poly(3-alkylthiophene) transistors. *Org. Electron.* **2006**, *7*, 514-520.

(147) Oosterbaan, W. D.; Bolsee, J. C.; Gadisa, A.; Vrindts, V.; Bertho, S.; D'Haen, J.; Cleij, T. J.; Lutsen, L.; McNeill, C. R.; Thomsen, L.; Manca, J. V.; Vanderzande, D. Alkyl-Chain-Length-Independent Hole Mobility via Morphological Control with Poly(3-alkylthiophene) Nanofibers. *Adv. Funct. Mater.* **2010**, *20*, 792-802.

(148) Jiang, X. M.; Osterbacka, R.; Korovyanko, O.; An, C. P.; Horovitz, B.; Janssen, R. A. J.; Vardeny, Z. V. Spectroscopic studies of photoexcitations in regioregular and regiorandom polythiophene films. *Adv. Funct. Mater.* **2002**, *12*, 587-597.

(149) Mauer, R.; Kastler, M.; Laquai, F. The Impact of Polymer Regioregularity on Charge Transport and Efficiency of P3HT:PCBM Photovoltaic Devices. *Adv. Funct. Mater.* **2010**, *20*, 2085-2092.

(150) Tajima, K.; Suzuki, Y.; Hashimoto, K. Polymer photovoltaic devices using fully regioregular poly[(2-methoxy-5-(3 ',7 '-dimethyloctyloxy))-1,4-phenylenevinylene]. *J. Phys. Chem. C* **2008**, *112*, 8507-8510.

(151) Suzuki, Y.; Hashimoto, K.; Tajima, K. Synthesis of regioregular poly(p-phenylenevinylene)s by Horner reaction and their regioregularity characterization. *Macromolecules* **2007**, *40*, 6521-6528.

(152) Brown, P. J.; Thomas, D. S.; Kohler, A.; Wilson, J. S.; Kim, J. S.; Ramsdale, C. M.; Sirringhaus, H.; Friend, R. H. Effect of interchain interactions on the absorption and emission of poly(3-hexylthiophene). *Phys. Rev. B* **2003**, *67*.

(153) Sugimoto, T.; Habuchi, S.; Ogino, K.; Vacha, M. Conformation-Related Exciton Localization and Charge-Pair Formation in Polythiophenes: Ensemble and Single-Molecule Study. *J. Phys. Chem. B* **2009**, *113*, 12220-12226.

(154) Terada, Y.; Choi, B. K.; Heike, S.; Fujimori, M.; Hashizume, T. Placing conducting polymers onto a H-terminated Si(100) surface via a pulse valve. *Nano Lett.* **2003**, *3*, 527-531.

(155) Scifo, L.; Dubois, M.; Brun, M.; Rannou, P.; Latil, S.; Rubio, A.; Grevin, B. Probing the electronic properties of self-organized poly(3-dodecylthiophene) monolayers by two-dimensional scanning tunneling spectroscopy imaging at the single chain scale. *Nano Lett.* **2006**, *6*, 1711-1718.

(156) Mena-Osteritz, E.; Meyer, A.; Langeveld-Voss, B. M. W.; Janssen, R. A. J.; Meijer, E. W.; Bauerle, P. Two-dimensional crystals of poly(3-alkylthiophene)s: Direct visualization of polymer folds in submolecular resolution. *Angewandte Chemie-International Edition* **2000**, *39*, 2680-2684.

(157) Darling, S. B.; Sternberg, M. Importance of Side Chains and Backbone Length in Defect Modeling of Poly(3-alkylthiophenes). *J. Phys. Chem. B* **2009**, *113*, 6215-6218.

(158) Loewe, R. S.; Ewbank, P. C.; Liu, J. S.; Zhai, L.; McCullough, R. D. Regioregular, head-to-tail coupled poly(3-alkylthiophenes) made easy by the GRIM method: Investigation of the reaction and the origin of regioselectivity. *Macromolecules* **2001**, *34*, 4324-4333.

(159) Urien, M.; Bailly, L.; Vignau, L.; Cloutet, E.; de Cuendias, A.; Wantz, G.; Cramail, H.; Hirsch, L.; Parneix, J. P. Effect of the regioregularity of poly(3-hexylthiophene) on the performance of organic photovoltic devices. *Polym. Int.* **2008**, *57*, 764-769.

(160) Plimpton, S. Fast Parallel Algorithms for Short-Range Molecular-Dynamics. *J. Comput. Phys.* **1995**, *117*, 1-19.

(161) Moreno, M.; Casalegno, M.; Raos, G.; Meille, S. V.; Po, R. Molecular Modeling of Crystalline Alkylthiophene Oligomers and Polymers. *J. Phys. Chem. B* **2010**, *114*, 1591-1602.

(162) Schneider, T.; Stoll, E. Molecular-Dynamics Study of a 3-Dimensional One-Component Model for Distortive Phase-Transitions. *Phys. Rev. B* **1978**, *17*, 1302-1322.

(163) Sugita, Y.; Okamoto, Y. Replica-exchange molecular dynamics method for protein folding. *Chem. Phys. Lett.* **1999**, *314*, 141-151.

(164) Bai, X.; Holdcroft, S. Molecular Control of Luminescence from Poly(3-Hexylthiophenes). *Macromolecules* **1993**, *26*, 4457-4460.

(165) Chen, T. A.; Wu, X. M.; Rieke, R. D. Regiocontrolled Synthesis of Poly(3-Alkylthiophenes) Mediated by Rieke Zinc - Their Characterization and Solid-State Properties. *J. Am. Chem. Soc.* **1995**, *117*, 233-244.

(166) Mao, H. Y.; Xu, B.; Holdcroft, S. Synthesis and Structure Property Relationships of Regioirregular Poly(3-Hexylthiophenes). *Macromolecules* **1993**, *26*, 1163-1169.

(167) Lee, C. K.; Hua, C. C.; Chen, S. A. Single-Chain and Aggregation Properties of Semiconducting Polymer Solutions Investigated by Coarse-Grained Langevin Dynamics Simulation. *J. Phys. Chem. B* **2008**, *112*, 11479-11489.

(168) Yang, X.; Loos, J. Toward high-performance polymer solar cells: The importance of morphology control. *Macromolecules* **2007**, *40*, 1353-1362.

(169) Westenhoff, S.; Howard, I. A.; Friend, R. H. Probing the morphology and energy landscape of blends of conjugated polymers with sub-10 nm resolution. *Phys. Rev. Lett.* **2008**, *101*, 016102.

(170) Hoffmann, S. T.; Scheler, E.; Koenen, J.-M.; Forster, M.; Scherf, U.; Strohriegl, P.; Baessler, H.; Koehler, A. Triplet energy transfer in conjugated polymers. III. An experimental assessment regarding the influence of disorder on polaronic transport. *Phys. Rev. B* **2010**, *81*, 165208.

(171) Kobayashi, H.; Onda, S.; Furumaki, S.; Habuchi, S.; Vacha, M. A single-molecule approach to conformation and photophysics of conjugated polymers. *Chem. Phys. Lett.* **2012**, *528*, 1-6.

(172) Habuchi, S.; Onda, S.; Vacha, M. Molecular weight dependence of emission intensity and emitting sites distribution within single conjugated polymer molecules. *Phys. Chem. Chem. Phys.* **2011**, *13*, 1743-1753.

(173) Brinkmann, M. Structure and morphology control in thin films of regioregular poly(3-hexylthiophene). *J. Polym. Sci., Part B: Polym. Phys.* **2011**, *49*, 1218-1233.

(174) Adachi, T.; Brazard, J.; Ono, R.; Bielawski, C.; Vanden Bout, D. Regioregularity effect on conformation and opto-electronic properties in single polythiophene chains. *Proc. SPIE* **2011**, *8098*, 80980F.

(175) Adachi, T.; Brazard, J.; Ono, R. J.; Hanson, B.; Traub, M. C.; Wu, Z. Q.; Li, Z. C.; Bolinger, J. C.; Ganesan, V.; Bielawski, C. W.; Bout, D. A. V.; Barbara, P. F. Regioregularity and Single Polythiophene Chain Conformation. *J. Phys. Chem. Lett* **2011**, *2*, 1400-1404.

(176) Traub, M. C.; Lakhwani, G.; Bolinger, J. C.; Vanden Bout, D.; Barbara, P. F. Electronic Energy Transfer in Highly Aligned MEH-PPV Single Chains. *J. Phys. Chem. B* **2011**, *115*, 9941-9947.

(177) Becker, K.; Lupton, J. M. Efficient light harvesting in dye-endcapped conjugated polymers probed by single molecule spectroscopy. *J. Am. Chem. Soc.* **2006**, *128*, 6468-6479.

(178) Becker, K.; Lupton, J. M.; Feldmann, J.; Setayesh, S.; Grimsdale, A. C.; Mullen, K. Efficient intramolecular energy transfer in single endcapped conjugated polymer molecules in the absence of appreciable spectral overlap. *J. Am. Chem. Soc.* **2006**, *128*, 680-681.

(179) Lin, H.; Tabaei, S. R.; Thomsson, D.; Mirzov, O.; Larsson, P.-O.; Scheblykin, I. G. Fluorescence blinking, exciton dynamics, and energy transfer domains in single conjugated polymer chains. *J. Am. Chem. Soc.* **2008**, *130*, 7042-7051.

(180) Beljonne, D.; Pourtois, G.; Silva, C.; Hennebicq, E.; Herz, L. M.; Friend, R. H.; Scholes, G. D.; Setayesh, S.; Müllen, K.; Brédas, J. L. Interchain vs. intrachain energy transfer in acceptor-capped conjugated polymers. *Proceedings of the National Academy of Sciences* **2002**, *99*, 10982-10987.

(181) Scholes, G. D. Long-range resonance energy transfer in molecular systems. *Annu. Rev. Phys. Chem.* **2003**, *54*, 57-87.

(182) Westenhoff, S.; Daniel, C.; Friend, R. H.; Silva, C.; Sundstrom, V.; Yartsev, A. Exciton migration in a polythiophene: Probing the spatial and energy domain by line-dipole Forster-type energy transfer. *J. Chem. Phys.* **2005**, *122*, 094903.

(183) Theander, M.; Inganas, O.; Mammo, W.; Olinga, T.; Svensson, M.; Andersson, M. R. Photophysics of substituted polythiophenes. *J. Phys. Chem. B* **1999**, *103*, 7771-7780.

(184) Palacios, R. E.; Barbara, P. F. Single molecule spectroscopy of poly 3-octyl-thiophene (P3OT). *J. Fluoresc.* **2007**, *17*, 749-757.

(185) Feist, F. A.; Basche, T. Fluorescence excitation and emission spectroscopy on single MEH-PPV chains at low temperature. *J. Phys. Chem. B* **2008**, *112*, 9700-9708.

(186) Forster, M.; Thomsson, D.; Hania, P. R.; Scheblykin, I. G. Redistribution of emitting state population in conjugated polymers probed by single-molecule fluorescence polarization spectroscopy. *Phys. Chem. Chem. Phys.* **2007**, *9*, 761-766.

(187) Cornil, J.; dos Santos, D. A.; Crispin, X.; Silbey, R.; Bredas, J. L. Influence of interchain interactions on the absorption and luminescence of conjugated oligomers and polymers: A quantum-chemical characterization. *J. Am. Chem. Soc.* **1998**, *120*, 1289-1299.

(188) Sterpone, F.; Bedard-Hearn, M. J.; Rossky, P. J. Nonadiabatic Mixed Quantum-Classical Dynamic Simulation of pi-Stacked Oligophenylenevinylenes. *J. Phys. Chem. A* **2009**, *113*, 3427-3430.

(189) Kose, M. E. Evaluation of Excitonic Coupling and Charge Transport Integrals in P3HT Nanocrystal. *J. Phys. Chem. C* **2011**, *115*, 13076-13082.

(190) Vogelsang, J.; Adachi, T.; Brazard, J.; Bout, D. A. V.; Barbara, P. F. Self-assembly of highly ordered conjugated polymer aggregates with long-range energy transfer. *Nature Mater.* **2011**, *10*, 942-946.

(191) Jaczewska, J.; Budkowski, A.; Bernasik, A.; Moons, E.; Rysz, J. Polymer vs solvent diagram of film structures formed in spin-cast poly(3-alkylthiophene) blends. *Macromolecules* **2008**, *41*, 4802-4810.

(192) Jaczewska, J.; Raptis, I.; Budkowski, A.; Goustouridis, D.; Raczkowska, J.; Sanopoulou, A.; Pamula, E.; Bernasik, A.; Rysz, J. Swelling of poly(3-alkylthiophene) films exposed to solvent vapors and humidity: Evaluation of solubility parameters. *Synth. Met.* **2007**, *157*, 726-732.

(193) Hennebicq, E.; Pourtois, G.; Scholes, G. D.; Herz, L. M.; Russell, D. M.; Silva, C.; Setayesh, S.; Grimsdale, A. C.; Müllen, K.; Brédas, J.-L.; Beljonne, D. Exciton Migration in Rigid-Rod Conjugated Polymers:An Improved Forster Model. *J. Am. Chem. Soc.* **2005**, *127*, 4744-4762.

(194) E.B.Preistley; Wojtowicz, P. J.; Sheng, P. *Introductions to Liquid crystals*; Plenum Press, New York and London, 1974.

(195) Chandrasekhar, S. *Liquid Crystals*, second ed.; Cambridge university press: Cambridge, UK, 1992.

(196) Donald, A.; Windle, A.; Hanna, S. *Liquid Crystalline Polymers*; Canbridge university press: Cambridge, UK, 2006.

(197) Gaiduk, A.; Yorulmaz, M.; Ruijgrok, P. V.; Orrit, M. Room-Temperature Detection of a Single Molecule's Absorption by Photothermal Contrast. *Science* **2010**, *330*, 353-356.

(198) Chong, S.; Min, W.; Xie, X. S. Ground-State Depletion Microscopy: Detection Sensitivity of Single-Molecule Optical Absorption at Room Temperature. *J. Phys. Chem. Lett* **2010**, *1*, 3316-3322.

(199) Kukura, P.; Celebrano, M.; Renn, A.; Sandoghdar, V. Single-Molecule Sensitivity in Optical Absorption at Room Temperature. *J. Phys. Chem. Lett* **2010**, *1*, 3323-3327.

(200) Feist, F. A.; Tommaseo, G.; Basché, T. Observation of Very Narrow Linewidths in the Fluorescence Excitation Spectra of Single Conjugated Polymer Chains at 1.2 K. *Phys. Rev. Lett.* **2007**, *98*, 208301.

(201) Feist, F. A.; Basché, T. Fluorescence Excitation and Emission Spectroscopy on Single MEH-PPV Chains at Low Temperature. *J. Phys. Chem. B* **2008**, *112*, 9700-9708.

(202) Walter, M. J.; Borys, N. J.; van Schooten, K. J.; Lupton, J. M. Light-Harvesting Action Spectroscopy of Single Conjugated Polymer Nanowires. *Nano Lett.* **2008**, *8*, 3330-3335.

(203) Soegiarto, A. C.; Comotti, A.; Ward, M. D. Controlled Orientation of Polyconjugated Guest Molecules in Tunable Host Cavities. *J. Am. Chem. Soc.* **2010**, *132*, 14603-14616.

(204) Soegiarto, A. C.; Ward, M. D. Directed Organization of Dye Aggregates in Hydrogen-Bonded Host Frameworks. *Cryst. Growth Des.* **2009**, *9*, 3803-3815.